A search for long-lived particles with large ionization energy loss in the ATLAS silicon pixel detector using 139 fb^{-1} of $\sqrt{s} = 13$ TeV pp collisions

A DISSERTATION PRESENTED
BY
ANN MIAO WANG
TO
THE DEPARTMENT OF PHYSICS

IN PARTIAL FULFILLMENT OF THE REQUIREMENTS
FOR THE DEGREE OF
DOCTOR OF PHILOSOPHY
IN THE SUBJECT OF
PHYSICS

HARVARD UNIVERSITY
CAMBRIDGE, MASSACHUSETTS

MAY 2021

Thesis advisor: Professor Melissa Franklin Ann Miao Wang

A search for long-lived particles with large ionization energy loss in the ATLAS silicon pixel detector using 139 fb^{-1} of $\sqrt{s} = 13$ TeV pp collisions

Abstract

The results from a search for long-lived, heavy charged particles with the ATLAS Run-2 dataset are presented. As charged particles move through a material, the amount of energy they lose via ionization depends only on their mass for a given momentum. This property can be used to search for new Beyond the Standard Model particles in $\sqrt{s}$ = 13 TeV proton-proton collisions at the Large Hadron Collider. This search is conducted using data collected by the ATLAS detector, with an integrated luminosity of 139 fb^{-1}. Events are required to have large missing transverse energy and an isolated, high-quality track with large transverse momentum and large ionization energy loss. The analysis tests the data for evidence of supersymmetric particles including gluinos, charginos, and sleptons. The observed yields in the signal regions are consistent with Standard Model expectation for low reconstructed track mass. At high mass, there is an excess of observed events over data, with the largest deviation in a mass region spanning 1100 to 2800 GeV, where 7 events are observed and 0.7 ± 0.4 events are predicted.

Contents

Listing of figures

Listing of tables

Acknowledgments

In my twenty-eight years, the last six years have proven to be both the most challenging and the most rewarding. A few of the happiest moments included seeing first data in 38 Oxford, talking about physics with my colleages, and watching the cows outside of BB5. Physics is the most fun when shared with other people, and that is the beauty of working in a collaboration. Over the years I've been incredibly fortunate to have met so many incredible people.

To my advisor Melissa– in order to thank you for all of the things that I should, I might need several pages. But I'd like to thank you in particular for pushing me to do things I didn't particularly want to do, because you were usually right in the end. Thank you for the many hours of guidance over the phone (even though I know you'd rather be in the lab with me). Thank you for insisting that I always check the overflow entries, and for the physics table. Most of all thank you for accepting me as your student.

To Paolo– working on the Harvard cosmic ray test stand with you was the most fun I've ever had doing physics. Thank you for showing me an ocean of patience and how to build something from start to finish with equanimity, diligence, and lots of humor. It was truly a pleasure to work with you every day, and I can't describe how grateful I am for that time. I'd also like to thank you for the attempts at my cultural education, although I still haven't seen a single Fellini film.

Alex– I spent the most time with you over the course of my PhD, so first and foremost thank you

for putting up with me through all of that. Moving to a foreign country can be challenging, and I'm particularly grateful for your support in the first few months after moving to Geneva. Thank you asking me the right questions, insisting that my plots were perfect, and for the secret hoard of hot sauce. Next time I'll let you order the cables the way you want to.

Simone– thank you for the wonderful semester at LBL and sharing your time to teach me how to do a physics analysis. Your broad expertise across physics and consideration for details is something I aspire to learn. Without your help, I'm not sure this thesis would have been possible.

Thank you to Werner for showing me that detectors are not magical boxes but (somewhat) predictable devices. Thank you for inspiring me to understand signal generation and for the tourist tips in Vienna. Thank you to Heinrich as well for the simulation advice and the generous help.

Karri, you always pushed my boundaries and preconceptions. We were roommates and labmates but somewhere along the way we became lifelong friends. Thanks for paving the way as the older student, the many adventures with tiny Peanut, and the many life discussions.

Thank you to my committee members, Roxanne and Andy. Roxanne, thank you for the career advice and for the many helpful thesis comments. Thanks to Andy for the boundless curiosity and taking the time to give me advice as a phyisicist outside my field.

Thanks to the entire pixel dE/dx analysis team, whose work contributed immensely to this thesis. Hide, thank you for guiding me through my first project on the main analysis and for always answering my questions, however late it is in Tokyo. Ismet, thank you for helping me when I needed it the most. Laura, your advice and analysis guidance were invaluable to a young physicist. Leo, thank you for your detailed questions and for pushing the analysis forward. Kate, thank you for always lending

a helping hand. Thank you to Simone, Stefano, Andrea, Dario, Claudia, Alex, Eunchong, Ashutosh, Zack, Jerry, Anne, and Nina for the perpetually interesting physics discussions.

The Harvard ATLAS group is full of both amazing physicists and people. Thank you to Masahiro, John, and Melissa for sharing your physics knowledge and for making the group environment so fun. Chris– thank you for believing in me as a young graduate student and showing me that understanding the physics was just as important as producing plots. Larry, although we never spent much time working directly together, you were always there whenever I needed help, whether it was had to do with understanding a phenomenological paper or finding good food in Geneva. Thank you for the delicious dinners and for always telling me about the latest exciting paper or proposed experiment in physics. Thank you to Nathan Felt and Steve Sansone for your jokes and endless technical expertise. Sarah, your magical ability to solder tiny resistors amazes me – thank you. Stefano, Alexandra, Rongkun, and Aaron, thank you for being wonderful postdoc mentors.

Thank you to the entire LBL group for giving me a home for the semester at Berkeley. Thank you to Maurice and Timon for the help on ITk, and thank you to Elodie for the vending machine chats and friendship.

Thank you to Christos B., Christos P., Kostas, Dimitrios, Patrick, and Andreas for the fun times in BB5 and test beam. Christos B., thanks for showing me around Greece. Thanks to Junjie, Bing, Verena, and Mauro for keeping us on the right path.

Thanks to my fellow high energy physics graduate students with whom I've shared a lot of wonderful experiences, both older and younger: Gareth, Tomo, Emma, Sun, Tony, Stephen, Jennifer, Julia, Karri, Brendon, Nicolo, Gabriel, Anne, Anthony, Alexis, and Jerry. Special thanks to Anne for

finally convincing me to see other parts of Switzerland, and to Anthony for helping me through the hardest parts of applying to jobs. Jerry also pointed out that I should thank `GNU Emacs`, so thank you `GNU Emacs`.

Thanks to all of the wonderful Harvard undergraduate and high school students I was lucky enough to work with, including Julia, Ben, Jonah, Joseph, Sarah, Zack, Youssef, Khalil, Josh, Toby, and Nina. Special thanks to Josh for the color scheme, and to Nina, Anne, Alexis, and Jerry for comments on my thesis.

Physics 123 is by far the best course I've ever taken. Thank you Tom for your dedication to the course material which inspired my appreciation for electronics.

Lisa and Carol, thanks for providing an ear when things got hard. Your presence and open doors means so much to the graduate students.

When I started at Caltech, I was determined to become a medical doctor. Thanks first to the core curriculum at Caltech, which forced an aspiring doctor to take five terms of physics. Steven Frautschi's approachable and clear teaching of electromagnetism drew me away from my intended path. Gil Refael's introduction to quantum mechanics cemented the point of no return. Thank you to Paul Sternberg and Amir Sapir for letting me spend a year in a worm lab, where I learned that research was pretty fun. Finally, thank you to Maria, Harvey, Javier, Cristian, and Dustin for opening my eyes to particle physics.

Thanks to Mrs. Munch, my high school math teacher, for being so supportive of my interest in math and teaching me how to take a derivative.

My friends in both Cambridge and Geneva pulled me away from the lab. Caroline– our dreams

of a commune will never die. To the residents of 29 Magnus– Rebecca, Maya, and Annie– I couldn't have imagined a better group of roommates. Thank you for the Friday night circles and wine. I was also blessed with a wonderful physics cohort– thank you for all of the laughs and physics discussion. To my friends in Geneva: thanks for showing me how amazing it can be to live in Switzerland. Tova, Emma, Larry, Karri, Kate, Lesya, Max, and Doose, I wouldn't have survived without your support and friendship. Thanks to my friends from Caltech who provide such a strong support network and plan the best vacations. Thank you to Nico for being there at the end.

Finally, thank you to my family, who motivate me each and every day.

List of Acronyms

SM Standard Model

QCD Quantum Chromodynamics

EWSB Electroweak Symmetry Breaking

BSM Beyond the Standard Model

SUSY Supersymmetry

MSSM Minimal Supersymmetric Extension of the Standard Model

GMSB Gauge-Mediated Supersymmetry Breaking

AMSB Anomaly-Mediated Supersymmetry Breaking

LSP Lightest Supersymmetric Particle

NLSP Next-To-Lightest Supersymmetric Particle

LHC Large Hadron Collider

ATLAS A Toroidal LHC Apparatus

CMS Compact Muon Solenoid

PSB Proton Synchrotron Booster

PS Proton Synchrotron

SPS Super Proton Synchrotron

MIP Minimum Ionizing Particle

MPV Most Probable Value

ID Inner Detector

MS Muon Spectrometer

IP Interaction Point

SCT Semiconductor Tracker

TRT Transition Radiation Tracker

IBL Insertable B-Layer

ToT Time Over Threshold

LL Low Level

HL High Level

MDT Monitored Drift Tube

CSC Cathode Strip Chamber

RPC Resistive Plate Chamber

TGC Thin Gap Chamber

MWPC Multiwire Proportional Chamber

LAr Liquid Argon

TileCal Tile Calorimeter

EM Electromagnetic

PMT Photomultiplier Tube

CB Combined

ME Extrapolated

L1 Level-1

HLT High Level Trigger

JVT Jet-Vertex-Tagger

IBL OF Insertable B-Layer Overflow

ISR Initial State Radiation

AOD Analysis Object Data

1

Introduction

The field of particle physics has been marked by countless theoretical and experimental achievements. Its progress has included not only a deeper theoretical understanding over the years but also the development of technologies that help us probe the smallest length scales and the highest energies. There could not exist one without the other. The simple cathode ray tube showed the world that atoms were peppered with tiny electrons in J.J. Thomson's famous experiment [?], paving the

way for a theoretical understanding of the atom. Many years later, Murray Gell-Mann and Yuval Ne'eman's Eightfold Way [1, 2] predicted the omega baryon, which was then discovered in 1964 at Brookhaven National Laboratory [3].

Arguably the most fundamental, experimentally verified theory of this world is the Standard Model (SM) of physics. Its predictive power guided many experimental physicists, who in turn saw unexpected signatures in their data that motivated theorists to pen more equations. The final particle predicted by the SM was theorized by Higgs [4, 5], Englert and Brout [6], and Guralnik, Hagen, and Kibble [7] in 1964. It was discovered by experimentalists almost 50 years later with the A Toroidal LHC Apparatus (ATLAS) and Compact Muon Solenoid (CMS) detectors at the Large Hadron Collider (LHC) [8, 9].

After the experimental discovery of the last SM particle, a sea of theories predicting physics beyond the SM have been proposed to solve the shortcomings of the SM. This thesis work explores some of those theories to look for signs of new physics. In particular, the work is guided by but not restricted to theoretical predictions, in hopes that there is something unpredicted in the data. The thesis describes a search for new physics using a technique which is sensitive to Beyond the Standard Model (BSM) theories but dependent only on the generic properties of charged particle interactions.

Chapter 2 describes the SM as well as BSM theories that this thesis work could potentially verify. The theory of energy loss by a charged particle in material, which forms the fundamental basis of this search, is described in Chapter 3.

Chapter 4 describes the machines built to collect the dataset used in this thesis work: the LHC and the ATLAS detector. Chapter 5 describes how ATLAS triggers on interesting collisions and

reconstructs the collected data into useful physics objects. Chapter 6 explains how the energy loss measurement is conducted, corrected, and calibrated. Chapters 7–9 present the details of the search strategy, estimation of Standard Model background, and systematic uncertainties.

Finally, Chapter 10 presents the results of the search in data. Chapter 11 concludes this work.

Much of this thesis is adapted from the ATLAS internal note on this topic, `ANA-SUSY-2018-42-INT1`, of which the thesis author is a contributor [10]. Figures and tables adapted from the internal note will be marked with a dagger symbol (†) in the caption. The analysis is also described in an ATLAS paper [11].

2

The Standard Model and Beyond

Physicists have been both blessed and cursed with the theory of the SM. The theory has led us to discoveries and given us a description of the universe, but its shortcomings are numerous and can be likened to breadcrumbs leading physicists out of the dark woods.

To provide context for this analogy, the SM is described qualitatively in the following chapter with a particle-based perspective. Several questions that the SM does not answer will be pointed out

and discussed. A few potential solutions, provided by BSM theories, will be described in Section 2.2 with a focus on supersymmetric theories.

2.1 The Standard Model

The Standard Model can be viewed as a portrait of the fundamental particles of the universe and their interactions (see Figure 2.1).

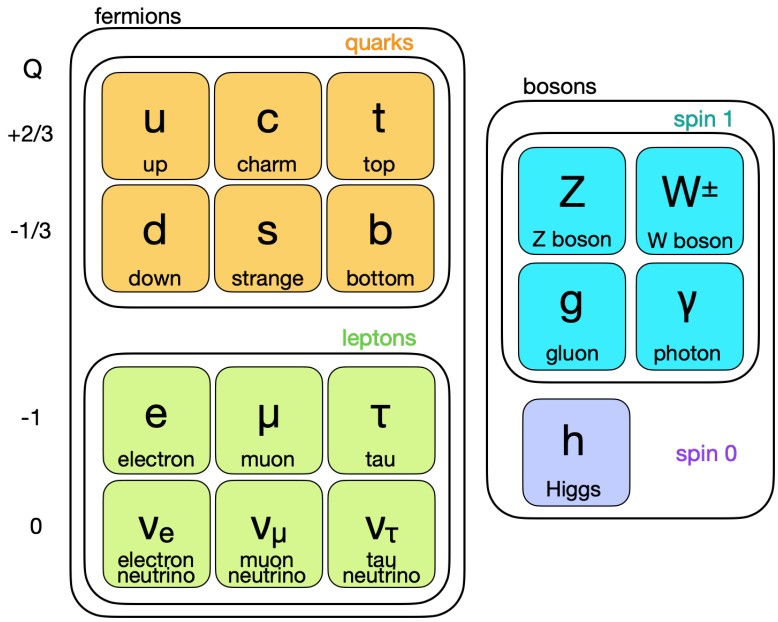

Figure 2.1: The Standard Model particles. There are three generations of leptons and quarks which make up the fermions. The force carriers, or bosons, include the spin-1 gauge bosons as well as the scalar Higgs boson.

The set of particles described by the Standard Model include three generations of matter, or fermions. There are six quarks and six leptons, as well as their antiparticles, each with quantum spin $1/2$. Three of the quarks have $+2/3$ electric charge and three have $-1/3$. The leptons with electric

charge -1 include the familiar electron which makes up ordinary matter and its heavier unstable cousins the muon and the tau. There are also three neutrinos, which are neutral massless particles. *

These particles interact by exchanging bosons, or particles of integer spin which serve as the force carriers. The spin 1 bosons include the photon, the W and Z bosons, and the gluon. The photon is the carrier of the electromagnetic force, and the W and Z are carriers of the weak force. The gluon is the carrier of the strong force. Particles must be *charged* under the force to interact with the associated bosons; the quarks are charged under color and interact via the strong force, but the leptons do not carry color charge. All fermions carry weak and electromagnetic charge, with the exception of the neutrinos which are neutral.

The Higgs boson is the only scalar fundamental particle. Through the mechanism of Electroweak Symmetry Breaking (EWSB), the inclusion of the Higgs field in the SM gives the other particles mass.

The SM can be encapsulated in a Lagrangian with 19 parameters which are experimentally determined. The parameters include the fermion masses and Higgs mass, as well as the Higgs vaccum expectation value, the quark mixing angles, a CP violating phase, the Quantum Chromodynamics (QCD) theta term, and the coupling constants [14, 15].

*Neutrinos are massless in the Standard Model, but experiments in the past few decades have shown that they have non-zero mass. [12, 13]

2.2 Beyond the Standard Model

While measurements continue to test different aspects of the SM with greater and greater precision [16], several discoveries of the past century revealed paradigm-shifting physics not described by the theory. In the 1930s, Oort and Zwicky saw hints that galaxies contained more mass than was visible or luminous by measuring stellar velocities in the Milky Way and the velocity dispersion of galaxies in the Coma Cluster [17–19]. Rubin measured galactic rotation curves in the 1970s and found that the velocity of stars orbiting the galactic center did not decrease with increasing radius from the center, which implied that the galactic mass was not concentrated in the visible region [20]. In 1979, Walsh and collaborators provided supporting evidence that there was some form of non-visible mass by measuring gravitational lensing effects [21]. Further details, as well as other evidence for the existence of some sort of non-visible matter, called dark matter, are summarized in [22]. The SM provides no particle which could explain the observed dark matter.

Another weakness of the SM is the "hierarchy problem". The hierarchy problem arises from the fact that the Higgs mass corrections include extremely large terms from any particles that the Higgs interacts with (either at tree-level or through loops). Each particle adds a one-loop correction term Δm_h^2 proportional to Λ^2, where Λ is a cutoff scale at which the theory is no longer valid. This is generally taken to be M_P, or the Planck mass, which can be considered the next scale at which new physics modifies the SM. These quantum corrections are about 30 orders of magnitude larger than the Higgs mass of 125 GeV, necessitating fine-tuning [23].

There are countless theories which offer solutions to the various weaknesses of the SM, but this

thesis will focus on Supersymmetry (SUSY). SUSY can be motivated by considering the corrections to the Higgs mass, Δm_h^2, which include contributions from the interaction of the Higgs with fermions and bosons. A key observation is that terms from fermions and bosons contribute with opposite sign in the loop. Therefore if there were corresponding partner particles for every SM particle, except with differing spin, the problematically large corrections to the Higgs mass would be canceled.

The general principle of SUSY introduces superpartner particles to the SM particles, which solves the hierarchy problem for exactly this reason. In the Minimal Supersymmetric Extension of the Standard Model (MSSM), each SM particle is embedded into a mathematical object called a *supermultiplet* along with its superpartners.

If we require a renormalizable theory there are two relevant supermultiplet objects: *chiral* and *gauge* supermultiplets [23]. The chiral supermultiplets each consist of a two-component Weyl fermion with spin $1/2$ (one for each helicity state) and a complex scalar field. The gauge supermultiplets each consist of a two-component Weyl fermion with spin $1/2$ and a spin 1 vector field, where the two fermionic components have the same gauge transformations. The SM fermions can be embedded into the chiral supermultiplets, resulting in scalar superpartners, and the SM bosons can be embedded into gauge supermultiplets, resulting in spin $1/2$ superpartners. The SM Higgs fields are embedded in chiral supermultiplets, of which two are required to avoid gauge anomalies [23]. An important consequence of this is the prediction of multiple Higgs bosons in SUSY theories.

In summary, each fermion has a bosonic superpartner with spin 0, and each spin 1 boson has a fermionic superpartner with spin $1/2$. The scalar bosonic superpartners are called squarks and

sleptons, while the fermionic superpartners include winos (superpartner of the bosons W^+, W^-, Z^0), bino (superpartner of the B), and the gluino (superpartner of the gluon). The superpartners of the Higgses are the higgsinos, and the superpartner of the graviton (mediator of the gravitational force) is the gravitino. After EWSB, the higgsinos and gaugino (wino and bino) fields mix to form four neutral states and two charged states, called neutralinos and charginos [23]. The sparticles are summarized in Figure 2.2.

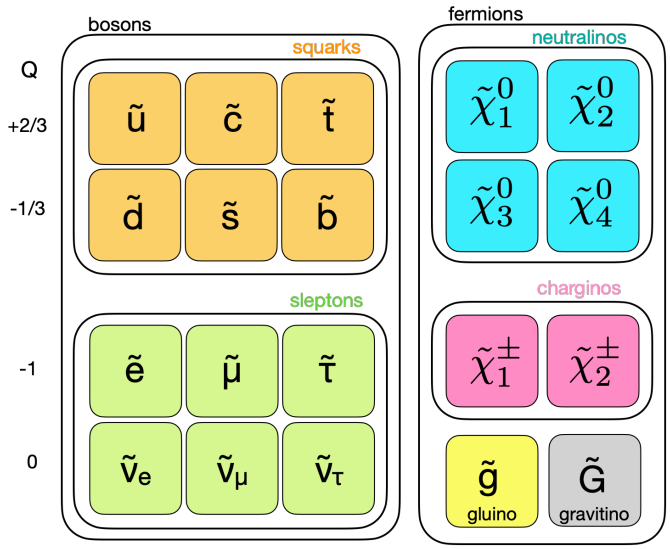

Figure 2.2: The Minimal Supersymmetric Extension of the Standard Model particles. There are scalar superpartners for the SM fermions, and fermionic superpartners for the SM bosons. After EWSB, the higgsinos and gauginos mix to form the neutralinos and charginos.

Naively this natural extension of the SM built out of these supermultiplets would set the superpartner masses at the original SM masses. However, no supersymmetric particles have been found to-date, so this leads us to require a mechanism which breaks the supersymmetry. This is usually done by adding a soft supersymmetry breaking term $\mathcal{L}_{\text{soft}}$, such that the full theory is expressed as

$\mathcal{L} = \mathcal{L}_{\text{SUSY}} + \mathcal{L}_{\text{soft}}$ [23].

$\mathcal{L}_{\text{soft}}$ allows for the supersymmetric partners, or *sparticles*, to have larger masses than the SM particles. The origin of the terms in $\mathcal{L}_{\text{soft}}$ is discussed in 2.2.1.

Another problem with the simplest supersymmetric theory is that it allows the proton to decay quickly through a intermediate sparticle, in contrast with current experimental bounds on the proton lifetime [24]. To solve this, a new symmetry called *R-parity* is explicity added so that all particles have even R-parity and all sparticles have odd R-parity. Note that this results in a Lightest Supersymmetric Particle (LSP) which is stable due to this symmetry, providing an excellent dark matter particle candidate.

The full set of vertices allowed in the MSSM assuming R-parity conservation can be found in [25].

2.2.1 Supersymmetry breaking mechanisms

Adding a general $\mathcal{L}_{\text{soft}}$ to the MSSM which preserves gauge invariance and R-parity introduces 105 seemingly arbitrary new parameters to the theory [23, 26]. A key aspect of constructing a SUSY theory is explaining the origin of the terms in $\mathcal{L}_{\text{soft}}$ and the associated free parameters.

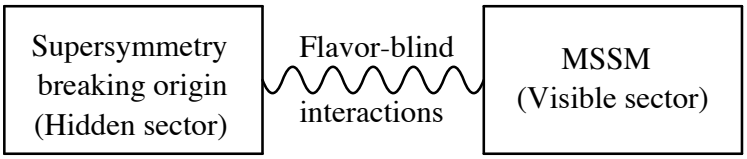

Figure 2.3: Hypothesized framework of SUSY breaking. The breaking happens in a hidden sector of particles which couple indirectly to the visible sector [23].

There are numerous mechanisms proposed to generate the supersymmetry-breaking terms. Discussion of these mechanisms can be found in [23]. Two mechanisms in particular can easily result in long-lived particle signatures at the LHC, which will be the target of this thesis. One of these is Gauge-Mediated Supersymmetry Breaking (GMSB) [27]. GMSB predicts a set of messenger particles which couple to the SUSY breaking sector as well as the SM particles and their partners. In this scenario, the LSP is predicted to be the gravitino. Any other supersymmetric particle $\tilde{X}$ will eventually decay to the gravitino, and the decay rate can be calculated as [23]:

$$\Gamma(\tilde{X} \to X\tilde{G}) = \frac{m_{\tilde{X}}^5}{48\pi {M_P}^2 m_{3/2}^2} \left(1 - m_X^2/m_{\tilde{X}}^2\right)^4 \tag{2.1}$$

where $m_{3/2}$ is the gravitino mass. In these scenarios, the Next-To-Lightest Supersymmetric Particle (NLSP) is predicted to be either a bino or a slepton, the latter of which could leave a track in the particle detector. If $m_{3/2} \gtrsim 1$ keV, then the slepton is likely to be stable on the order of length scale of the ATLAS detector [23].

Another proposed mechanism is Anomaly-Mediated Supersymmetry Breaking (AMSB), where the SUSY breaking results from a superconformal anomaly [28, 29]. The gaugino masses in this scenario can be calculated to be [23]:

$$\begin{aligned} M_1 &= \frac{33}{5}\frac{m_{3/2}}{16\pi^2} g_1^2 \\ M_2 &= \frac{m_{3/2}}{16\pi^2} g_2^2 \\ M_3 &= -\frac{m_{3/2}}{16\pi^2} 3 g_3^2, \end{aligned} \tag{2.2}$$

where $g_1 = \sqrt{5/3}e/\cos\theta_W$, $g_2 = e/\sin\theta_W$, and $g_3 = \sqrt{4\pi\alpha_S}$ are the SM gauge couplings. M_1, M_2, and M_3 are the masses of the bino, wino, and gluino, respectively. This results in the neutralino with a large wino-content as the LSP and a chargino about 200 MeV heavier in mass. Due to this small mass splitting, the decay rate of the chargino can be suppressed, which implies a long-lived chargino.

2.2.2 Split-Supersymmetry

A different model of SUSY is split-SUSY, where the SUSY-breaking scale m_S is far above a TeV [30, 31]. The scalar superpartners in this case will have masses around m_S, but the gauginos can be protected by chiral symmetries to be lighter in mass and discoverable at the LHC. Because the decay of the gluino is mediated by a virtual heavy squark, this model can result in long-lived gluinos with lifetime [30]

$$\tau = 3 \times 10^{-2}\text{s} \left(\frac{m_S}{10^9\ \text{GeV}}\right)^4 \left(\frac{1\ \text{TeV}}{m_{\tilde{g}}}\right)^5 . \tag{2.3}$$

These long-lived gluinos, which carry color charge, will then hadronize and form composite particles called R-hadrons. A single gluino R-hadron consists of bound state of the gluino and various quarks.

Note that split-SUSY, because of the large value of m_S, does not solve the aforementioned hierarchy problem. However, it preserves other desirable properties of SUSY, including providing a dark matter particle candidate and the high-scale unification of gauge couplings [30].

2.3 Current experimental status of searches for supersymmetry

Both ATLAS and CMS, two particle physics experiments located at the LHC in Geneva, Switzerland, have conducted searches for evidence of supersymmetry since 2011. A summary of the searches as of March 2021 published by ATLAS is shown in Figure 2.4 [32].

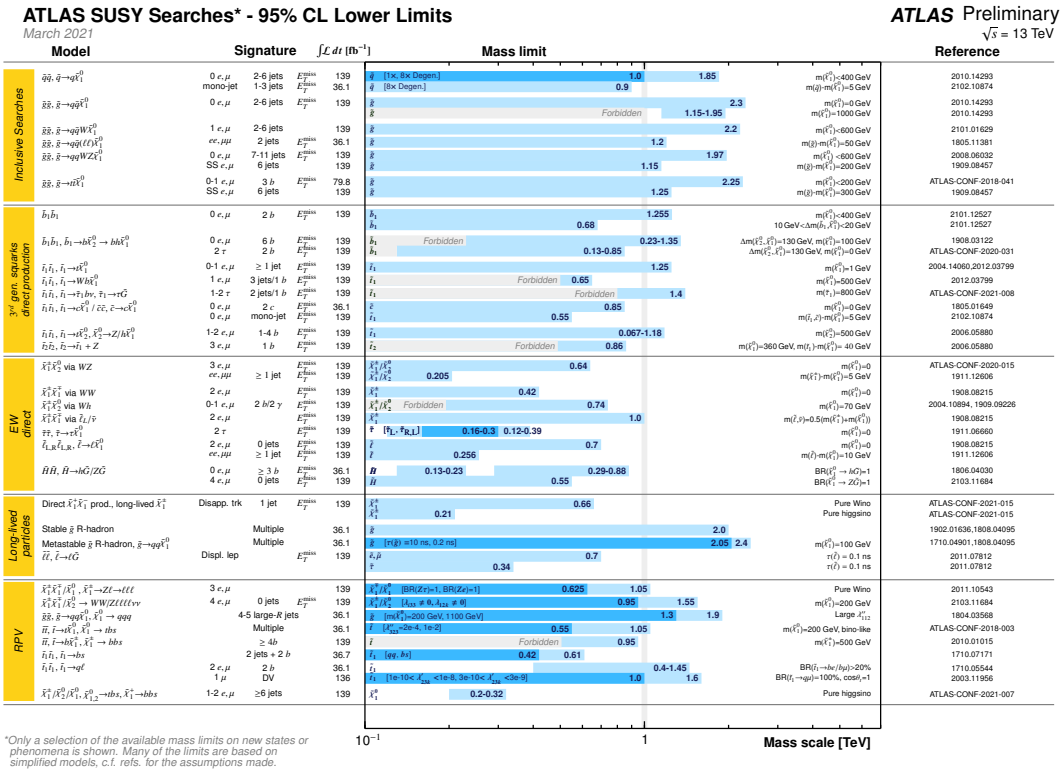

Figure 2.4: ATLAS limits on various supersymmetric models as of March 2021 [32]. Sparticle masses in the shaded blue regions in the "Mass Limit" column are excluded at 95% CL. The dark blue regions indicate that there is an extra constraint on the limit (e.g. branching ratio assumption), as specified in the brackets.

The model quoted in the first column on the figure is a *simplified model*. Simplified models are toy models in which a reduced set of constraints are used to parameterize the model. Simulated

events of the simplified models, which generally only include the production of a few sparticles, are produced to evaluate the sensitivity of each search. For example, the first model listed includes the pair production of two squarks at the LHC, where each squark decays promptly to a quark and a neutralino. In a full SUSY theory, other sparticles will be produced, but in a simplified model only a subset of sparticles are considered with sparse assumptions. Simplified models help evaluate the sensitivy of a search to different phenomenological signatures as opposed to excessively tuning to a large set of arbitrary theoretical parameters. They are used broadly across collider searches and are further described in [33].

The other columns in Figure 2.4 specify the ATLAS detector signature of each model, the size of the dataset used to search for the model, the sparticle mass range excluded by the search, and references to the results. The majority of searches look for evidence of sparticles which promptly decay to SM-like objects. A small subset of analyses look for sparticles which do not decay promptly, or are *long-lived* on the scale of the detector. A comprehensive and recent summary of the status of long-lived particles at collider experiments can be found in [34]. Searching for long-lived gluinos, sleptons, and charginos, motivated by the SUSY scenarios described in the previous section, is the focus on this thesis.

The current ATLAS limits on long-lived gluinos, which are predicted by split-SUSY scenarios, are shown in Figure 2.5 as a function of mass and lifetime. The simplified model assumes that gluinos are produced in pairs, with each gluino decaying to two quarks and a neutralino of 100 GeV. The strongest *observed* limits on gluinos with lifetimes of a few ns to $\sim$30 ns are from the 13 TeV ATLAS pixel $\mathrm{d}E/\mathrm{d}x$ analysis [35]. This analysis is the predecessor to the work described in

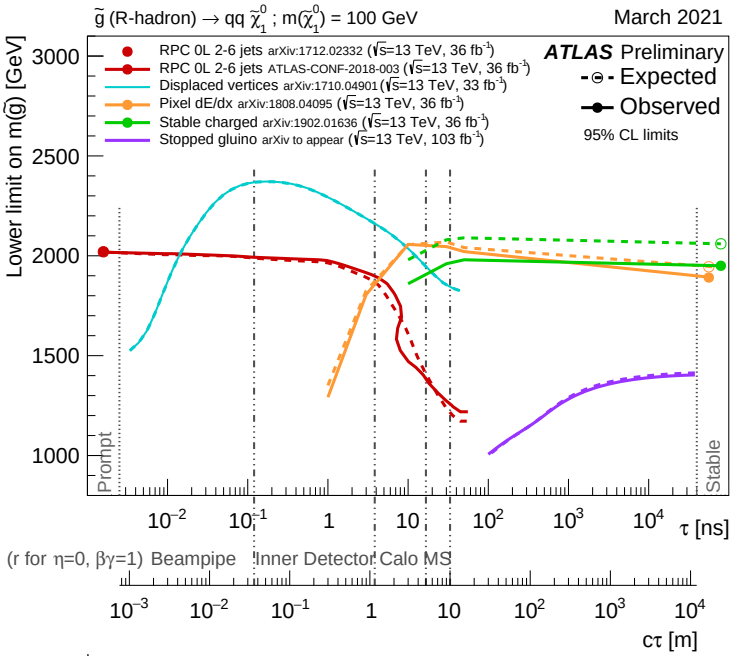

Figure 2.5: ATLAS limits on gluinos as a function of mass and lifetime as of March 2021 [32].

this thesis with 36 fb^{-}1 and looked for gluinos with a broad range of lifetimes. Gluinos with masses up to ∼2 TeVare excluded for intermediate lifetimes of $\mathcal{O}$(10 ns). Versions of the pixel $\mathrm{d}E/\mathrm{d}x$ search were also conducted with 3 fb^{-1} at $\sqrt{s}$ = 13 TeVand also at 8 TeV in ATLAS [36, 37].

The ATLAS stable charged particle analysis [38], which uses some of the custom $\mathrm{d}E/\mathrm{d}x$ measurements developed by the pixel $\mathrm{d}E/\mathrm{d}x$ analysis team combined with additional time-of-flight information, has stronger expected limits than the pixel $\mathrm{d}E/\mathrm{d}x$ analysis for longer lifetimes.† Because of the requirement of additional detector timing information, the sensitivity of the stable charged particle analysis drops off quickly with shorter lifetimes. CMS conducted a similar search

†Expected limits refer to the expected exclusion power of the analysis if the observed data in the signal regions exactly matched the predicted background.

for stable charged particles with 12.9 fb^{-1} at $\sqrt{s}$ = 13 TeVand targeted several signal models including gluinos and staus. Stable gluinos were excluded up to 1850 GeV, and pair-produced stable staus were excluded up to 360 GeV [39].

For gluino lifetimes of a fraction of a ns to a few ns, the sensitivity of the displaced vertex analysis takes over [40]. The displaced vertex analysis looks for evidence of the gluino decay products.

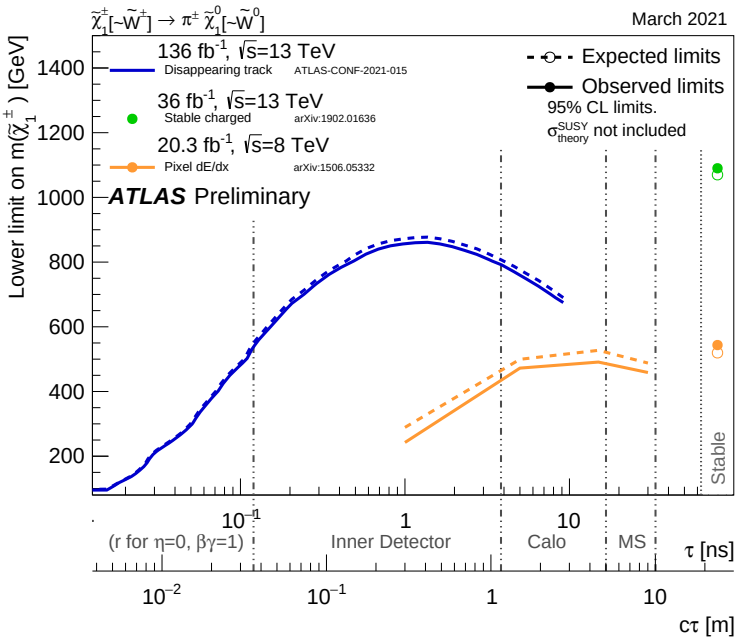

Figure 2.6: ATLAS limits on charginos as a function of mass and lifetime as of March 2021 [32].

Because of the relatively model-independent nature of this search, which will be discussed in greater detail in later chapters, the ATLAS pixel $\mathrm{d}E/\mathrm{d}x$ analysis with 36 fb^{-1} specifically looked for long-lived gluinos but also has sensitivity to long-lived charginos (and broadly to long-lived heavy charged particles in general), similar to the stable charged particle analyses. The $\sqrt{s}$ = 8 TeV version

of the pixel $\mathrm{d}E/\mathrm{d}x$ search looked for both gluinos and charginos [37]. Despite the limited dataset and lower collision energy, these limits remain the strongest ATLAS limits for charginos of intermediate lifetime, as shown in Figure 2.6. This thesis work revives the search for charginos in addition to gluinos. Furthermore, long-lived sleptons, which are predicted in GMSB SUSY models, are also targeted by this work. As shown in Figure 2.4, long-lived staus with masses up to 340 GeVand lifetimes of 0.1 ns are excluded by the displaced lepton search [41]. This thesis has sensitivity to staus with longer lifetimes.

3

The Theory of Energy Loss

The electromagnetic force is ubiquitous in the life of a particle physicist. All particle detectors rely on electromagnetism; each detector produces a current or voltage signal that we read out. Particle trackers utilize the fact that incident charged particles traveling through detector interact electromagnetically with the detector material.

One important component in understanding particle tracking is the theory of energy loss asso-

ciated to a particle traveling through the detector material. This energy loss can be in many forms including atomic excitation, ionization, and bremsstrahlung; the primary forms of energy loss at the LHC for fundamental particles heavier than an electron are ionization and atomic excitation [42]. An energy loss measurement along a particle track, combined with a track momentum measurement, can also be used to determine the mass of the particle which made the track. This type of particle identification is the basis of the work described in later chapters of this thesis.

Descriptions and formulae describing how fundamental particles interact as they travel through material can fill many books. Here we focus on the theories that are particularly relevant to this thesis with an emphasis on silicon material, using the notation shown in Table 3.1. The Particle Data Group review gives a broader overview [16].

3.0.1 Mean energy loss

The famous Bethe-Bloch equation describes the *mean* energy loss of an incident charged particle (with $m >> m_e$) traveling through a material [42]:

$$\langle \mathrm{d}E/\mathrm{d}x \rangle = \frac{2\pi k^2 n_e z^2 e^4}{m_e v^2} \left(\ln \frac{2m_e v^2 W_{\max}}{I^2(1-\beta^2)} - 2\beta^2 - \delta - U \right) [\mathrm{MeV/cm}]. \tag{3.1}$$

The definitions of the variables in this equation are shown in Table 3.1. $\langle \mathrm{d}E/\mathrm{d}x \rangle$ has units of energy over length in Equation 3.1 and is often abbreviated as $\mathrm{d}E/\mathrm{d}x$. In literature the term $\mathrm{d}E/\mathrm{d}x$ is used to refer to various quantities, including $\langle \mathrm{d}E/\mathrm{d}x \rangle$ as well as $\langle \mathrm{d}E/\mathrm{d}x \rangle/\rho$.* While $\langle \mathrm{d}E/\mathrm{d}x \rangle$

*Unless there is explicit specification of the units as [MeV $\mathrm{g}^{-1}\mathrm{cm}^2$], in this chapter $\mathrm{d}E/\mathrm{d}x$ refers to the quantity with units of [MeV/cm].

Symbol	Meaning
N_A	Avogadro's number $[\mathrm{mol}^{-1}]$
m_e	electron mass $[\mathrm{eV}/c^2]$
e	elementary charge [C]
h	Planck constant $[\mathrm{eV}\cdot\mathrm{s}]$
k	Coulomb constant $[\mathrm{N}\cdot\mathrm{m}^2\cdot\mathrm{C}^{-2}]$
n_e	electron density $[\mathrm{m}^{-3}]$
c	speed of light $[\mathrm{m/s}]$
v	incident particle velocity $[\mathrm{m/s}]$
ρ	material density $[\mathrm{kg/m}^3]$
δ	density correction term
U	shell correction term
β	$\frac{v}{c}$
γ	$\sqrt{1-\beta^2}^{-1}$
z	incident particle charge multiplier ($q = ze$)
I	mean excitation energy of material [eV]
b	impact parameter [m]
W_{max}	maximum transferrable energy in a collision [eV]
W_{tot}	total energy loss [eV]
x	incident particle path length in material [m]

Table 3.1: Notation and constants used.

is heavily dependent on the material through the density, $\langle \mathrm{d}E/\mathrm{d}x\rangle/\rho$ as a function of $\beta\gamma$ curves are minimally dependent on material and therefore is often used to describe energy loss more generically.

$\langle \mathrm{d}E/\mathrm{d}x\rangle$ (excluding the U correction) is plotted for incident particles traveling through silicon in Figure 3.1.

The derivation of Equation 3.1 includes both classical and quantum mechanical components. We note a few fundamental dependences of the equation that come from electromagnetic principles by examining the first factored term, $\frac{2\pi n_e z^2 e^4}{m_e v^2}$. $\langle \mathrm{d}E/\mathrm{d}x\rangle$ is inversely proportional to the squared

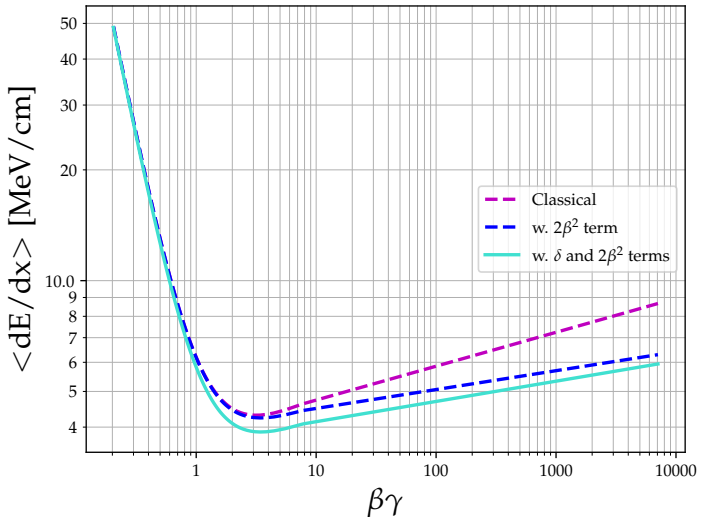

Figure 3.1: The energy loss (linear stopping power) curve as a function of $\beta\gamma$ for particles traveling through silicon.

velocity of the incident particle. This is because slower particles feel the integrated electric field of the material for a longer period of time. We also note that $\langle \mathrm{d}E/\mathrm{d}x \rangle$ is also dependent on the electron density n_e of the material and the charge of the incident particle z, which determine the strength of the electric field. A particle with a $\beta\gamma$ value that sits near the minimum of the curve in Figure 3.1 is commonly referred to as a Minimum Ionizing Particle (MIP).

To gain more intuition, it is useful to derive the classical component of this equation which was originally derived by Bohr [43]. The derivation, detailed in the following section, will follow Reference [42] and [44]. [†] A discussion of the modifications to the classical formula, or the addition of the $-2\beta^2$, δ and U correction terms, will be discussed briefly in Section 3.0.3.

[†]In References [42] and [44], the Coloumb constant k is set to 1, which is also the convention here.

3.0.2 Classical derivation of mean energy loss

Consider a particle with charge ze traveling through material with electron density n_e. To calculate $\langle \mathrm{d}E/\mathrm{d}x \rangle$, or the mean energy loss per unit path length, we can calculate the total energy loss W_{tot} and divide it by the distance x the particle travels through the material. Then $\langle \mathrm{d}E/\mathrm{d}x \rangle$ is simply W_{tot}/x.

To derive W_{tot}, we need to know (1) the energy transferred to a single electron and (2) the number of electrons that feel the field of the incident particle. The product of these is the total energy W_{tot}.

We begin by considering an incident particle of mass m, charge ze, and velocity v, which is moving along the z-axis in Figure 3.2. A single electron sits a distance b away from the z-axis. In the rest frame of the incident particle, the incident particle feels a Coulomb field from the electron at time t with transverse component $E_\perp = \frac{zeb}{\sqrt{b^2+(\gamma v t)^2}^3}$ [45].

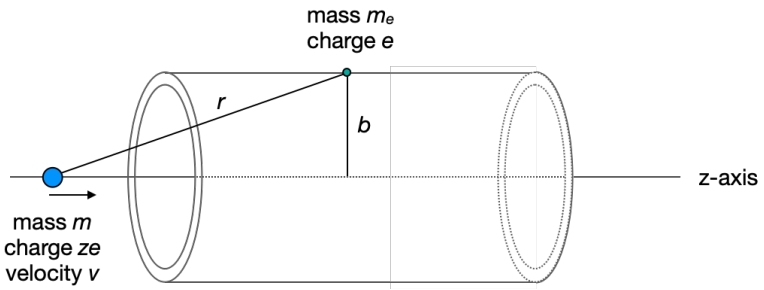

Figure 3.2: A particle is moving along the z-axis. An electron in a cylindrical slice of the of material is located a distance b from the z-axis.

If we boost to the lab frame, where the particle is moving with velocity v and the electron is at rest in the lab frame, $E_\perp$ becomes $E'_\perp = \gamma E_\perp = \gamma \frac{zeb}{\sqrt{b^2+(\gamma v t)^2}^3}$.

The impulse Δp felt by the electron is then given as

$$\begin{aligned}\Delta p &= \int F\, dt \\ &= \int eE\, dt \\ &= \int_{-\infty}^{\infty} \gamma \frac{ze^2 b}{\sqrt{b^2 + (\gamma v t)^2}^3} dt \quad = \frac{2ze^2}{bv},\end{aligned} \tag{3.2}$$

Using the expression for impulse, the kinetic energy of the electron is then

$$\begin{aligned}W &= \frac{\Delta p^2}{2m_e} \\ &= \frac{2z^2 e^4}{m_e b^2 v^2}.\end{aligned} \tag{3.3}$$

To extend this to the energy transferred to more than one electrion, let us write down the number of total electrons encountered in an infinitesimal slice of phase space. If the incident particle travels a length dx, it will encounter $dx\, n_e\, (2\pi b)\, db$ electrons that are distance b away.

Therefore the kinetic energy transferred to the electrons of the material is then

$$\begin{aligned}W_{\text{tot}} &= \int dx \int db \frac{2z^2 e^4}{m_e b^2 v^2}\, n_e\, (2\pi b) \\ &= x \int \frac{2z^2 e^4}{m_e b^2 v^2}\, n_e\, (2\pi b)\, db.\end{aligned} \tag{3.4}$$

Dividing both sides of the equation by x, we find

$$\begin{aligned}\langle \mathrm{d}E/\mathrm{d}x \rangle \equiv \frac{W_{\text{tot}}}{x} &= \int \frac{2z^2 e^4}{m_e b^2 v^2}\, n_e\, (2\pi b)\, db \\ &= \frac{4\pi n_e z^2 e^4}{m_e v^2} \ln \frac{b_{\text{max}}}{b_{\text{min}}},\end{aligned} \tag{3.5}$$

What values of b should be considered?

The maximum value of b depends on the excitability of the material, which quantifies how easily it absorbs energy from the incident particle [46]. Let us introduce the *mean excitation energy* I, which depends on the characteristic electronic transitions of the material and can be defined as

$$\ln I = \int f(\epsilon, 0) \ln \epsilon \, d\epsilon \, / \int f(\epsilon, 0) \, d\epsilon, \tag{3.6}$$

where ϵ is the energy transferred and $f(\epsilon, 0)$ is the associated dipole oscillator strength [47]. Further discussion of the dipole oscillator strength and its relation to the generalized oscillator strength and the transition matrix element for atomic excitations is discussed in Section 3.0.5.

The mean excitation energy can then be related to an excitation time τ

$$I = \frac{h}{\tau}, \tag{3.7}$$

where h is Planck's constant. The bound b_{max} is then given as

$$b_{\text{max}} \sim \frac{\gamma h v}{I}. \tag{3.8}$$

The minimum value of b is bounded by the regime where the classical assumption fails, or when b is smaller than the de Broglie wavelength of the electron (in the center-of-mass frame).

The de Broglie wavelength and therefore b_{min} is then

$$b_{\text{min}} \sim \lambda = \frac{h}{2p_e}, \tag{3.9}$$

where p_e is the electron momentum in the center of mass frame of the collision. p_e is $\gamma m_e v$ assuming the incident particle mass m is much larger than m_e.

Integrating Equation 3.5 using these bounds, we get

$$\begin{aligned} \langle \mathrm{d}E/\mathrm{d}x \rangle &= \frac{4\pi n_e z^2 e^4}{m_e v^2} \ln \frac{b_{\text{max}}}{b_{\text{min}}} \\ &= \frac{4\pi n_e z^2 e^4}{m_e v^2} \ln \frac{\gamma^2 2 m_e v^2}{I}. \end{aligned} \tag{3.10}$$

Equation 3.1 is written in terms of W_{max}, or the maximum energy transferrable to an electron. W_{max} for a particle with momentum p and mass m colliding with the atomic electron (assumed to be at rest) is [42]:

$$W_{\text{max}} = 2m_e c^2 \beta^2 \gamma^2 \left(1 + \left(\frac{m_e}{m}\right)^2 + 2\gamma \frac{m_e}{m}\right)^{-1} \tag{3.11}$$

For masses $m \gg m_e$, which is a good assumption for many of the particles produced at the LHC, this simplifies to

$$W_{\text{max}} = 2m_e c^2 \beta^2 \gamma^2. \tag{3.12}$$

Substituting this into Equation 3.10, we finally recover Equation 3.1 (with $k = 1$) up to the $2\beta^2$ term and the density and shell corrections.

3.0.3 Corrections to the classical equation

The first corrective term to Equation 3.1 ($-2\beta^2$) comes from the full quantum-mechanical derivation by Bethe [48]. The second term, the density correction term δ, comes from the fact that the material that the incoming particle travels through is polarized by the electric field of the incident particle and screens the field strength for electrons at large b [49]. The effect of these two terms can be seen in Figure 3.1. Finally, the shell correction term U takes into account the effect that the inner shell electrons do not participate much in the interactions for particles with very small $\beta\gamma$, when the incident particle velocity is comparable to the atomic electron velocity [50]. The shell correction is small for $\beta\gamma \gtrsim 0.01$ [42].

More details on these corrections as well as other corrections relevant only at low incident particle energies, including the Bloch correction [51, 52] and the Barkas effect [53], are found in [42, 50].

3.0.4 Fermi plateau

As seen in Figure 3.1, $\langle \mathrm{d}E/\mathrm{d}x \rangle$ rises as a function of $\beta\gamma$ for $\beta\gamma \gtrsim 10$. This is called the *relativistic rise* regime and comes from the dependence of W_{max} on $\beta\gamma$. This can also be interpreted as the electric field of the particle "pancaking" due to relativistic effects.

Practically, the detectable maximum energy transferred to an electron is limited by the thickness of the detector. For example, if an incident particle transfers enough energy to an electron in the material such that the electron escapes the detector, the energy loss measurement is reduced [42]. Therefore it is useful to define a constant maximum energy T_{cut} above which the transferred energy

is not measurable. Figure 3.3 shows the effect of capping W_{max} at different T_{cut} values, corresponding to detector thicknesses, which results in the ionization energy loss curve plateauing at high $\beta\gamma$ values. This is also referred to as the *Fermi plateau*.

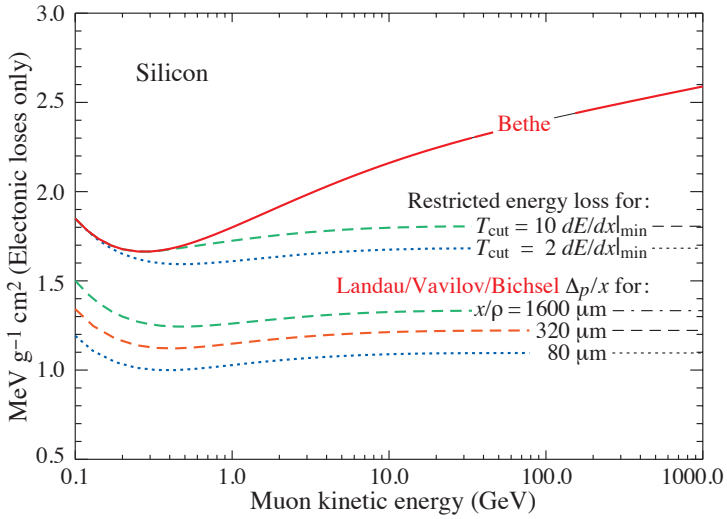

Figure 3.3: The dependence of different measures of ionization energy loss per unit path length as a function of the incident muon energy. Δ_p/x (calculated using Landau theory with modification by Vavilov and Bichsel) plateaus at a muon kinetic energy of $\approx$ 10 GeV, as do calculations of $\langle \mathrm{d}E/\mathrm{d}x \rangle$ with restricted energy loss. The $\langle \mathrm{d}E/\mathrm{d}x \rangle$ given by the Bethe-Bloch formula continues to sharply rise with increasing muon energy [16].

3.0.5 Straggling functions

Energy loss is a probabilistic phenomenon. Although the previous descriptions describe the average energy loss for particles traversing a material, a single energy loss measurement for a given particle requires a description of the probability distribution function. This function, also called a *straggling function*, was first derived by Landau in 1944 [54].

Landau derivation

Landau's original derivation [54] of the straggling function $f(\Delta, x)$, which describes the probability of losing energy Δ in thickness x, is described in the following section with some added intuition and modifications following [42]. [55] also provides a good description of the derivation.

Landau derived this function by finding the solution to an integrated transport equation. We note that there are other ways to analytically derive this function, including a commonly used method which involves performing an n-fold convolution of an expression for a single collision cross section (see [56]).

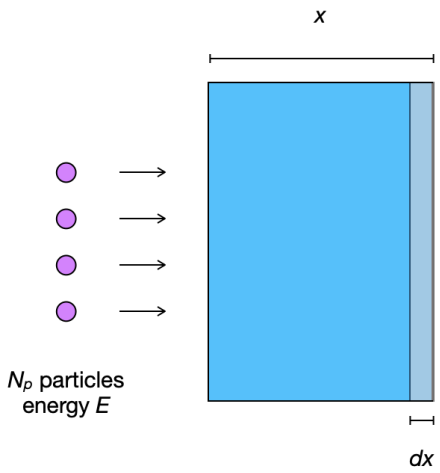

Figure 3.4: A block of material with thickness x is irradiated with N_p particles, each with energy E.

Consider N_p particles with energy E passing through a material of total thickness x (see Figure 3.4). The number of particles which have lost energy $\in [\Delta, \Delta + d\Delta]$ after traveling through x is $N_p\, f(\Delta, x) d\Delta$. Similarly, the number of particles which have lost energy $\in [\Delta, \Delta + d\Delta]$ af-

ter traveling through x and an infinitesimal slice of material with thickness dx, can be expressed as $N_p\, f(\Delta, x + dx)d\Delta$. Therefore, the *change* Δ_{N_p} in the number of particles which have lost, in total, an amount of energy between Δ and $\Delta + d\Delta$ after passing through an additional infinitesimal slice of material with thickness dx can be expressed as

$$\Delta_{N_p} = N_p\ [f(\Delta, x + dx) - f(\Delta, x)]\, d\Delta. \tag{3.13}$$

Let us consider an alternative way of expressing Δ_{N_p}:

$$\Delta_{N_p} = I_p - D_p, \tag{3.14}$$

where I_p and D_p refer to particles which "enter" and "exit", respectively, the slice of $[\Delta, \Delta + d\Delta]$ phase space. I_p is defined as

$$I_p = N_p \int_0^\infty w(E, \epsilon)\, dx\, f(\Delta - \epsilon, x)\, d\Delta\, d\epsilon, \tag{3.15}$$

where $f(\Delta - \epsilon, x)d\Delta$ is the probability that the incoming particle has already lost energy $\Delta - \epsilon$, and $w(E, \epsilon)dx$ is the probability that the particle has a collision in dx which transfers energy ϵ to the material.

D_p describes the number of particles which had lost energy between $\Delta,\ \Delta + d\Delta$ and after losing ϵ additional energy have total energy loss $\Delta + \epsilon > \Delta + d\Delta$:

$$D_p = N_p \int_0^\infty w(E,\epsilon)\, dx\, f(\Delta, x)\, d\Delta\, d\epsilon. \tag{3.16}$$

Then

$$N_p\ [f(\Delta, x+dx) - f(\Delta, x)]\, d\Delta = N_p \int_0^\infty w(E,\epsilon)\, [f(\Delta-\epsilon, x) - f(\Delta, x)]\ d\Delta\, d\epsilon\, dx. \tag{3.17}$$

Dividing both sides by $N_p\, dx\, d\Delta$ gives

$$\frac{df}{dx} = \int_0^\infty w(E,\epsilon)\, [f(\Delta-\epsilon, x) - f(\Delta, x)]\ d\epsilon, \tag{3.18}$$

Solving Equation 3.18 gives us $f(\Delta, x)$.

Note that the resulting expression for $f(\Delta, x)$ is dependent on the choice of $w(E,\epsilon)$. Landau's original derivation uses the spin-independent Rutherford cross section for collisions and assumes that the transferred energy ϵ is much less than the maximum energy W_{max} transferrable in a collision. The Rutherford collision probability $w(E,\epsilon)$ and cross section $\sigma_R(E,\epsilon)$ are defined as [42, 54, 56, 57]:

$$\begin{aligned} w(E,\epsilon) &= n_e\, \sigma_R(E,\epsilon)\ [\text{MeV}^{-1}\ \text{cm}^{-1}] \\ \sigma_R(E,\epsilon) &= \frac{2\pi e^4}{m_e v^2 \epsilon^2} \left(1 - \frac{v^2}{c^2}\frac{\epsilon}{W_{\text{max}}}\right)\ [\text{MeV}^{-1}\ \text{cm}^2]. \end{aligned} \tag{3.19}$$

Assuming that the transferred energy ϵ is small compared to W_{max}, the maximum energy trans-

ferrable, this equation reduces to:

$$w(E,\epsilon) = \frac{2\pi n_e e^4}{m_e v^2 \epsilon^2}. \tag{3.20}$$

Landau's expression for $f(\Delta, x)$ is given by the solution of Equation 3.18 with $w(E,\epsilon)$ given by Equation 3.20. Landau also took the limit of a *thin* absorber, where $W_{\max}/\frac{2\pi n_e e^4}{mv^2} \gg x$. The technical details of solving Equation 3.18, which involves taking a Laplace transform, can be found in [54]. A boundary condition of $f(\Delta, x = 0) = \delta(\Delta)$ is assumed, which can be interpreted as requiring that the incident particle has not lost any energy at the incident surface.

Finally, the Landau distribution describing the probability of losing energy Δ in thickness x is given as [54]

$$\begin{aligned} f(\Delta, x) &= \frac{\phi(\lambda)}{\xi} \\ \phi(\lambda) &= \frac{1}{2\pi i}\int_{-i\infty+c_1}^{i\infty+c_1} e^{u\ln u + \lambda u} du \\ \lambda &= \frac{\Delta - \xi\left(\ln\frac{\xi}{\epsilon'} + 1 - C\right)}{\xi}. \end{aligned} \tag{3.21}$$

C is Euler's constant, and $\xi = x\frac{2\pi n_e e^4}{mv^2}$. $\ln\epsilon' = \ln\frac{(1-v^2/c^2)I^2}{2m_e v^2} + v^2/c^2$, where I is the ionization potential.

If instead the absorber is thick and $W_{\max}/\frac{2\pi n_e e^4}{mv^2} \ll x$, the resulting solution to the transport equation is a Gaussian distribution [42, 54].

More details of the derivation can be found in [42, 54].

Comments on the Landau distribution

In practice the Landau distribution is parameterized by two parameters and then fitted to a distribution in data. λ is redefined as $\lambda = (\Delta - \mu)/\sigma$, where μ is called the location parameter and σ is called the scale parameter [58].

The Landau distribution with $\mu = 0$ and a few choices of σ is shown in Figure 3.5. The distribution is peaked with a long right tail. The emission of δ-rays results in events with energy loss Δ in the tail of the distribution. δ-rays are ionized electrons which received enough energy from the incoming particle to ionize other atoms [42].

The Landau distribution has an infinitely long tail, so the mean and variance of the distribution are undefined. The Landau distribution is also a stable distribution, which means that linear combination of two random variables X_1,X_2, drawn from two Landau distributions, will also follow a Landau distribution [59, 60].

Because the mean and variance are undefined, the most probable value is a useful parameter. Landau derived an analytical expression for the most probable value Δ_p to be [54]

$$\Delta_p = \xi \left(\ln \frac{\xi}{\epsilon'} + 0.37 \right). \tag{3.22}$$

Modifications to the Landau distribution

Vavilov modified the integration limits of Equation 3.18 to take into account the kinematic bound on Δ

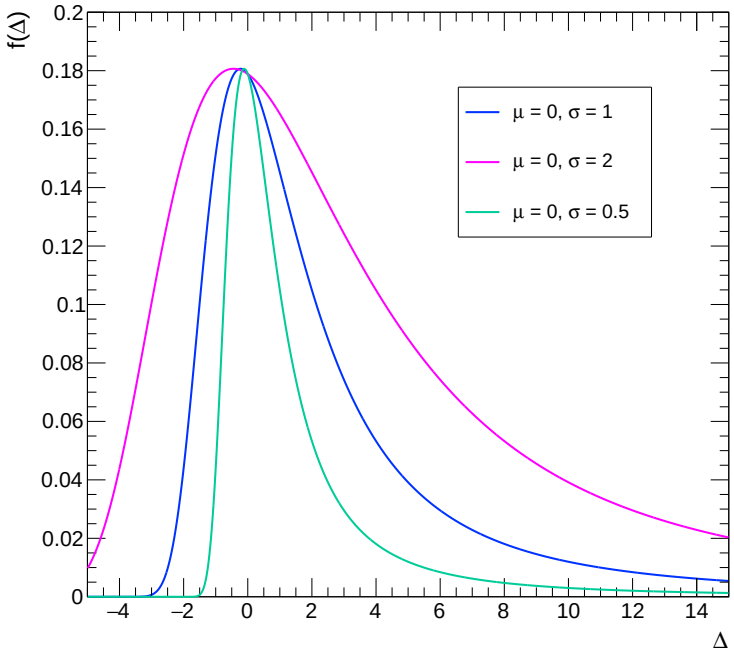

Figure 3.5: The Landau distributions with location parameter $\mu = 0$ and scale parameter $\sigma = 0.5, 1, 2$. The distributions have an infinitely long right tail.

$$\frac{df}{dx} = \int_0^u w(E,\epsilon)\left[f(\Delta-\epsilon,x) - \int_0^{W_{\max}} f(\Delta,x)\right] d\epsilon, \tag{3.23}$$

where $u = \min(\Delta, W_{\max})$ [61]. He also used the full Rutherford collision probability (Eq. 3.19). However, Equation 3.19 does not consider the effects of the electronic structure of the material on energy loss. For thin sensors where the total number of collisions is small, these details become increasingly important. Taking this into account involves modifying the Rutherford collision cross section with an inelastic form factor to account for the atomic structure. This is the approach taken in the Bethe-Fano method [50] and shows excellent agreement with experiment for thin sensors and results are summarized in Section 10 of Reference [56].

In the Bethe-Fano method, the Rutherford collision cross section is modified as follows [56]

$$\sigma(\epsilon, Q) = \sigma_R(\epsilon)\, f(\epsilon, \vec{K})\, \epsilon/Q, \tag{3.24}$$

with $Q = |\hbar\vec{K}|^2/2m_e$. $\sigma_R(\epsilon)$ is the Rutherford collision cross section, $\vec{K}$ is the momentum transfer vector, and $f(\epsilon, \vec{K})$ represents the generalized oscillator strength.[‡]

The generalized oscillator strength term can be conceptually viewed to contain the transition probabilities for the material excitations and ionizations. In other words, $f(\epsilon, \vec{K})$ is defined as

$$f(\epsilon, \vec{K}) = \frac{\epsilon}{Q}\,|F(\epsilon, \vec{K})|^2, \tag{3.25}$$

[‡]Equation 3.24 is the non-relativistic cross section; the relativistic extension can be found in Reference [56].

where $F(\epsilon, \vec{K})$ is the material transition matrix element [56]. [§]

Figure 3.6 shows the ratio of the collision cross sections of these modified models with the Rutherford cross section for incoming particles with $\beta\gamma = 0.316$. The effect of the electronic structure is clearly visible in the ratio, which exhibits a multi-peak structure.

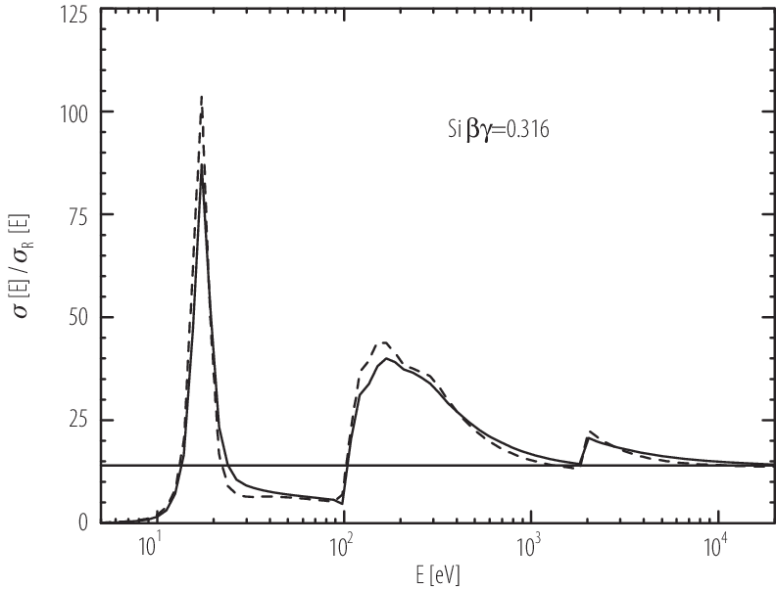

Figure 3.6: The ratio of the collision cross sections as a function of energy loss E using the Bethe-Fano model (solid line) and the Fermi Virtual Photon model (dashed line) with respect to the Rutherford collision cross section, for silicon. The peaks come from the shell structure of the silicon electrons. The incoming charged particle is fixed to have $\beta\gamma = 0.316$ [56].

The straggling functions calculated with the Bethe-Fano model compared to the Landau model with the simplified Rutherford cross section are shown in Figure 3.7. The function calculated with the Bethe-Fano model for a 300 μm silicon sensor is significantly broader than the function calcu-

[§]A simplification of the Bethe-Fano theory involves replacing the generalized oscillator strength term with the dipole oscillator strength. This is called the Fermi-virtual-photon theory, or the photo-absorption ionization model described by Allison and Cobb [62]. The dipole oscillator strength is the limit of $\vec{K} \to 0$ of the generalized oscillator strength and is more easily measured in experiments [56].

lated with the Landau model with the Vavilov modification.

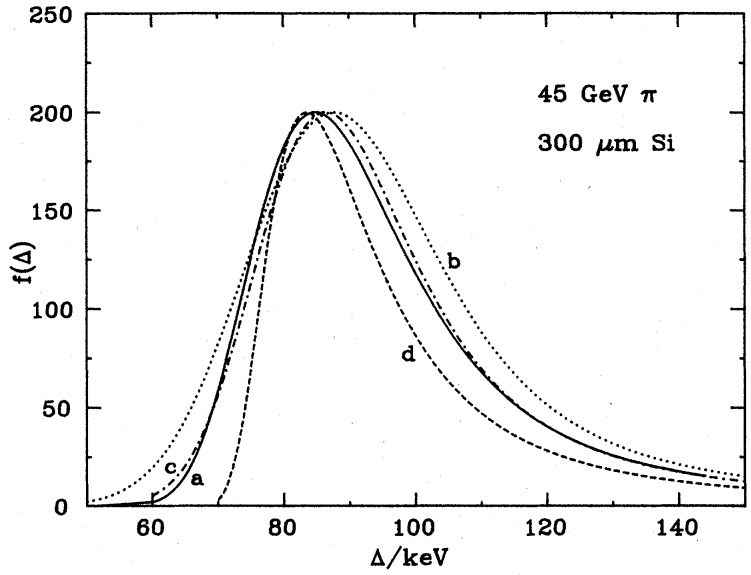

Figure 3.7: The straggling function $f(\Delta, x)$ for silicon, where x = 300 μm, using the Bethe-Fano model (line a) and the Landau-Vavilov model (line d). The Landau-Vavilov model significantly underestimates the width of the straggling function. Lines b, c are calculated using an alternative model (Shulek) [63].

Table 3.2 compares the most probable value (Δ_p) and full width at half maximum (w) of the straggling functions using the two different theories for a range of silicon sensor thicknesses. For $\approx$ 100 μm thick silicon sensors, Δ_p only differs by $\approx$ 5%, but w differs by $\approx$ 50%. An in-depth comparison of the Bethe-Fano model with the Landau model can be found in Reference [63].

More details about the modifications to the Landau model can be found in Reference [56].

x (μm)	Δ_p (keV)	r_p	Δ_p/x	w (keV)	r_w
10	1.857	0.844	186	1.758	2.465
160	43.38	1.006	272	18.32	1.606
320	90.96	1.008	285	31.54	1.382
1280	393.2	1.002	307	103.01	1.128

Table 3.2: The most probable value Δ_p and the full width at half maximum w of the straggling function for different silicon thickness x, with incident particles of $\beta\gamma$ > 500. The values of Δ_p/x and the ratio of Δ_p (r_p) and w (r_w) calculated with the Bethe-Fano model and the Landau model are also provided. Table adapted from Tables 5 & 6 in Reference [63].

A discussion on mean versus most probable value

In the Bethe-Bloch equation, $\mathrm{d}E/\mathrm{d}x$ refers to the mean energy loss per unit path length $\langle \mathrm{d}E/\mathrm{d}x \rangle$. The remainder of this thesis describes a searching using a track ionization energy loss measurement. The experimental quantity, defined later in Chapter 6, is the mean of a subset of the lowest charge measurements along the track, which is an estimator for the *most probable value* Δ_p of the energy loss distribution. The details of the algorithm are discussed in Chapter 6.

The motivation of choosing the most probable value as the estimator is because the mean energy loss per unit path length $\langle \mathrm{d}E/\mathrm{d}x \rangle$ lies in the tail of the straggling function. As discussed in Reference [16], $\langle \mathrm{d}E/\mathrm{d}x \rangle$ is pulled to large values by rare tail events and is not a useful experimental quantity, particularly when there are only a handful of measurements per particle. Figure 3.8 shows the position of the mean energy loss per unit path length overlaid on the various straggling functions for silicon sensors of different thicknesses. $\langle \mathrm{d}E/\mathrm{d}x \rangle$ is $\gtrapprox$ 40% larger than Δ_p.

A consequence of choosing Δ_p/x as the $\mathrm{d}E/\mathrm{d}x$ estimator is that while <$\mathrm{d}E/\mathrm{d}x$> is independent of sensor thickness, Δ_p/x is dependent on sensor thickness. The effect of this is later discussed

in Chapter 6.

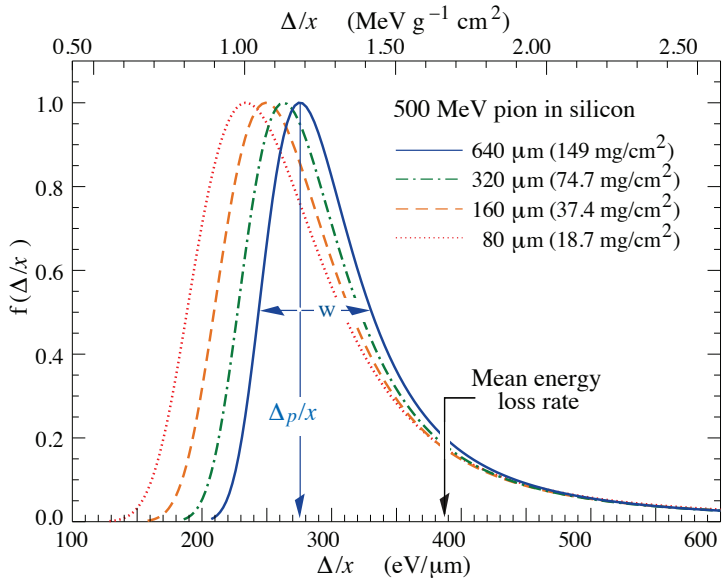

Figure 3.8: The straggling function $f(\Delta, x)$ for silicon for various thicknesses. The functions are normalized to equal 1 at the most probable value. The mean energy loss per unit path length is independent of thickness and lies in the tail of the distribution. The most probable value per unit path length, Δ_p/x, shows a clear dependence on thickness [16].

Another consequence of choosing Δ_p/x as the $\mathrm{d}E/\mathrm{d}x$ estimator is that the experimentally measured $\mathrm{d}E/\mathrm{d}x$ will plateau at large $\beta\gamma$. Δ_p/x plateaus for $\beta\gamma \gtrapprox 10$, while $\langle \mathrm{d}E/\mathrm{d}x \rangle$ continues to rise, as shown in Figure 3.3. This minimizes the correlation between $\mathrm{d}E/\mathrm{d}x$ and momentum at high $\beta\gamma$ values.

3.1 Summary

The mean energy loss of a charged particle moving through material is described by the Bethe-Bloch formula in Equation 3.1. The first term of the equation was derived classically by Bohr [43], and

since then there has been a long history of corrections. The straggling function, or probability distribution function of a single energy loss measurement as opposed to the mean loss, was first derived by Landau [54] and later modified to more accurately describe experimental data. Modern straggling function models include the Bethe-Fano model and the photo-absorption ionization model (also called the Fermi-Virtual-Photon model) [50, 56, 62]. These deviate from the original Landau model when the material traversed is relatively thin.

4

The LHC and the ATLAS Experiment

The Large Hadron Collider, located on the border of Switzerland and France, is the highest energy particle collider ever built. Protons are collided at a center-of-mass energy of 13 TeVto probe physics at the smallest distance scales. There are four major experiments situated at various points along the LHC ring which examine the particles that come out of these high energy collisions. The data described in this thesis is collected from one such experiment, the A Toroidal LHC Apparatus exper-

iment.

ATLAS is one of two *general-purpose* detectors, consisting of subsystems built to measure electrons, photons, hadrons, and muons originating from LHC proton-proton collisions. Many design aspects of the detector were optimized to look for the Higgs boson, which was discovered in 2012 by both ATLAS and the CMS, the other general-purpose detector [8, 9]. A Higgs boson produced in the LHC collisions will decay before reaching the beampipe. ATLAS was designed to precisely measure the Standard Model decay products of the Higgs boson in order to reconstruct the Higgs mass peak.

ATLAS is not optimized for a direct detection search for heavy new particles using $\mathrm{d}E/\mathrm{d}x$. The small number of measurements available for the $\mathrm{d}E/\mathrm{d}x$ measurement of each particle, as well as the limited $\mathrm{d}E/\mathrm{d}x$ resolution, is evidence of this. Despite this fact, ATLAS remains a powerful tool for the analysis described by this thesis, in part due to its excellent momentum resolution and its ability to identify Standard Model processes.

4.1 The Large Hadron Collider

The CERN accelerator complex accelerates two counter rotating proton beams up to a center-of-mass energy of 13 TeV using a series of increasingly powerful machines. Protons are sourced from a small bottle of hydrogen gas and accelerated to 50 MeV by a linear accelerator (Linac 2). These protons are then injected into the Proton Synchrotron Booster (PSB), where they are accelerated to 1.4 GeV, and then passed to the larger Proton Synchrotron (PS). By the time they reach the Super

Proton Synchrotron (SPS), the protons have an energy of 25 GeV, and the SPS accelerates them to 450 GeV. The final accelerator, the LHC, accelerates the two proton beams each to 6.5 TeV [64].

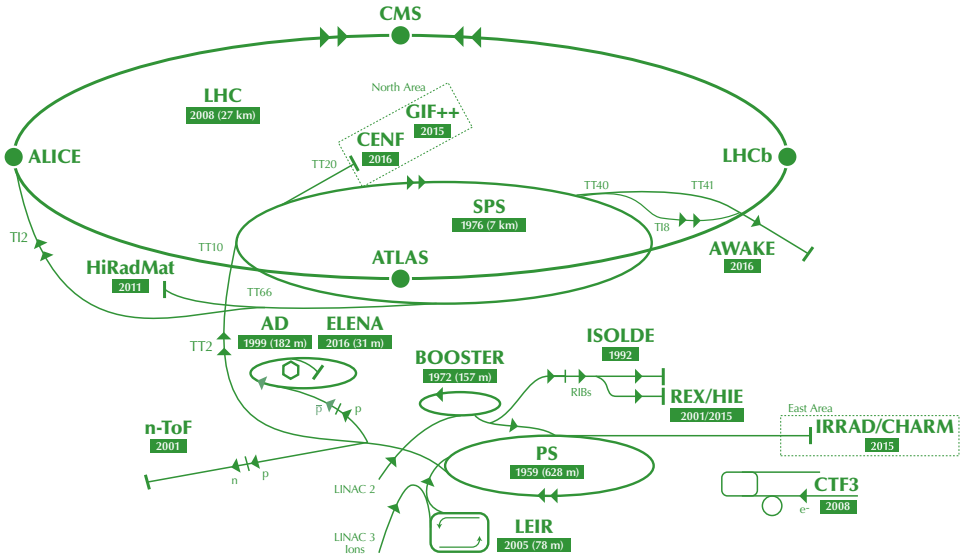

Figure 4.1: The CERN accelerator complex [64].

There are numerous challenges associated with accelerating particles to such high energies. Arguably the most difficult aspects of reaching TeV-scale energies are governed by the classical equation which arises from equating the centripetal force with the magnetic force felt by a particle of charge q traveling with velocity v in the magnetic field B:

$$p = q\,r\,B, \tag{4.1}$$

where p is the particle momentum and r is the orbit radius. From this relation it can be seen that to keep the particles in their circular orbit as they are being accelerated, either a strong magnetic field or

a very large orbit is required.

To keep down the cost and complexity of building a large accelerator, superconducting dipole magnets with ∼8 Tesla fields are used to bend the protons as they circulate in the LHC. There are 1232 dipoles situated along the ring, with an additional 392 quadrupoles to focus the proton beams [64]. With 8 Tesla magnets, the LHC needs to have a radius of about 3 km to keep the highly energetic protons in orbit. The protons are accelerated using eight radiofrequency cavities per beam which accelerate the protons with synchronized oscillating electromagnetic fields [64]. A full description of the technical design of the LHC can be found in [65].

An important aspect of the LHC design is that the proton beam is not a continuous beam of protons but a series of bunches resulting from the acceleration in the radiofrequency cavities. A single bunch contains $\sim 10^{11}$ protons [64]. These bunches are collided at a frequency of 40 MHz and often result in more than one proton-proton collision per *event*, where an event is defined as an instance of the two proton bunches crossing. Any collisions in the event which are not the most energetic inelastic collision are referred to as *pile-up*.

The most recent data-taking period of the LHC, referred to as Run-2, was from 2015-2018. The dataset collected by ATLAS during this run is used in this thesis.

4.2 Overview of ATLAS

The ATLAS experiment is a cylindrical detector centered around the *interaction point*, or the point where the accelerated protons collide. The detector layout follows that of other general-purpose de-

tectors; the innermost layers make up the tracking subsystem, which is surrounded by an electromagnetic and hadronic calorimeter. A solenoidal magnet lays inside the calorimeters to bend charged particles traversing the inner tracking subsystem. A muon spectrometer sits on the outskirts, providing another momentum measurement for muons with the bending power of a separate toroidal magnet system. An illustration of the ATLAS detector is shown in Figure 4.2.

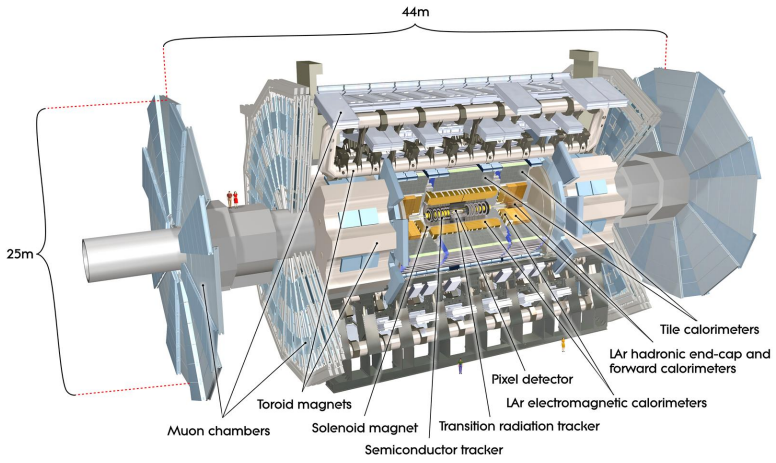

Figure 4.2: The ATLAS detector and its subsystems [66].

The coordinate system used by ATLAS is defined with the beam axis as the z-axis and is shown in Figure 4.3. The polar angle θ is measured with respect to the z-axis, as is the azimuthal angle ϕ. The cartesian coordinates x and y are defined such that $+y$ points towards the sky and $+x$ points towards the LHC ring center [67]. r is defined as $r = \sqrt{x^2 + y^2}$. The $x - y$ plane at $z = 0$ splits the ATLAS detector in two parts: the C-side and the A-side. The A-side is the side closer to the airport in Geneva, Switzerland.

In a proton-proton collider, the momentum fraction that each parton in a proton carries is not

known. As a result, we use transverse variables. The *pseudorapidity* η, which is defined as $\eta = -\ln \tan\frac{\theta}{2}$, is often used in place of θ. Pseudorapidity is the massless approximation of *rapidity*, or $y = \frac{1}{2}\ln\frac{E+p_z}{E-p_z}$, which has the useful property that differences in rapidity Δy are Lorentz invariant under boosts along z. $\eta = 0$ is equivalent to $\theta = 90°$, and $\eta = \infty$ is equivalent to $\theta = 0$.

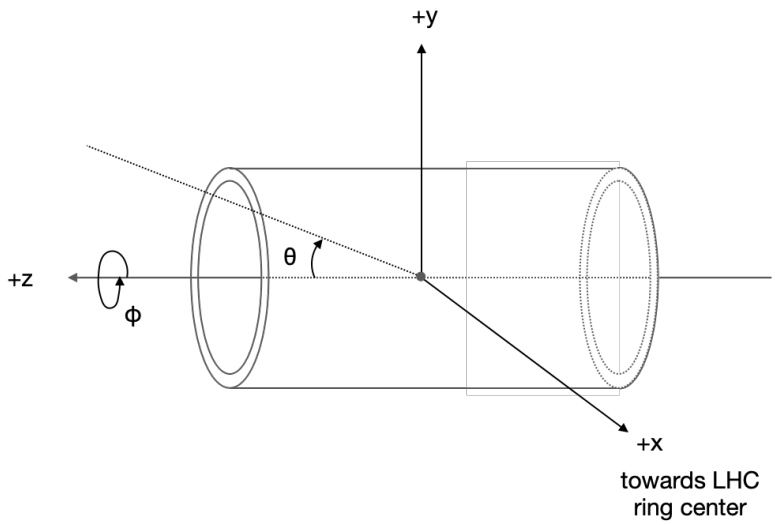

Figure 4.3: The ATLAS coordinate system.

The detector is subdivided into the *barrel* and *endcap* detectors. The barrel detector measures tracks at small values of η (typically up to $|\eta| \sim$ 1-1.8 although this number varies depending on the subsystem). The endcap detector measures forward tracks at large values of η (typically from $|\eta| \sim$ 1-1.8 to 2.5-3.2). The calorimeter system also has a forward section which spans $3.1 < |\eta| < 4.9$.

4.3 Inner Detector

The Inner Detector (ID), which is the innermost tracking system, consists of three subsystems: the pixel detector, the Semiconductor Tracker (SCT), and the Transition Radiation Tracker (TRT). A slice of the ID is shown in Figure 4.4. The pixel detector is the closest to the interaction point and spans $r = 33.25$ to 122.5 mm. It is composed of small pixels ($\mathcal{O}(100\mu\text{m})$) to resolve the many tracks coming from the interaction point. The next detector, the SCT, spans $r = 299$ to 514 mm and is composed of detector layers covered in silicon strips, while the final detector, the TRT, is a tracker composed of straw tubes.

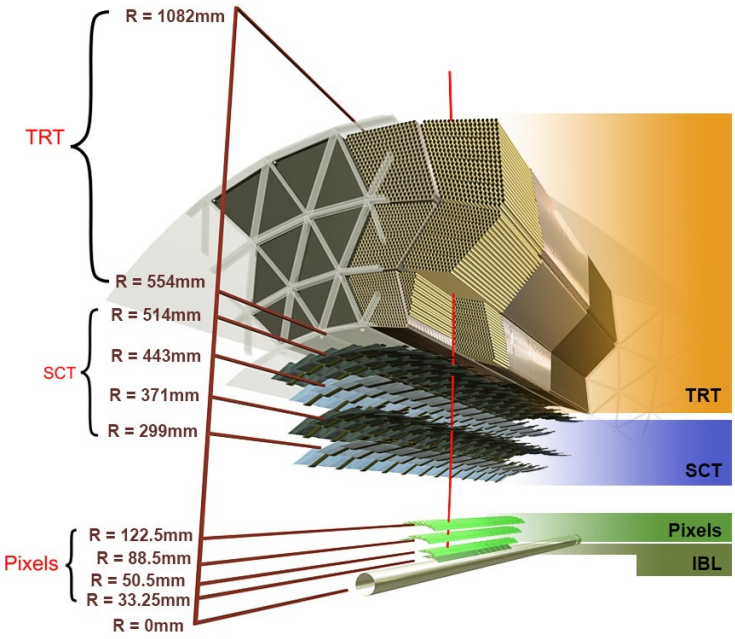

Figure 4.4: A cross-section of the ID [68, 69].

4.3.1 Pixel Detector

The working principle of the pixel detector is like that of most tracking technologies. A charged particle traversing the active material, or sensor, will ionize the material and produce, for a minimum ionizing particle, about 80 primary electron-hole pairs per micron of silicon traversed. A voltage is applied to the sensor, causing the electrons and holes to drift and induce a signal on the pixel electrode. The induced current is processed with front-end electronic circuitry, which typically amplifies and shapes the signal before extracting a measurement of the time and charge of the signal.

The pixel detector is arranged in four layers, where each layer provides a precision three-dimensional measurement of the particle trajectory. The innermost layer is called the Insertable B-Layer (IBL) and was inserted between the first and second runs of the LHC. The IBL has a distinct design and is discussed in Section 4.3.1. The three other pixel layers were installed before the first run and have a shared design. These layers, in increasing radius, are referred to as the B-Layer, Layer-1, and Layer-2 as shown in Figure 4.6.

Original Pixel Layers

The basic detector unit of each pixel layer is called a *module*, shown in Figure 4.5. A module consists of the aforementioned sensor (the active material), front-end electronics to read out the sensor signals, and a *flex-hybrid* board for signal routing and control. Each sensor is made of 250 μm-thick n^+-in-n type silicon. For each module, the sensor is bump-bonded to and read out by 16 front-end chips. The front-end chip (`FE-I3`) contains 2880 pixel cells, each with a charge preamplifier and

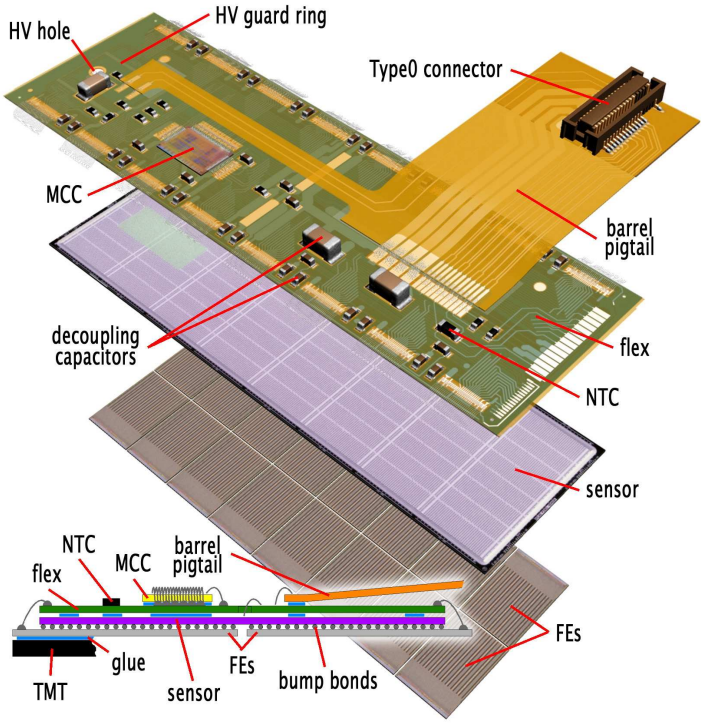

Figure 4.5: The components of a barrel pixel module are shown. The module consists of a sensor sandwiched in between a flex-hybrid board and 16 front-end electronic chips. The front-end chips are bump-bonded to the sensor. The flex-hybrid board provides low voltage to the front-end chips [70].

discriminator [70].

To provide a precise spatial measurement, a single pixel spans only 50 μm in $r-\phi$ and 400 μm in r, z (with a few exceptions). The Time Over Threshold (ToT) of the signal in each pixel is measured and recorded in increments of a 40 MHz clock. The ToT is measured with a range of 8 bits; if the ToT exceeds this range, no information is recorded [71]. The ToT is then converted to a charge value used in the $\mathrm{d}E/\mathrm{d}x$ measurement, as discussed in Chapter 6.

Each pixel layer in the barrel is divided into two carbon-fiber half-shell structures, which each support a set of *staves*. A stave is defined as a mechanical support for a set of 13 modules. Each pixel layer in the end-cap is divided into eight *disk sectors*, which serve a similar purpose to the staves. A disk sector supports six modules [70].

The number of pixels across the three layers sum to be approximately 67 million electronic channels in the barrel detector and 13 million electronic channels in the endcap detector. The active area is around 1.73 m^2, with coverage up to $|\eta|$=2.5 [70]. The pixel spatial resolution is $\sim$10 μm in $r-\phi$ and $\sim$115 μm in r, z [67].

Insertable B-Layer

The innermost layer of the ID at r = 33.25 mm was inserted before the start of the second LHC run, coinciding with the installation of a new beam-pipe. This layer, called the IBL, added a fourth tracking measurement and another charge measurement to the already existing pixel layers used in the $\mathrm{d}E/\mathrm{d}x$ measurement per track. The IBL is composed of 14 staves which each contain 20 modules (see Figures 4.7 and 4.8). The length of the active area of a stave is about 6 cm in z.

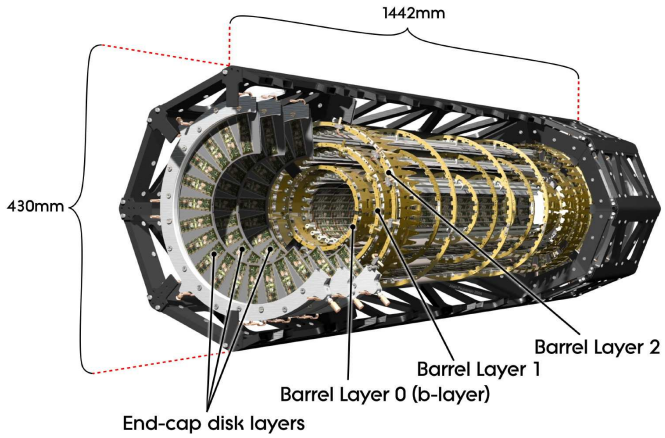

Figure 4.6: The pixel detector consists of three barrel layers and three end-cap layers capping each side [70].

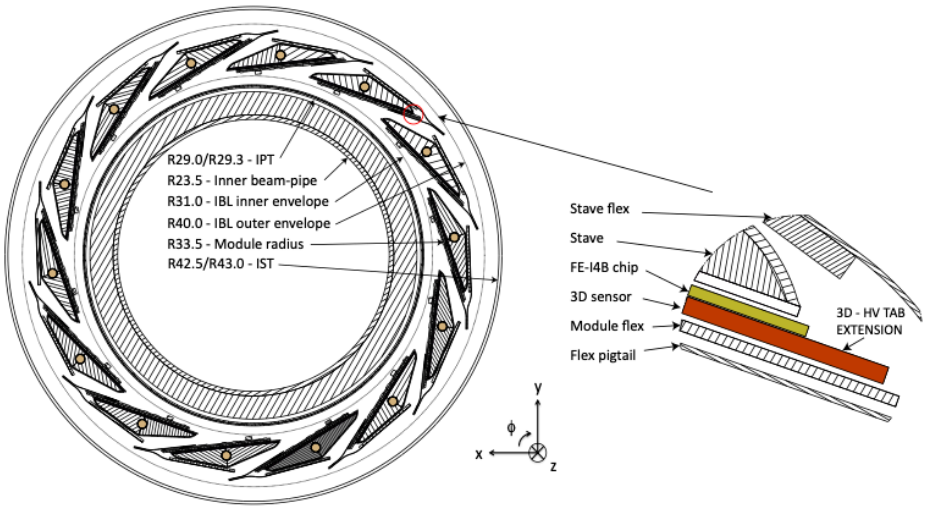

Figure 4.7: The IBL layout in the r — ϕ plane is shown. The 14 staves overlap in ϕ and are sandwiched by the inner positioning tube (IPT) and the inner support tube (IST). A close-up of a portion of a stave shows the detector components [72].

Unlike the other three pixel layers, the IBL has *two* sensor technologies: planar and 3D. The IBL planar sensors are an improved version of the sensors on the non-IBL layers with a larger fraction of active sensor area. The 3D sensors are made of a special radiation-hard technology and are used only at large η from $\sim$2.7-3. This technology incorporates the use of columnar electrodes which lay perpendicular to the surface of the sensor. This geometry causes the ionized electrons and holes to drift parallel to the surface and reduces the drift time and depletion voltage [72].

Planar modules have planar-type sensors (200 μm-thick) bump-bonded to two front-end chips per module. 3D modules have 3D sensors (230 μm-thick) bump-bonded to one front-end chip per module. Both types of modules have a flex-hybrid board and are read out with an updated version of the `FE-I3` chip, `FE-I4`. Each `FE-I4` chip contains 26,880 50 μm $\times$ 250 μm pixels and with a ToT resolution of 4 bits [72].

The IBL spans 0.15 m^2 of active area with over 12 million electronic channels, with coverage up to $|\eta| = 3$ [72].

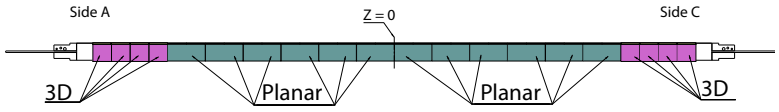

Figure 4.8: The position of planar and 3D sensors along the z-axis in the IBL for a single stave [72].

4.3.2 Semiconductor Tracker

The SCT consists of 4 layers in the barrel and 18 disks in the endcap, 9 per side. It has rougly 6 million channels and provides coverage up to $|\eta|$=2.5 [73].

An SCT module is composed of silicon sensors covered by readout strips with 80 μm pitch. In the barrel, modules are composed of two connected sensors on each side. Each pair of connected sensors is composed of 768 strips. The strips on each side are offset by an angle of 40 mrad to provide a measurement of both the precision and non-precision coordinate. In the endcap, modules also have two connected sensors on each side, with the exception of the innermost rings which have one per side. In both the barrel and endcap, sensors are made of 285 μm-thick p-in-n type technology and are capacitively coupled to the readout strips [73].

Each sensor is read out by 6 front-end ABCD chips as shown in Figure 4.9. An ABCD chip has 128 channels which output binary signals [73]. The SCT provides four three-dimensional measurements for a particle traversing the detector, where each measurement requires two hits from each layer.

The SCT in principle has some limited ability to probe $\mathrm{d}E/\mathrm{d}x$ in a similar manner to the pixel detector. The binary output, which indicates whether or not a signal was above a set threshold, is recorded for three ticks of the LHC bunch cross clock (25 ns) [73]. However, the 4 and 8-bit ToT measurements in the pixel detector have much better precision.

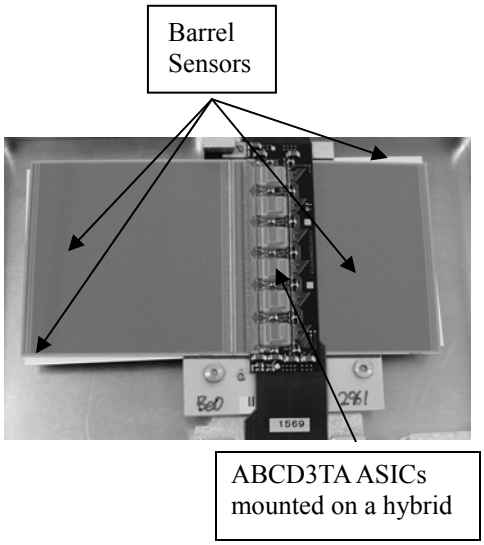

Figure 4.9: A picture of an SCT barrel module. Two layers of sensors are visible, where the bottom layer is tilted at a slight angle with respect to the top layer. Six ABCD readout chips are mounted over the right sensor [74].

4.3.3 Transition Radiation Tracker

The TRT is composed of straw tubes made of kapton and carbon fiber with 31 μm diameter gold plated tungsten wire strung in the middle. Each tube is 4 mm in diameter and has a bias voltage of -1530 V applied to the walls. There are 52,544 straws in the barrel and 245,760 straws in the end-cap regions which cover up to $|\eta| = 2.0$. Each straw is a drift chamber and is filled with 70% argon or xenon, 27% CO_2, and 3% O_2. Xenon was used in the first LHC run but replaced with argon in some regions with significant gas leaks for the second run. The straws are surrounded by a sea of polypropylene and polyethylene fibers, which serve as the *radiator* material [75].

Similar to the working principle in the silicon detectors, charged particles ionize the gas within

the straw tubes to produce 5 or 6 primary electron-ion pairs. These electrons and ions drift due to an applied electric field. However, the electric field of the drift tube is stronger near the tungsten wire, so the electrons initiate an avalanche of ionization as they approach the wire. The straw tubes have a *gas gain*, defined as the charge multiplication factor due to the avalanche process, of about 2.5×10^4 [75].

In addition to the ionization signal, *transition radiation* is emitted as charged particles move across the boundary of the radiator material. Transition radiation can be understood qualitatively by considering the electric fields in the two different materials as a charged particle moves through. They are necessarily different due to differing material properties, and Jackson describes how the differences resolve themselves at the boundary: "...the fields must reorganize themselves as the particle approaches and passes through the interface. In this process of reorganization some pieces of the field are shaken off as transition radiation" [45].

The probability of producing transition radiation depends on the Lorentz γ of the charged particle. As charged particles move through the different media in the TRT, emitted transition radiation photons which can be used to distinguish electrons from other particles with smaller γ.

In the barrel, the straws are parallel to the z-axis, while in the endcap the straws are perpendicular to the z-axis and are radially pointing. The straw signals, which have a transition radiation contribution and an primary ionization contribution, are compared against low and high thresholds. The Low Level (LL) threshold crossing time is used to reconstruct the drift circle of the charged particle, while the High Level (HL) threshold tags electrons which produce large amounts of transition radiation.

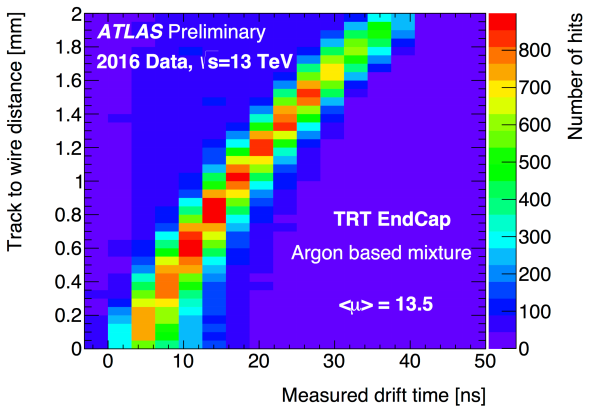

Figure 4.10: An example of the r-t relation for the TRT endcap detectors for tracks with $p_{\mathrm{T}} > 2$ GeV, ≥ 1 silicon hit and ≥ 10 TRT hits [76].

To determine the drift circle of the incoming particle, the drift time is measured as the time between the LHC bunch cross clock and the leading edge of the signal above the LL threshold, corrected by shifts due to signal propagation delay, time walk, and the particle time of flight. The drift time can then be converted to a drift radius with a calibrated r-t relation like that shown in Figure 4.10.

The straw $r - \phi$ spatial resolution is $\sim$130 μm [67]. Due to the high pile-up conditions and the high rate conditions of Run 2, the occupancy of the TRT detector can be as high as $\sim$90% (see Figure 4.11), resulting in significant efficiency losses. However, the TRT provides a large number of measurements ($\sim$30) to the track momentum measurement [75]. More details about the TRT can be found in [75].

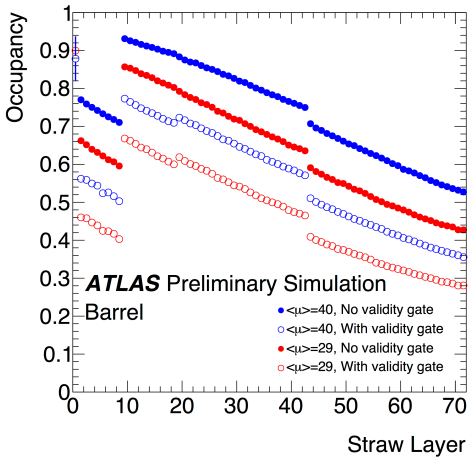

Figure 4.11: The TRT hit occupancy for various straw layers in the barrel, simulated at average pile-up $\langle\mu\rangle = 29$ and $\langle\mu\rangle = 40$. The points with a validity gate applied are calculated with a restricted time window of acceptance (28.125 ns) with respect to the 75 ns readout window. The restricted time window is used to filter hits during reconstruction. Note that the first 9 layers contain shorter straws and therefore have reduced occupancy [76].

4.4 Magnetic Field

The ATLAS magnet system consists of four superconducting magnets: a solenoid, a barrel toroid, and two endcap toroids. The magnetic field strength, along with the spatial resolution of the tracking detectors, determine the ability of ATLAS to measure the momenta of charged particles.

The solenoid sits outside of the ID and bends charged particles in ϕ as they pass through the ID. The toroids sitting within the Muon Spectrometer (MS) bend charged particles which make it to the muon system in η.

The radial and axial magnetic field components in the ID are shown in Figure 4.12. The axial magnetic field is ~ 2 Tesla at $z = 0$ and decreases at the end of the longitudinal boundary of the solenoid [67].

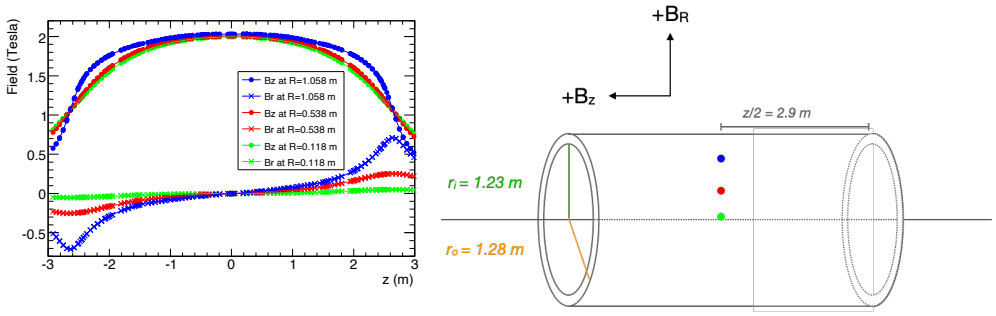

(a) Field map

(b) Solenoid layout

Figure 4.12: The (a) radial and axial magnetic field components of the field in the ID [67], shown for various values of r within the solenoidal magnetic field. (b) is a cartoon of the solenoid with the colored points corresponding to the r values in (a).

The magnetic fields in the muon subsystem vary substantially as a function of detector region: the strength in the barrel toroid ranges from 0.15 to 2.5 Tesla, while the strength in the endcap toroids ranges from 0.2 to 3.5 Tesla [67]. Figure 4.13 shows the variation in the bending power as a function of ϕ and η for the muon momentum measurement. The relevant quantity plotted is the toroidal magnetic field integrated over the path length traversed by an infinite momentum muon through the Monitored Drift Tube (MDT) chambers.

4.5 Calorimeter System

ATLAS has both an Electromagnetic (EM) calorimeter and a hadronic calorimeter to measure particle energies. The calorimeter system is divided into a barrel system and an endcap system, with an additional forward region from $3.1 < |\eta| < 4.9$ [77]. In the barrel, the EM calorimeter is a sampling calorimeter with lead absorber plates and Liquid Argon (LAr) as the active material. The hadronic

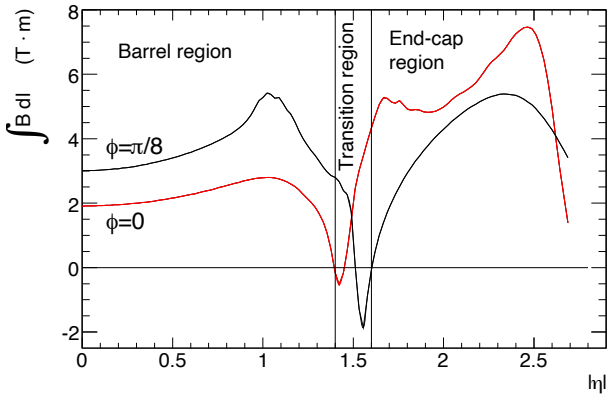

Figure 4.13: The predicted bending power varies as a function of $|\eta|$ and ϕ. The bending power is the magnetic field integrated across the path length an infinite momentum muon traverses through the MDT chambers [67].

calorimeter, or Tile Calorimeter (TileCal), is also a sampling calorimeter but instead composed of steel absorber plates and scintillating tiles as the active material [78]. A LAr-based hadronic system is also used in the endcap region with copper absorbers [77]. The spatial division of the calorimeters is shown in Figure 4.14.

The TileCal, composed of a central barrel region and two extended barrel regions, extends up to $|\eta| = 1.7$. It is 7.4 nuclear interaction lengths (λ) thick. Alternating steel plates and scintillating tiles make up the bulk of the three-layer calorimeter. After the primary particle showers in the absorber and produces secondary particles, as those secondary particles traverse the scintillator, the resulting scintillating light is shifted and guided to a Photomultiplier Tube (PMT) with a wavelength shifting fiber. The PMTtransforms the light signal into an amplified electrical signal.

A slice of the TileCal is shown in Figure 4.15. The basic cell of the TileCal covers $\Delta\eta \times \Delta\phi = (0.1 - 0.2) \times \pi/32$ in the transverse plane.

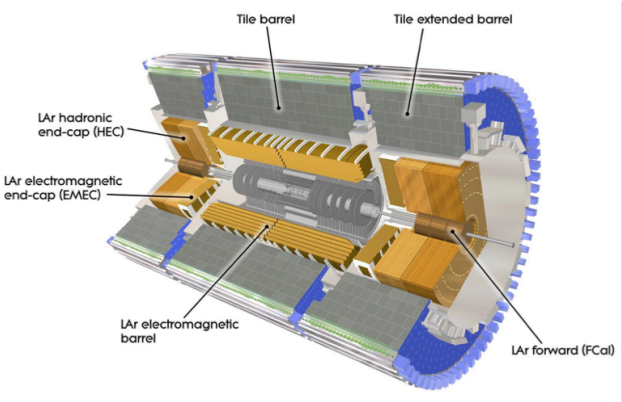

Figure 4.14: An illustration of the ATLAS calorimeters which are situated around the ID system [78].

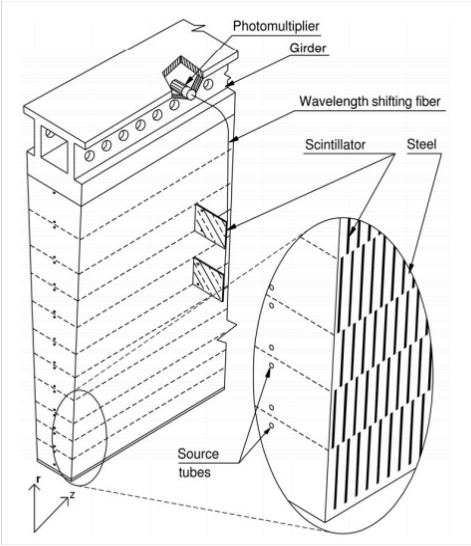

Figure 4.15: A wedge of the TileCal contains steel and scintillating tile components which are oriented parallel to incoming particles at $\eta = 0$. A wavelength-shifting fiber guides the scintillation light to PMTs [78].

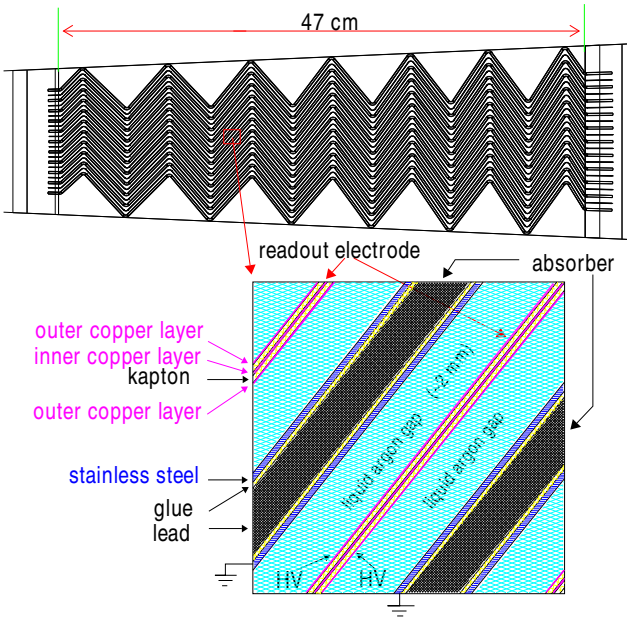

Figure 4.16: A slice of the EM barrel showing its accordion structure. Layers of lead absorber are sandwiched between layers of LAr [77].

The rest of the calorimeter system, which includes the presampler, the EM calorimeter, sections of the hadronic calorimeter, and the forward calorimeter, are LAr-based. A LAr and lead-based system serves as the EM calorimeter in the barrel and endcap, covering up to $|\eta| = 3.2$. Lead plates are arranged in an accordion geometry filled with LAr as the active material. The accordion shape and detailed structure of a barrel slice are shown in Figure 4.16. Particles traversing the detector will ionize the LAr and induce a signal on copper electrodes. The barrel calorimeter is divided into three layers, while the endcap calorimeter is divided into two or three layers depending on the region. The EM calorimeter ranges from 24 to 27 radiation lengths (X_0) in depth [77, 79].

The EM calorimeter has finer segmentation than the hadronic calorimeter in the transverse plane

so that individual photon showers from neutral pion decays can be resolved. The granularity ranges from $\Delta\eta \times \Delta\phi = (0.025/8 - 0.1) \times (\pi/128 - \pi/32)$. A table summarizing the granularity for each EM, hadronic, and forward calorimeter module can be found in [79].

A LAr and copper-based hadronic endcap calorimeter spans the region from $1.5 < |\eta| < 3.2$ and has a parallel plate structure. LAr also serves as the active material for the forward calorimeter [77].

4.6 Muon Spectrometer

Muons produced in LHC collisions often interact minimally with the detector material and therefore will travel through the inner detector and calorimeter system without losing significant energy. ATLAS has a spectrometer composed of four detector technologies dedicated to measuring muons: MDT, Cathode Strip Chamber (CSC), Resistive Plate Chamber (RPC), and Thin Gap Chamber (TGC).

Similar to the other detectors, the MS is divided into the barrel ($|\eta| < 1.05$) and the endcap ($1.05 < \eta < 2.7$). The endcap detector is composed of three wheels on each side which cap the cylindrical detector: one small wheel and two large wheels. The CSC and TGC technologies can be found in the endcap, while the RPC technology covers the barrel. The MDTs are located in both the barrel and endcap regions. The layout of the detector technologies is shown in Figure 4.17.

The MDTs are the primary precision tracking technology in the barrel and cover most of the end-cap except for a small section of the small wheel from $2.0 < |\eta| < 2.7$, where the CSCs are used due to their improved ability to handle high particle rates [80]. Each MDT is a drift tube composed

of a ∼meter-long aluminum tube with a 3 cm diameter surrounding a 50 micron-thick gold-plated tungsten-rhenium wire. A voltage of ∼3 kV, applied to the wire, creates a strong electric field [81]. Each tube is filled with 93% argon gas and 7% CO_2 and is positioned to precisely measure η.

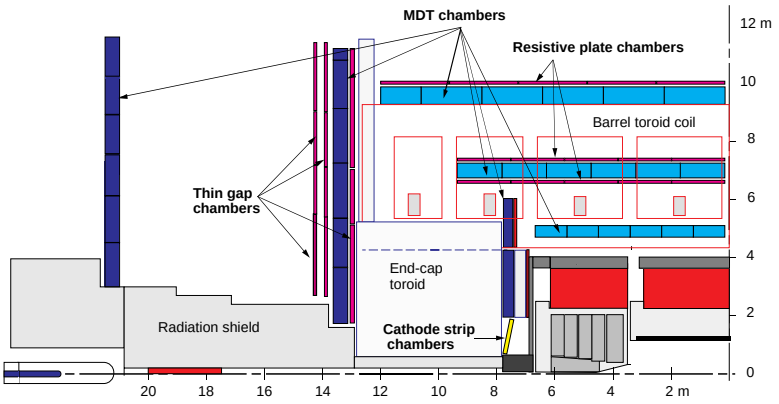

Figure 4.17: The layout of the Muon Spectrometer in a cutout of the y-z plane [82].

The MDT tubes, similar to the TRT straws, are operated as drift chambers with a maximum drift time of $\approx$ 750 ns [81]. As ionized electrons drift towards the wire where the electric field is stronger, an avalanche process begins to multiply the primary charge and amplify the signal, which ultimately results in a similar gas gain to the TRT of $\sim 10^4$ [80].

The CSCs are Multiwire Proportional Chamber (MWPC) detectors which can track higher rates of particles than the MDTs without significant efficiency losses. As a result they are placed in the highest η region of the innermost endcap wheel, where the particle rate is the largest. Each chamber has readout strips covering both sides to provide precision measurements of η and ϕ [80].

The TGC and RPC technologies are used in the ATLAS trigger system due to their superior time resolution. The TGC and RPC technologies have intrinsic detector-only time resolution of 4

and 1.5 ns, respectively [67]. The TGCs are MWPCs operated in saturated mode. Each individual chamber is 2.8 mm thick with an operating voltage of ≈ 3 kV and filled with 55% CO_2 and 45 % n-pentane [80]. The RPCs are parallel-plate detectors operated in avalanche mode, with plates made of Bakelite and a gas gap of 2 mm. They are filled with a gas mixure of $C_2H_2F_4$, iso-C_4H_{10}, and SF_6 [83]. Both triggering chambers provide a measurement of the non-precision coordinate ϕ [67].

Further details can be found in [80].

5

Trigger and Object Reconstruction

After the protons have collided, there are a number of steps before the collision data can be analyzed. Limited information about the collision event, at trigger level, is used to decide whether or not the event is interesting enough to be recorded to disk. After the event is recorded to disk, the raw data has to be processed in a step called *reconstruction* which constructs physically meaningful objects and quantities from the detector output. The following sections briefly outline triggering and recon-

struction.

5.1 The ATLAS Trigger

The LHC collides proton bunches every 25 ns, or at a rate of 40 MHz. To filter these collisions for interesting events, ATLAS employs a two-stage trigger system to reduce the recorded data rate from 40 MHz to approximately 1 kHz.

The first stage is called the Level-1 (L1) Trigger. This is a hardware-based filter which makes decisions based on information from the MS and calorimeters with coarse granularity, and reduces the data rate from 40 MHz to 100 kHz. Events which pass the L1 Trigger are then passed to the software-based High Level Trigger (HLT). At the HLT, software-based objects using finer granularity information are available to make a more refined decision about whether or not an event is interesting. Events which pass both levels at a rate of 1 kHz are then recorded to disk. More information on the ATLAS trigger system can be found in [84, 85].

There are numerous triggers based on various physics quantities. This thesis uses events which pass the Missing Transverse Energy, or $E_{\mathrm{T}}^{\mathrm{miss}}$ trigger. The motivation and effect of this choice is discussed in Chapter 7.

5.1.1 $E_{\mathrm{T}}^{\mathrm{miss}}$ Trigger

The initial transverse momentum of the colliding protons is approximately zero. Due to momentum conservation, any non-zero value of $E_{\mathrm{T}}^{\mathrm{miss}}$ is due to either detector mismeasurement or from particles which are invisible to the detector. The $E_{\mathrm{T}}^{\mathrm{miss}}$ trigger calculates this value using calorimeter

measurements.

Trigger-level $E_{\mathrm{T}}^{\mathrm{miss}}$ is defined as $E_{\mathrm{T}}^{\mathrm{miss}} = \sqrt{(E_x^{\mathrm{miss}})^2 + (E_y^{\mathrm{miss}})^2}$, with

$$\begin{aligned} E_x^{\mathrm{miss}} &= -\Sigma_i E_i \sin\theta_i \cos\phi_i \\ E_y^{\mathrm{miss}} &= -\Sigma_i E_i \sin\theta_i \sin\phi_i, \end{aligned} \tag{5.1}$$

where i runs over objects that vary depending on the specific trigger algorithm and level [86]. At L1, the sum is calculated over the collection of jet elements. A jet element is a trigger tower with a typical granularity of $\Delta\eta \times \Delta\phi = 0.2 \times 0.2$. Each trigger tower consists of smaller towers (typically 0.1×0.1) of calorimeter cells. Each 0.1×0.1 tower is required to pass an η-dependent energy threshold to be included in the calculation. This threshold filters out noise from pile-up and is set such that the tower has an average occupancy of ∼1%. The L1 $E_{\mathrm{T}}^{\mathrm{miss}}$ trigger contributes ∼5-10 kHz to the total L1 trigger rate [86].

At the second level, the HLT, several $E_{\mathrm{T}}^{\mathrm{miss}}$ algorithms and thresholds were implemented over the course of Run-2 data taking. Three algorithms will be briefly discussed here: the `cell`, `mht`, and `pufit` algorithms. The trigger defined for each data taking period is shown in Table 5.1. Further details can be found in [86].

The simplest algorithm (`cell`) calculates $E_{\mathrm{T}}^{\mathrm{miss}}$ as a sum over all calorimeter cells. Cells with the absolute value of the signal-to-noise ratio ($|E_i/\sigma_{E_i}|$) < 2 are excluded. Cells with $E_i/\sigma_{E_i} < -5$ are also excluded.

A more refined algorithm (`mht`) calculates $E_{\mathrm{T}}^{\mathrm{miss}}$ using jet objects. Offline jet reconstruction is summarized in 5.5; the HLT reconstructs jets from topo-clusters, or clusters of energy deposits, in a

Data Period	Approx. Lumi [fb^{-1}]	Trigger
2015	3.9	HLT_xe70_mht
2016 A-D3	7.0	HLT_xe90_mht_L1XE50
2016 D4-F1	6.1	HLT_xe100_mht_L1XE50
2016 F2-L	22.6	HLT_xe110_mht_L1XE50
2017 B-D5	13.8	HLT_xe110_pufit_L1XE55
2017 D6-N	33.4	HLT_xe110_pufit_L1XE50
2018 B-C5	6.8	HLT_xe110_pufit_xe70_L1XE50
2018 C5-R	54.0	HLT_xe110_pufit_xe65_L1XE50

Table 5.1: Trigger used for each data-taking period in Run-2.[†]

similar manner. The topo-clustering algorithm is detailed in 5.5.

Due to the large increase in the number of proton-proton collisions per event (pile-up) over the course of Run-2, a new algorithm (`pufit`) was implemented to correct for the contribution of pile-up collisions to the calorimeter energy measurements. The algorithm does a fit to topo-clusters to estimate the contribution. Full details can be found in [86].

The efficiency of the $E_{\mathrm{T}}^{\mathrm{miss}}$ trigger can be measured in data enriched in $Z \to \mu\mu$ events. Because muon information is ignored in the trigger-level calculation of $E_{\mathrm{T}}^{\mathrm{miss}}$, the trigger efficiency as a function of the p_{T} of the Z-boson is a good measure of the $E_{\mathrm{T}}^{\mathrm{miss}}$ trigger performance. Figure 5.1 shows that $> \sim$90% of $Z \to \mu\mu$ events where the Z has $p_{\mathrm{T}} > 170$ GeVwill pass the $E_{\mathrm{T}}^{\mathrm{miss}}$ trigger.

5.2 Inner Detector track reconstruction

5.2.1 Reconstruction procedure

The most important reconstructed objects in this thesis work are ID tracks, which represent the trajectories of particles traversing the Inner Detector. ID tracks include hits from the pixel detector,

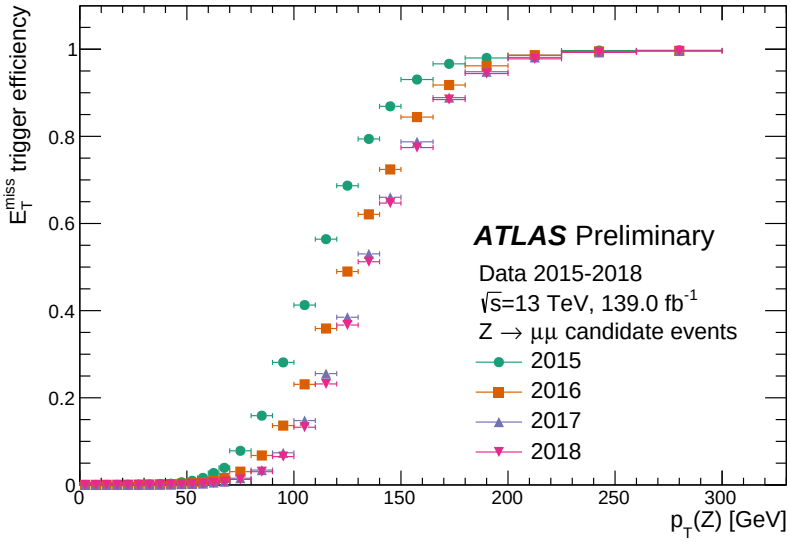

Figure 5.1: The efficiency of the $E_{\mathrm{T}}^{\mathrm{miss}}$ trigger is measured in $Z \rightarrow \mu\mu$ events as a function of the p_{T} of the reconstructed Z-boson. The efficiency is greater than ∼90% for p_{T} > 170 GeV with the lowest unprescaled $E_{\mathrm{T}}^{\mathrm{miss}}$ triggers [86].

the Semiconductor Tracker (SCT), and the Transition Radiation Tracker (TRT).

Pixels and strips which record a hit are clustered per layer using a connected component analysis method [87]. This method groups pixels and strips which have neighboring corners and edges. ID tracks are formed using either an *inside-out* or an *outside-in* algorithm which combine the pixel and strip clusters with the TRT hits [88].

Due to the high particle density in the pixel detector, an algorithm to identify clusters which likely came from multiple particles is run on the pixel clusters. This is further discussed in Section 5.2.1).

Inside-out reconstruction The inside-out algorithm starts by forming track segments out of silicon hits and then extending these segments to the TRT to form track candidates.

To begin, each cluster on a pixel detector layer (which provides three-dimensional information) and pairs of clusters on the SCT detector layers (one from each set of offset readout strips) form *space-points*. Three silicon space-points form a *track seed* and define a road where associated hits from other layers can be added. A combinatorial Kalman filter is employed to build track candidates out of the seeds and associated hits [88–90].

This procedure results in multiple track candidates sharing the same clusters as well as track candidates with misassigned space points. To resolve situations with shared clusters, a second stage of filtering is applied by passing the track candidates to the *ambiguity solver*. The order in which tracks are passed is determined by the *track score* which depends on the number of holes (absences of hits on a layer), the track fit (χ^2), momentum, and the cluster measurement quality (for example, tracks

with more pixel hits are weighted to have a better score due to the pixel detector resolution) [88, 89]. For each track candidate, the ambiguity solver then counts the clusters shared by that candidate and any previously accepted track candidate. If that number exceeds one for that candidate or any previously accepted track, then the offending cluster is removed from the track candidate and the track is rescored. Note that this does not include removing clusters properly identified as merged by the neural network. Additionally clusters can be shared by no more than two tracks [89].

Finally, the track candidate is accepted if it passes the following requirements (for `Loose` tracks):

- $p_T > 500$ MeV
- $|\eta| < 2.5$
- At least seven silicon (pixel + SCT) hits including any expected in disabled sensors
- At most one shared silicon module (equivalent to one hit in the pixel or two hits in the SCT layers)
- At most two holes in the silicon layers (pixel + SCT)
- At most one hole in the pixel layers

The accepted tracks are passed to the TRT track extension step. The silicon track segments are extrapolated into the TRT, where compatible TRT hits are added to the track. Details of the TRT extension can be found in Reference [88].

Outside-in reconstruction The inside-out algorithm can fail for a number of reasons. For example, tracks which originate from a secondary vertex (and therefore have a low number of silicon hits) may be missed. To catch these tracks, an outside-in algorithm starting with the TRT hits is run on hits which are already assigned to a track.

TRT hits do not provide a measurement on the coordinate parallel to the detector straw axis. Therefore, hits are projected onto the r - ϕ (r - z) plane in the TRT barrel (endcap) region. TRT segments are then identified using a Hough transform [91]. These segments are then extrapolated to the silicon detector so that silicon hits missed by the inside-out algorithm can be added to improve the measurement [88, 92].

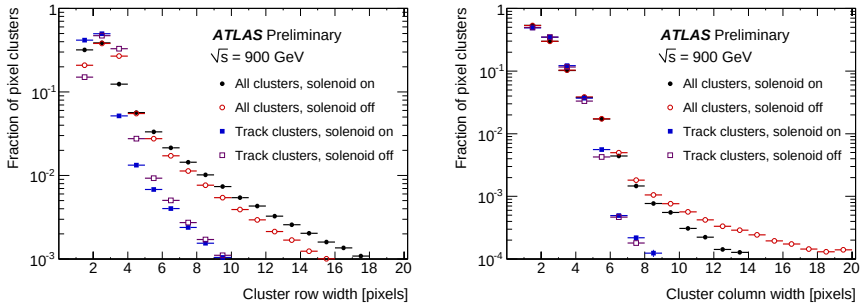

(a) Cluster row width **(b)** Cluster column width

Figure 5.2: The distribution of pixel cluster width for on-track cluster and all clusters along the (a) $r - \phi$ direction and (b) r, z directions using collision data at $\sqrt{s}$= 900 GeV. The large difference in the tail distributions with and without the solenoid is likely due to low-momentum particles which are deflected in the solenoidal field [93]

IDENTIFYING MERGED CLUSTERS The pixel cluster size in the $r - \phi$ and r, z directions is shown in Figure 5.2. There are a significant fraction of clusters which contain more than one pixel. There are several ways that energy can be deposited in multiple pixels. The simplest case is if an incident particle has a large angle of incidence that crosses multiple pixels. The incident particle can also emit δ-rays while traversing the silicon. These δ-rays, which are energetic electrons kicked out of the material, can deposit energy in a neighboring pixel. The drift electrons and holes also feel a non-negligible Lorentz force from the magnetic field. The angle that the electrons and holes drift with respect to

the electric field direction due to the force of the magnetic field called the *Lorentz angle*. This can result in induced charged across multiple pixels. Finally, due to the high particle multiplicity environment, there is a significant rate of particles with overlapping tracks [94].

To identify which clusters originate from multiple particles, the clusters are fed through multiple neural networks. The pixel charge measurements, the pixel sizes, the layer specifications, the estimated angles of incidence ϕ and θ, and the pixel η (if there exists no track candidate) are inputs into the neural networks. One neural network calculates the probability that a cluster originated from either 1, 2, or 3 particles (P_1,P_2,P_3). These probabilities are then used to classify each cluster according to the requirements in Table 5.2.

Categorization	Requirement
1 particle	$P_2 < 0.6$, $P_3 < 0.2$
2 particles	$P_2 > 0.6$, $P_3 < 0.2$
3 particles	$P_3 > 0.2$

Table 5.2: Requirements on the output probabilities from the neural network to identify a given cluster as originating from more than one particle. Values taken from [95].

The performance in simulated dijet events of the classification neural net is shown in Figure 5.3. These requirements result in $\sim$ 95% of 1-particle clusters being classified correctly, while $\sim$ 80% of 2-particle clusters and $\sim$ 95% of 3-particle clusters are classified as originating from more than one particle [95].

A second group of neural networks then estimates where the particles crossed the pixel layer and the corresponding uncertainties on this estimate. The performance in a sample of simulated dijet events is shown in Figure 5.4.

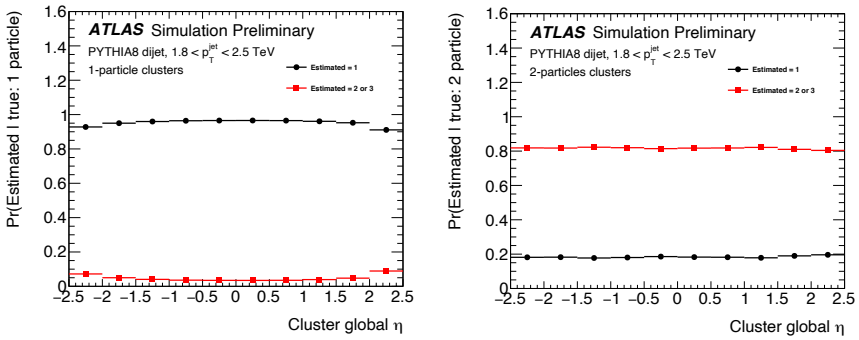

(a) 1-particle cluster

(b) 2-particle clusters

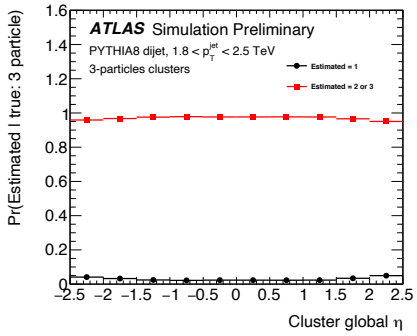

(c) 3-particle clusters

Figure 5.3: The performance of the neural network used to classify clusters is measured in a sample of simulated dijet events. The probabilities across cluster η for (a) 1-particle clusters, (b) 2-particle clusters, and (c) 3-particle clusters to be classified as either 1 or multiple clusters are shown. [95]

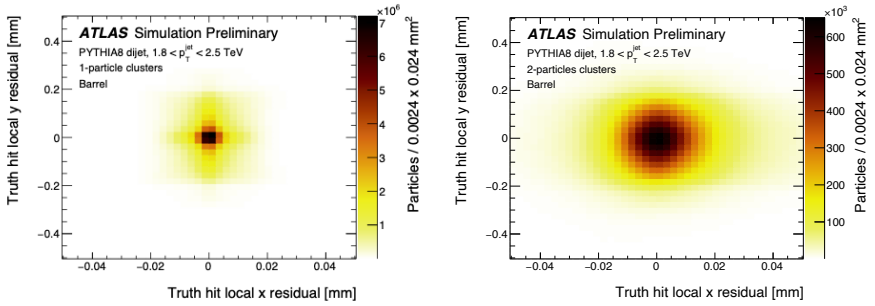

(a) 1-particle cluster

(b) 2-particle clusters

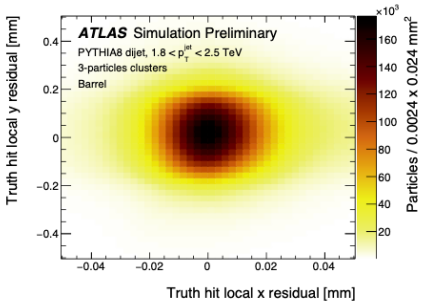

(c) 3-particle clusters

Figure 5.4: The performance of the position estimation neural networks is measured in a sample of simulated dijet events for clusters in the pixel barrel. The x (corresponding to $r - \phi$) and y (corresponding to z) residuals for (a) 1-particle clusters, (b) 2-particle clusters, and (c) 3-particle clusters are shown. [95]

Further details of the neural network training and performance are found in Reference [94, 95].

Reconstruction performance The efficiency of reconstructing ID tracks is shown in Figure 5.5 in simulated minimum bias events. Multiple definitions of tracks are used by ATLAS; `Loose` tracks, which are used in this thesis, are defined by the requirements in Section 5.2.1. *. The efficiency of reconstructing `Loose` tracks with $p_{\mathrm{T}} > 5$ GeVat $\eta = 0$ is around 90% [96].

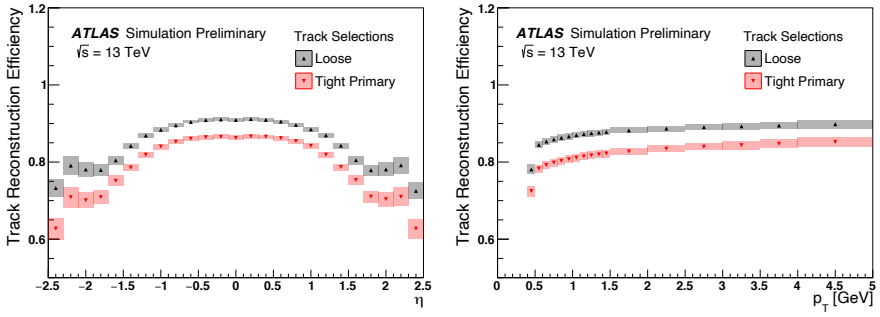

(a) Efficiency vs. η **(b)** Efficiency vs. p_{T}

Figure 5.5: The efficiency as a function of (a) η and (b) p_{T} for reconstructing ID tracks. Two working point definitions are shown, `Loose` and `Tight Primary`. The `Loose` definition is used to build the tracks which are described in later chapters of this thesis [96].

As previously mentioned, tracking is done in a high particle multiplicity environment. As a result, another important benchmark of the tracking performance is the number of reconstructed fake tracks. Figure 5.6 shows the dependence of the number of tracks reconstructed on the number of pile-up interactions, μ. Because the number of tracks originating from real particles should have a linear dependence on the number of pile-up interactions, any non-linear dependence can be attributed to fake tracks. Tracks which satisfy the `Loose` working point are shown to have around a

*The `Loose` definition used in Figure 5.5 has a p_{T} cut of 400 MeV. This is loosened with respect to the definition in Section 5.2.1.

5% fake rate for $\mu = 30$ [96].

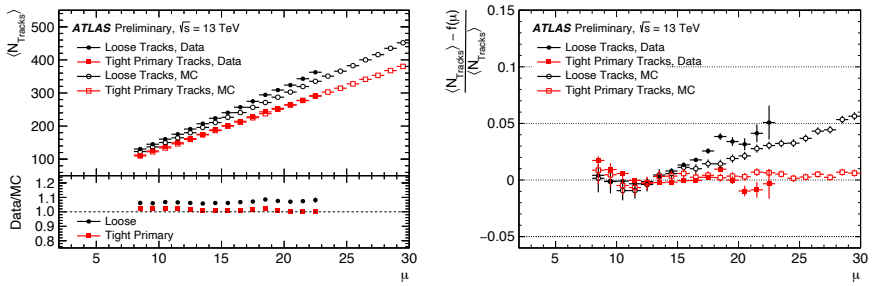

(a) $< N_{\text{track}} >$ vs μ **(b)** Fake rate vs μ

Figure 5.6: (a) shows the average number of ID tracks reconstructed versus the number of pile-up interactions. (b) shows an estimation of the number of fake tracks versus the number of pile-up interactions. This estimation assumes that $f(\mu)$, or the predicted rate of real tracks, can be estimated from a linear fit to the rate of tracks at low μ [96].

5.3 Primary Vertex reconstruction

To reconstruct the set of all candidate vertices in the event, an adaptive vertex fitter algorithm [97] is run over ID tracks which pass a series of requirements specified in [98]. The fit is seeded by the transverse position of the beam spot and is run multiple times, minimizing the χ^2 of the tracks. Tracks are assigned weights depending on their compatibility with originating from the vertex. After the final vertex position is determined, any incompatible tracks are re-used to reconstruct other vertices. Further details of this algorithm are found in [98].

The primary vertex, which represents the point of collision, is the vertex reconstructed with the highest $\Sigma_i \, p_{\text{T}}^2$, where i runs through all tracks associated to the vertex.

5.4 Muon reconstruction

To reconstruct muons, hits in each layer of the MS are combined to form *segments*. MS tracks are required to contain at least two segments (except in the barrel-endcap transition area where the requirement is loosened due to fewer detector layers). A global fit of the MS hits is performed and the resulting χ^2 of the fit is used in the muon identification criteria.

Muons are built from MS segments which pass these requirements. Various criteria used to define what constitutes a muon are described in [99] and used in ATLAS reconstruction. This thesis uses two definitions, *combined* muons which incorporate ID measurements, and *extrapolated* muons.

Combined (CB) muons are formed from the combination of ID and MS tracks. MS tracks are extrapolated to the inner detector, where they are matched with an ID track to form a CB muon. An alternative algorithm which takes ID tracks and extrapolates them to the MS, is also used for a small fraction of CB muons and largely reconstructs low p_{T} muons missed by the nominal algorithm [84, 99].

A different definition of muons is useful for $|\eta| > 2.5$, where there is a lack of coverage by the ID. Extrapolated (ME) muons, used for large η values, are built from MS tracks consisting of at least three segments that point back to the interaction point.

This thesis uses *medium* muons, which consist of CB muons in the $|\eta| < 2.5$ region and ME muons in the $2.7 > \eta > 2.5$ region. Note that the signal region described in Chapter 7 is restricted to $|\eta| < 1.8$; therefore ME muons are only used as an input to the $E_{\mathrm{T}}^{\mathrm{miss}}$ calculation described later in

Section 5.7. Under the medium definition, CB muons are additionally required to have

- if $|\eta| > 0.1$, ≥ 3 hits in ≥ 2 MDT layers,
- if $|\eta| < 0.1$, ≥ 3 hits in ≥ 1 MDT layer and < 1 MDT hole layer,
- q/p significance < 7.

q/p significance refers to the absolute value of the difference of the q/p measurement using the MS and ID, divided by the uncertainty on the combined measurement.

The efficiency of reconstructing medium muons as a function of η in $Z \rightarrow \mu\mu$ events is shown in Figure 5.7. The efficiency is greater than 95% for $\eta < 2.5$ except for a dip at $|\eta| < 0.1$ due to a gap in the detector where the cables run.

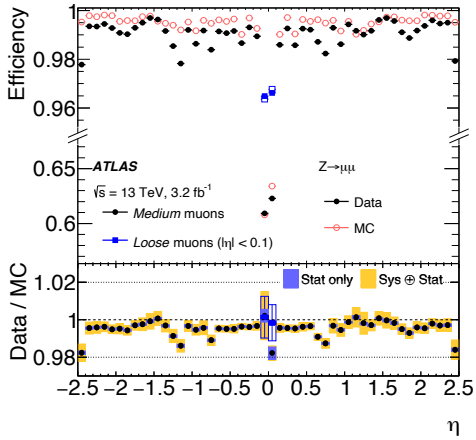

Figure 5.7: The efficiency of muon reconstruction versus η for medium and loose muons with $p_T > 10$ GeV. The efficiency is measured using $Z \rightarrow \mu\mu$ events, where there is a noticeable dip at $|\eta| < 0.1$ due to lack of detector coverage [99].

Further details of the reconstruction algorithms and performance are found in [99], In this thesis, reconstructed muons are used both in the E_T^{miss} calculation and to categorize ID tracks.

5.5 Jet reconstruction

Although this thesis describes a search for highly ionizing tracks, reconstructed jets which are close to candidate tracks are used to tag tracks which come from Standard Model processes. The criteria for vetoing tracks which likely originate from electrons or hadrons is further described in Chapter 7.

A jet is a cluster of calorimeter energy deposits from significant hadronic or electromagnetic activity. The jets used in this thesis are collections of *topo-clusters*, which are clusters of calorimeter cells. These cells are grouped using an algorithm that clusters neighboring cells based on the absolute value of the cell signal-to-noise ratio, where the noise is defined as the average cell noise [79].

The cells which seed each topo-cluster are required to have large signal-to-noise ratios (≥ 4). Any cells neighboring the seeds are included in the cluster. If the newly added cell has a signal-to-noise ratio above 2, then its own neighbors are also added to the cluster. More details of the algorithm are found in [79].

The topo-clusters are then combined into jet objects using an anti-k_T algorithm [100] with ΔR = 0.4 [79]. The energy resolution of these jets measured in 2017 data, after a series of calibrations and corrections are applied, is shown in Figure 5.8. For jets with $p_{\mathrm{T}} > 100$ GeV, the energy resolution is $<\sim$10% [101].

To decrease the contamination of pileup jets, a variable called the Jet-Vertex-Tagger (JVT) is calculated and used to identify jets which likely originated from pile-up. This likelihood-based variable depends on the p_{T} of any associated tracks originating from the primary vertex, the jet p_{T}, and the number of pile-up tracks in the event. More details on the specific calculation can be found in [102].

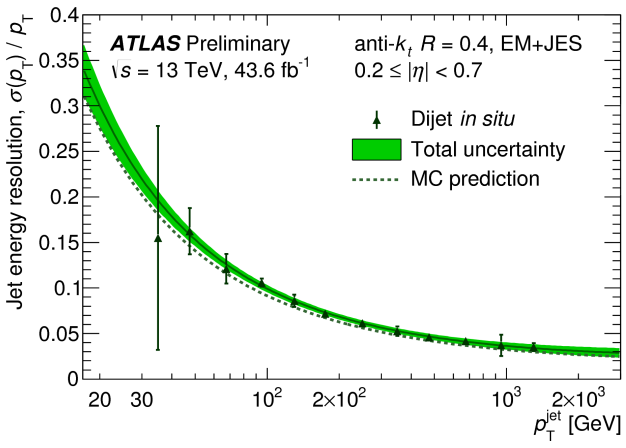

Figure 5.8: The resolution of the jet energy measurement as a function of jet p_{T} in 2017 data. The prediction in simulation is given by the dashed line and the measurement in data is given by the solid line surrounded by the green uncertainty band. The resolution measured in data uses an in-situ method in dijet events [101].

5.6 Other objects

In this thesis, electrons are only used as an input to the $E_{\mathrm{T}}^{\mathrm{miss}}$ calculation described in 5.7. Electrons are reconstructed from ID hits and EM calorimeter deposits. Details can be found in [103].

ATLAS also has standard reconstruction algorithms for tau leptons [104] and photons [105], but they are not used in this thesis. Note that photon-like signatures are included in the $E_{\mathrm{T}}^{\mathrm{miss}}$ calculation through the jet collection, but ATLAS photon objects are not used.

5.7 $E_{\mathrm{T}}^{\mathrm{miss}}$ reconstruction

After the physics objects are reconstructed, the Missing Transverse Energy, or $E_{\mathrm{T}}^{\mathrm{miss}}$, is calculated from the objects. Offline $E_{\mathrm{T}}^{\mathrm{miss}}$ (i.e. not trigger-level) is defined as the negative vectorial sum of the p_{T} of the following collections:

$$E_{\mathrm{T}}^{\mathrm{miss}} = -\Sigma p_T^e - \Sigma p_T^\mu - \Sigma p_T^{\mathrm{jet}} - \Sigma p_T^{\mathrm{track}}. \tag{5.2}$$

The first term Σp_T^e is the vectorial sum over the electron p_{T} measurements, where electrons which pass the `LooseAndBLayer` requirements defined in [103] with $|\eta| < 2.47$ and $p_{\mathrm{T}} > 10$ GeV are considered. Medium quality muons with $|\eta| < 2.7$ and $p_{\mathrm{T}} > 10$ GeV are considered in Σp_T^μ. Jets which enter the $\Sigma p_T^{\mathrm{jet}}$ term are required to have $p_{\mathrm{T}} > 20$ GeVand $|\eta| < 2.8$, as well as a JVT requirement of 0.59. The JVT and p_{T} thresholds help reduce the contribution of pile-up jets [106]. Finally, unused ID tracks which are not compatible with originating from an electron, muon, or jet are used in the $\Sigma p_T^{\mathrm{track}}$ term, also called the track soft term [107]. Note that tracks with $p_{\mathrm{T}} > 30$ GeV are required to pass a set of isolation and track momentum uncertainty criteria to be included in the track-based soft term. An overlap removal procedure is applied to ensure there is no double-counting of objects (for example, the electron collection will have some overlap with the jet collection).

The $E_{\mathrm{T}}^{\mathrm{miss}}$ resolution using the $E_{\mathrm{T}}^{\mathrm{miss}}$ definition in [107] (which differs from the $E_{\mathrm{T}}^{\mathrm{miss}}$ definition in this thesis due to the inclusion of reconstructed photons and tau leptons) is shown in Figure 5.9. The RMS of the combined $E_{\mathrm{x}}^{\mathrm{miss}}$ and $E_{\mathrm{y}}^{\mathrm{miss}}$ distributions is around 25 GeVfor $E_{\mathrm{T}}^{\mathrm{miss}} = 500$ GeV.

More details on the performance of the $E_{\mathrm{T}}^{\mathrm{miss}}$ reconstruction and the overlap removal procedure can be found in [107]. The $E_{\mathrm{T}}^{\mathrm{miss}}$ distribution in data, as well as the expected distribution from signal, is further discussed in 7.

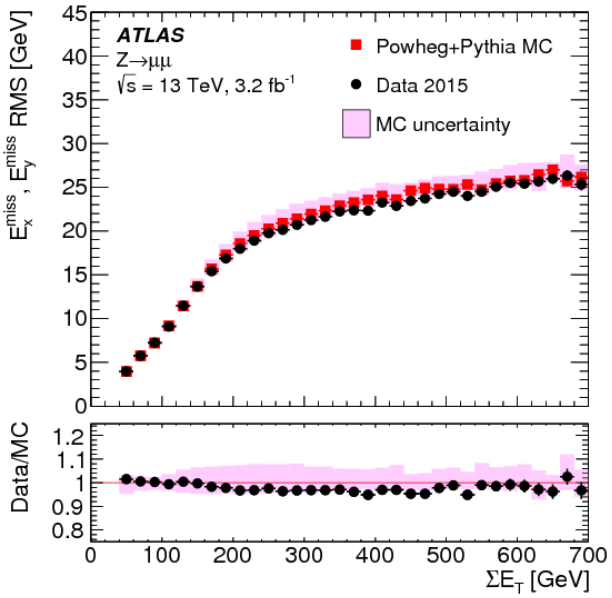

Figure 5.9: The RMS resolutions of $E_{\mathrm{x}}^{\mathrm{miss}}$ and $E_{\mathrm{y}}^{\mathrm{miss}}$ predicted in simulation and measured in $Z \rightarrow \mu\mu$ events in 2015 data [107].

6

Measurement of $\mathrm{d}E/\mathrm{d}x$

This thesis, which later describes a search for highly ionizing particles beginning in Chapter 7, requires a specialized treatment of pixel $\mathrm{d}E/\mathrm{d}x$ information. The calculation and calibration of the $\mathrm{d}E/\mathrm{d}x$ measurement is described in this chapter.

6.1 Pixel detector measurement

The analysis uses the $\mathrm{d}E/\mathrm{d}x$ measurements provided by the pixel detector. The pixel detector, described in Chapter 4, consists of four layers. There can be more than one measurement per layer if the particle passes through regions of the detector where sensors overlap in ϕ (see Figure 6.1).

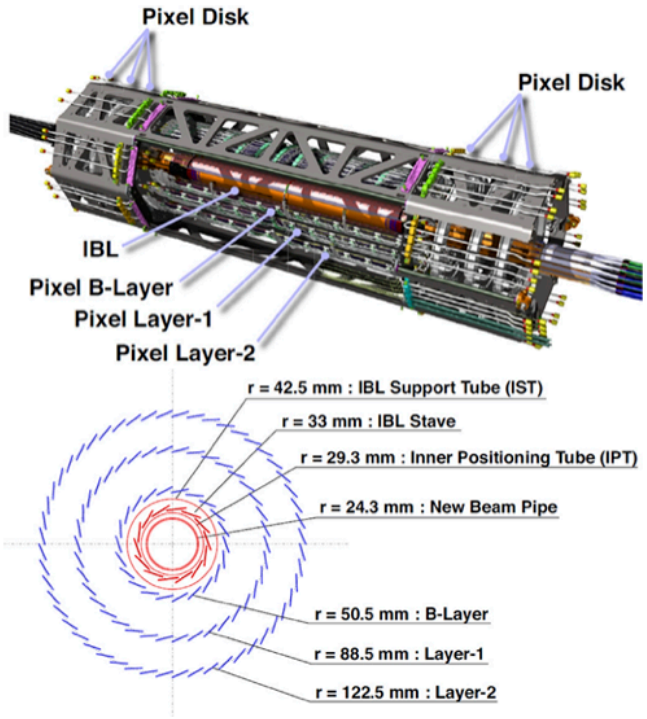

Figure 6.1: A drawing of the ATLAS pixel detector and a projection onto the $r - \phi$ plane are shown. The staves on each layer overlap in ϕ [108].

A particle traversing a layer often deposits charge in more than one pixel. Neighboring pixels are clustered according to the details found in Chapter 5. For each cluster, we define the cluster charge Q as the sum of the individual calibrated pixel charges [71].

A set of quality cuts is applied to these clusters. If the cluster position is in the edge region of a module or in the region where two pixel sensors are connected to a single electronics channel, it is removed. The remaining clusters form the set of "good clusters" [71].

6.2 Truncated mean algorithm

For each cluster, the cluster charge is converted to a cluster $\mathrm{d}E/\mathrm{d}x$ measurement using the equation

$$\mathrm{d}E/\mathrm{d}x = \frac{Q\,W}{\rho\,x\,e}, \tag{6.1}$$

where W is the average energy required to ionize an electron-hole pair, e is the elementary charge, ρ is the density of silicon, and x is the particle path length through silicon [71]. We then combine the cluster $\mathrm{d}E/\mathrm{d}x$ measurements into a single track $\mathrm{d}E/\mathrm{d}x$ measurement using an algorithm commonly referred to as the truncated mean algorithm. This algorithm was traditionally used in wire chambers which had on average tens of measurements per track [109]. The truncated mean algorithm reduces the impact of the long Landau tail on the $\mathrm{d}E/\mathrm{d}x$ measurement and is designed to estimate the Most Probable Value (MPV) of the $\mathrm{d}E/\mathrm{d}x$ distribution.

The algorithm flows as follows:

1. Order the n good cluster measurements in increasing $\mathrm{d}E/\mathrm{d}x$ for a given track.
2. Remove the largest m cluster $\mathrm{d}E/\mathrm{d}x$ values.
3. Average the remaining $n - m$ cluster $\mathrm{d}E/\mathrm{d}x$ values.
4. Calculate the track $\mathrm{d}E/\mathrm{d}x$ from the averaged $\mathrm{d}E/\mathrm{d}x$.

n	m	Removed clusters	IBL overflow?	Conditions
$2-4$	1	Δ^n	No	
$5+$	2	Δ^n, Δ^{n-1}	No	
2	1	$\Delta_{\text{IBL OF}}$	Yes	
$3,4$	1	$\Delta_{\text{IBL OF}}$	Yes	$Q^{\text{max}}_{\text{non-IBL}} < Q_{\text{IBL OF}}$
$3,4$	2	$\Delta^{\text{max}}_{\text{non-IBL}}, \Delta_{\text{IBL OF}}$	Yes	$Q^{\text{max}}_{\text{non-IBL}} > Q_{\text{IBL OF}}$
$5+$	2	$\Delta^{\text{max}}_{\text{non-IBL}}, \Delta_{\text{IBL OF}}$	Yes	

Table 6.1: The $\mathrm{d}E/\mathrm{d}x$ truncated mean algorithm parameters. The table shows the number of clusters m removed given n used hits. $Q_{\text{IBL OF}}$ refers to the maximum charge measurable in the IBL front-end. Due to the fact that the IBL provides no numerical measurement for hits which set the overflow bit high, tracks with a hit in the IBL OF are treated separately in the algorithm.

Table 6.1 shows the value of m, which depends on n for a given track. Note that there is a special treatment of tracks with a hit in the Insertable B-Layer Overflow (IBL OF), since the IBL front-end electronics provides no numerical measurement for these hits. Tracks with a hit in the IBL OF are referred to as `IBL1` tracks, and tracks without a hit in the IBL OF are referred to as `IBL0` tracks. As discussed in Chapter 4, the IBL has different front-end electronics with respect to the other pixel layers. The ToT value is measured with 4 bits; if the ToT exceeds the maximum value measurable, a bit referred to as the overflow bit is set high.

In the table, Δ refers to the $\mathrm{d}E/\mathrm{d}x$ measurement of a given cluster, ordered in increasing value from $\Delta^0, \Delta^1, \Delta^2, ...\Delta^n$. Let $Q_{\text{IBL OF}}$ refer to the maximum charge for which the IBL electronics provide a numerical measurement. In the case where one of the track clusters had a hit exceeding this charge, that cluster is always removed, and a subset of the non-IBL hits ($\Delta^0_{\text{non-IBL}}, ...\Delta^{\text{max}}_{\text{non-IBL}}$) are also removed.

For example:

- If a track has m = 4, or four good clusters, with no hits in the IBL OF, the highest $\mathrm{d}E/\mathrm{d}x$

cluster is removed from the $\mathrm{d}E/\mathrm{d}x$ calculation and the other three cluster $\mathrm{d}E/\mathrm{d}x$ values are averaged.

- If the track instead has a hit in the IBL OF, then that hit is removed if the other three cluster charges are less than $Q_{\text{IBL OF}}$.
- If the track has a hit in the IBL OF and the maximum cluster charge from a non-IBL layer is larger than $Q_{\text{IBL OF}}$, then the largest non-IBL cluster is removed along with the IBL OF cluster.

The dependence of the track $\mathrm{d}E/\mathrm{d}x$ resolution on the number of hits used in the truncated mean is shown in 6.2. The width of the distribution decreases with an increased number of averaged hits.

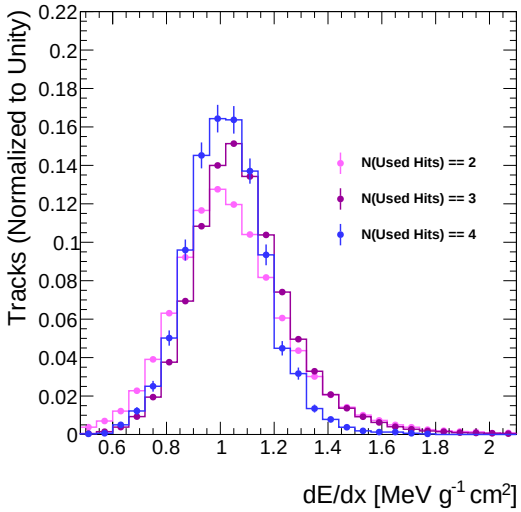

Figure 6.2: The track $\mathrm{d}E/\mathrm{d}x$ distribution (after applying the corrections described in Section 6.3), as a function of the number of hits averaged in the calculation. The tracks shown are from a subset of data collected in 2018 which pass the $\mathrm{d}E/\mathrm{d}x$ control region event selection (see Chapter 8). The distribution narrows with an increase in the number of averaged hits.

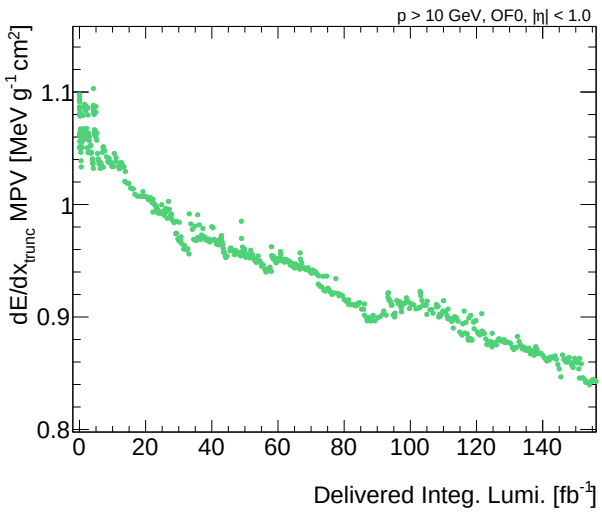

Figure 6.3: The most probable value of track $\mathrm{d}E/\mathrm{d}x$ measured in the pixel detector as a function of delivered integrated luminosity for the Run-2 dataset (2015–2018), for tracks with momentum > 10 GeV, $|\eta|$ < 1, and no hits in the IBL OF. Each point represents an individual run.

6.3 Corrections

The cluster charge and consequently the track $\mathrm{d}E/\mathrm{d}x$ measurements are very sensitive to detector conditions. For instance, due to radiation damage, the $\mathrm{d}E/\mathrm{d}x$ measurement in the Run-2 dataset decreased appreciably as a function of delivered integrated luminosity (see Figure 6.3). The $\mathrm{d}E/\mathrm{d}x$ measurement was also seen to be affected by detector conditions including the high voltage applied to the sensors and the front-end electronics settings (see Figure 6.4).

As discussed in greater detail in Chapter 2, the measured track $\mathrm{d}E/\mathrm{d}x$ is dependent on the track path length x through the sensor material for thin sensors. For a track originating from the interaction point, the angle of incidence with respect to the sensor plane increases with η and consequently the track path length x also increases with η. The track path length for a straight track as a function

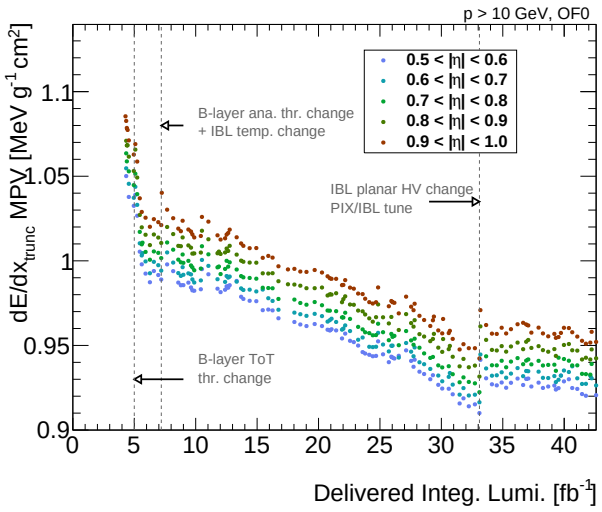

Figure 6.4: The most probable value of track $\mathrm{d}E/\mathrm{d}x$ measured in the pixel detector as a function of delivered integrated luminosity for data collected in 2015 and 2016. Tracks are required to have momentum >10 GeV and no hit in the IBL OF. Several jumps in $\mathrm{d}E/\mathrm{d}x$ are visible due to changing detector settings. Slices in η are plotted; the pixel detector at higher η measures a higher $\mathrm{d}E/\mathrm{d}x$ as expected.[†]

of η is shown in Figure 6.5.

Because this analysis selects for high $\mathrm{d}E/\mathrm{d}x$ tracks above a certain value in $\mathrm{d}E/\mathrm{d}x$, any η or run dependence must be corrected.

6.3.1 Run-dependent correction

The $\mathrm{d}E/\mathrm{d}x$ dependence on delivered integrated luminosity is corrected for on a run-by-run basis. A special inclusive dataset of high quality ID tracks with $p > 10$ GeV is used to maximize the amount of statistics available per run. For each run, the track $\mathrm{d}E/\mathrm{d}x$ is plotted separately for `IBL0` and `IBL1` tracks in bins of $|\eta|$. The $|\eta|$ bin edges are defined by $[0.0, 1.0, 1.4, 1.6, 1.8, 2.0, 2.1, 2.2, 2.3, 2.4, 2.5]$, where the bins are chosen to be larger at small

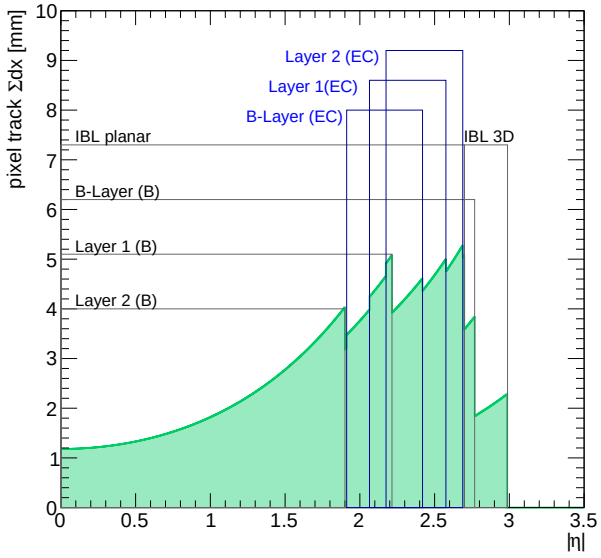

Figure 6.5: The track path length, or travelled distance through silicon sensor material, that a straight tracking originating from the interaction point has as a function of $|\eta|$. The $|\eta|$ coverage of the various pixel subdetectors is shown as overlaid boxes.

η largely due to lack of statistics. This is also well-motivated by the decreased $\mathrm{d}E/\mathrm{d}x$ dependence on η for small η (see 6.3.2). If there are $\geq$ 1000 tracks in the given (`IBL0/IBL1`, η) slice, then the distribution of track $\mathrm{d}E/\mathrm{d}x$ is fit with a modified Crystal Ball function. This is based on the traditional Crystal Ball function [110] and has the functional form:

$$f(x) = \begin{cases} N \exp\left[-\frac{\alpha^2}{2}\right] \left(\frac{n_1}{|\alpha|} / \left(\frac{n_1}{|\alpha|} - |\alpha| - \frac{x-x_0}{\sigma_1}\right)\right)^{n_1} & \frac{x-x_0}{\sigma_1} \leq -|\alpha| \\ N \exp\left[-\frac{1}{2}\left(\frac{x-x_0}{\sigma_1}\right)^2\right] & -|\alpha| < \frac{x-x_0}{\sigma} < 0 \\ N \exp\left[-\frac{1}{2}\left(\frac{x-x_0}{\sigma_2}\right)^{n_2}\right] & \frac{x-x_0}{\sigma_1} > 0 \end{cases} \tag{6.2}$$

with free parameters $N, \sigma_1, \sigma_2, x_0, n_1, n_2, \alpha$.

For each fit, x_0 is extracted as an estimator of the MPV of the distribution. Scale factors are then calculated using the estimated MPV to flatten the $\mathrm{d}E/\mathrm{d}x$ across the runs (with a handful of outliers systematically removed due to poor fits). Run 329716, which is the run in the dataset following the special run used for the $\mathrm{d}E/\mathrm{d}x$ vs $\beta\gamma$ run described in 6.4, is chosen as the normalization point. The resulting scale factors are shown in Figure 6.6 and are applied to the $\mathrm{d}E/\mathrm{d}x$ measurement for each track. If there is no scale factor in the correponding (`IBL0/IBL1`, η) slice for a given run, the scale factor for the preceding run which is closest in time is used.

6.3.2 η CORRECTION

A superset of the events used in the analysis regions described in Chapter 7 are used to calculate an η-dependent $\mathrm{d}E/\mathrm{d}x$ correction. Events are required to pass the $E_{\mathrm{T}}^{\mathrm{miss}}$ trigger, have at least one track

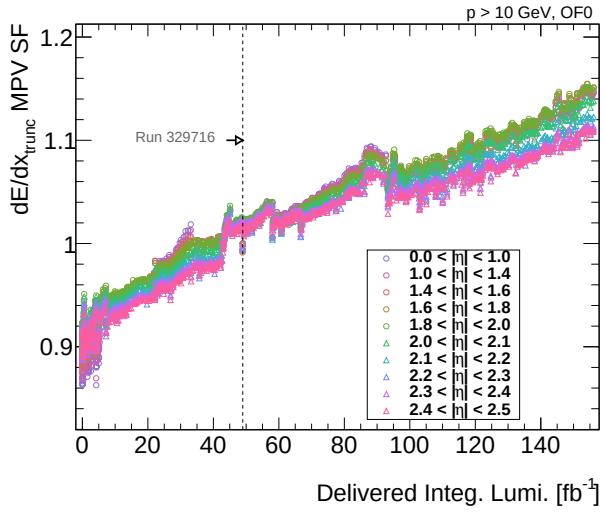

(a) `IBL0` tracks

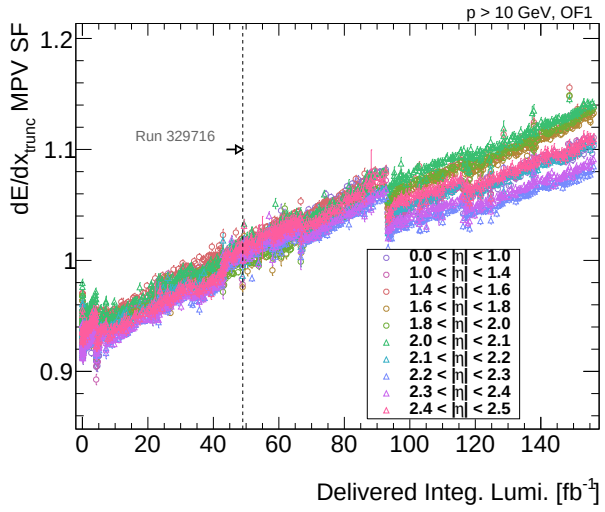

(b) `IBL1` tracks

Figure 6.6: The run-dependent scale factors for (a) `IBL0` tracks and (b) `IBL1` tracks.[†]

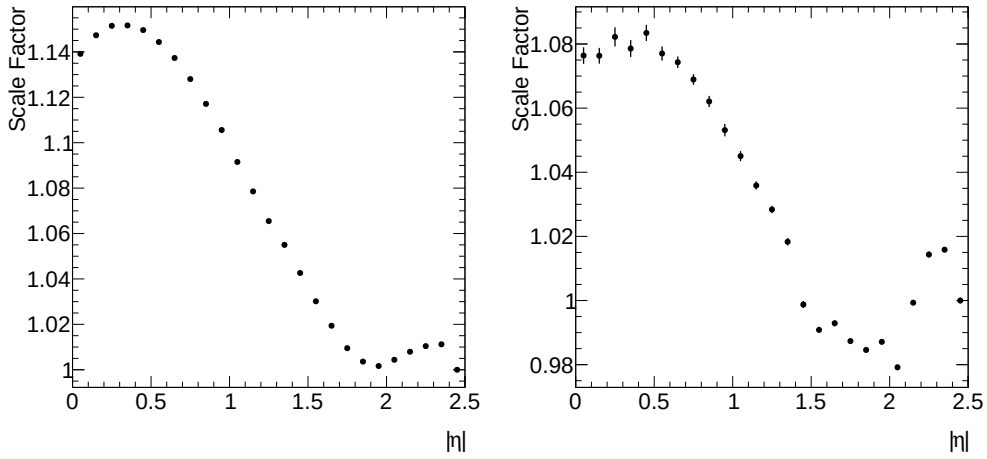

(a) `IBL0` tracks **(b)** `IBL1` tracks

Figure 6.7: The η-dependent scale factors for (a) `IBL0` tracks and (b) `IBL1` tracks.[†]

with $p_{\mathrm{T}} > 50$ GeV, and pass a set of loose track isolation criteria.

The track $\mathrm{d}E/\mathrm{d}x$ distribution for all ID tracks with $p_{\mathrm{T}} > 10$ GeV is sliced in $|\eta|$ in bins of 0.1 from 0 to 2.5 and fit with a Gaussian function within each slice. `IBL0` and `IBL1` tracks are also fit separately. The fit is restricted to a narrow region around the peak to avoid any bias due to the long Landau tail. Scale factors are derived and normalized to the highest $|\eta|$ bin which has the largest statistics. The factors are shown in Figure 6.7.

One should note that the corrections do not account for any changes in the shape of the $\mathrm{d}E/\mathrm{d}x$ distribution. The distributions for a run early in Run-2 and late in Run-2 are shown in Figure 6.8. Similarly, the $\mathrm{d}E/\mathrm{d}x$ distribution for different slices of η are shown in Figure 6.9. Tracks at higher η have a narrower $\mathrm{d}E/\mathrm{d}x$ distribution than those at lower η. The $\mathrm{d}E/\mathrm{d}x$ resolution degrades visibly with radiation damage. These remaining shape differences motivate η-dependent templates in the

background estimation, detailed in Chapter 8.

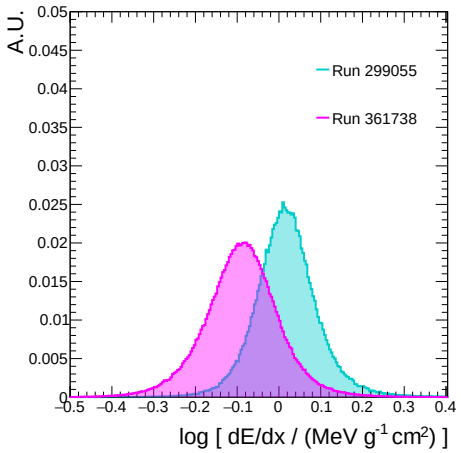

Figure 6.8: The log $\mathrm{d}E/\mathrm{d}x$ distributions for an early run taken at 4 fb^{-1} (Run 299055) and a late run taken at 146 fb^{-1} (Run 361738) delivered integrated luminosity, before run-by-run or η corrections are applied.[†]

6.4 Calibrating $\mathrm{d}E/\mathrm{d}x$ as a function of $\beta\gamma$

The mass m of a particle can be defined as

$$m = p/\beta\gamma, \tag{6.3}$$

where p is the momentum, $\beta = \frac{v}{c}$, and $\gamma = 1/\sqrt{1-\beta^2}$. The ID provides a momentum measurement, and the pixel $\mathrm{d}E/\mathrm{d}x$ measurement provides a probe of the particle $\beta\gamma$.

With a calibration of the dependence of $\mathrm{d}E/\mathrm{d}x$ on $\beta\gamma$, we can then measure the mass of each particle which makes a track in the detector. This particle ID technique is one of the cornerstones of the analysis strategy.

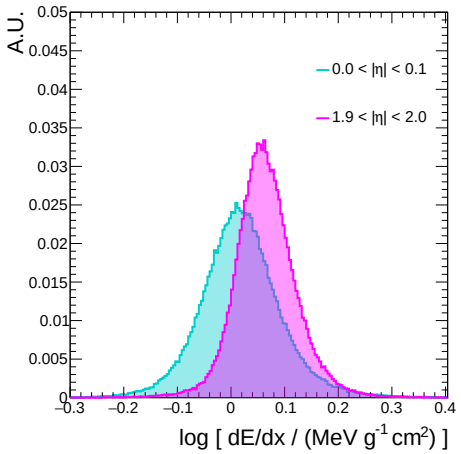

Figure 6.9: The log $\mathrm{d}E/\mathrm{d}x$ distributions in a single run for tracks with $|\eta|$ < 0.1 and 1.9 < $|\eta|$ < 2.0, before run-by-run or η corrections are applied.[†]

6.4.1 Special dataset

Massive new particles have low $\beta\gamma$ values relative to the most commonly produced particles at the LHC, e.g. pions, kaons, protons. For example, according to simulation, 2 TeV R-hadrons are produced with $\beta\gamma$ values which peak at about 0.4. So, the dependence of $\mathrm{d}E/\mathrm{d}x$ on $\beta\gamma$ must be calibrated for low values of $\beta\gamma$ in order to accurately reconstruct the mass of these heavy particles. This calibration cannot be performed using the standard tracks reconstructed in each dataset. The standard ATLAS tracking only reconstructs tracks with p_{T} greater or equal to 500 MeV. For a pion (mass $\approx$ 140 MeV), the $\beta\gamma$ distribution of standard tracks has a lower bound of $\sim$ 3.6. The distribution of $\beta\gamma$ values for a kaon, proton is limited to $\approx$ 1 and 0.5, respectively.

Therefore, the calibration is conducted using a special data run with low p_{T} track reconstruction down to 100 MeV. This run is a minimum bias run, which uses triggered coincidences in the

minimum bias trigger scintillators (MBTS) that do not privilege any particular physics process [111]. These data runs also have a lower number of interactions per beam crossing, or μ, with respect to the other runs. Because tracking reconstruction is, essentially, a combinatorics problem, the lower μ value for this run reduces the computational expense of running low p_{T} reconstruction for this run.

6.4.2 Calibration procedure

The calibration strategy relies on the fact that, for a fixed momentum, the various particles in the low p_{T} dataset have distinct $\mathrm{d}E/\mathrm{d}x$ distributions. Figure 6.10 shows the $\mathrm{d}E/\mathrm{d}x$ distribution for tracks in a narrow slice of momentum. In a given slice the momentum can be treated as "fixed" and a multi-peak structure emerges in the $\mathrm{d}E/\mathrm{d}x$ distribution. This multi-peak structure can be attributed to the superposition of pion, kaon, and proton contributions. Because these are particles with known masses, the $\beta\gamma$ values corresponding to a fixed slice of momentum can be calculated.

To derive the calibration, tracks from the low p_{T} dataset are sliced evenly in log-momentum space with bounds at $10^{2+.004i}$ MeV for $0 < i < 75$. Tracks are also separated into `IBL0` and `IBL1` tracks and binned in the same η slices as defined in Section 6.3.1. The resulting $\mathrm{d}E/\mathrm{d}x$ distributions in each $(p, |\eta|, \texttt{IBL0/IBL1})$ slice are fit with a superposition of modified Crystal Ball functions to extract the positions of the peaks (Equation 6.2).

An additional correction to the momentum measured for each particle is required due to an assumption during ATLAS reconstruction that most tracks are produced by pions. This assumption creates a bias at low momentum and results in an underestimated reconstructed momentum measurement for kaons and protons due to multiple scattering effects. A correction derived in [35] using

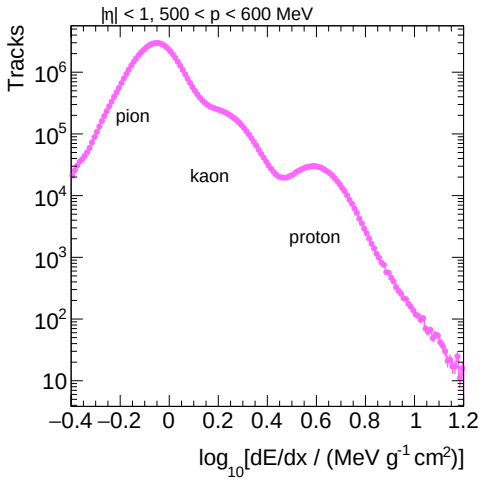

Figure 6.10: An example log $\mathrm{d}E/\mathrm{d}x$ distribution for tracks in Run 329542 with $|\eta| < 1$ and $500 < p < 600$ GeV. Three peaks are visible, which come from pions, kaons, and protons, from left to right.

simulated low momentum samples is applied.

Finally, the extracted $\mathrm{d}E/\mathrm{d}x$ peaks are then plotted as a function of the corresponding $\beta\gamma$. An example $\mathrm{d}E/\mathrm{d}x$ versus $\beta\gamma$ plot is shown in Figure 6.11 for a slice of $(|\eta|, q, \texttt{IBL0/IBL1})$. The points are then fit with an empirical function $g(x)$, given by

$$g(\beta\gamma) = \frac{1+(\beta\gamma)^2}{\beta\gamma}\left[a + b\log_{10}(\beta\gamma) + c\,\left[\log_{10}(\beta\gamma)\right]^2\right] \tag{6.4}$$

The resulting fit is then used to map a measured track $\mathrm{d}E/\mathrm{d}x$ to a $\beta\gamma$ value.

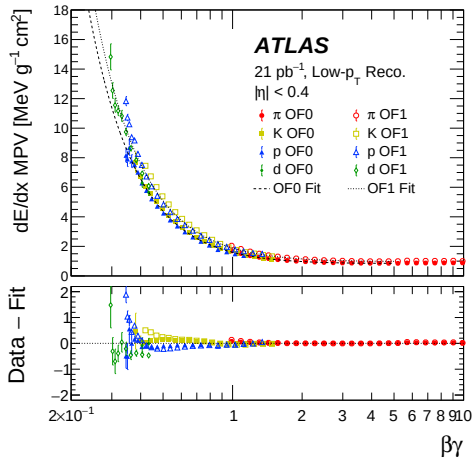

Figure 6.11: An example of the fitted MPV values of $\mathrm{d}E/\mathrm{d}x$ as a function of $\beta\gamma$, for tracks with $|\eta| < 0.4$ split into `IBL0` and `IBL1` tracks [11].

7

Analysis strategy

The $\mathrm{d}E/\mathrm{d}x$ measurement in the pixel detector gives us a very powerful handle in the search for new physics with the ATLAS experiment. The search described in the following chapters exploits this measurement to search for long-lived particles in a relatively model-independent manner.

By virtue of their large masses, heavy new particles are expected to travel more slowly than the average particle at the LHC. Figure 3.1 shows the theoretical dependence of mean energy loss on $\beta\gamma$.

Figure 6.11 shows the most probable measured track $\mathrm{d}E/\mathrm{d}x$ as a function of $\beta\gamma$ with the ATLAS detector. Both of these plots show that slower particles, or particles with $\beta\gamma < 1$, will have large $\mathrm{d}E/\mathrm{d}x$ compared to particles with $\beta\gamma > 1$. The $\mathrm{d}E/\mathrm{d}x$ measurement therefore provides us with an excellent tool to discriminate any potential new massive charged particles from SM background. Furthermore, using the calibration of $\mathrm{d}E/\mathrm{d}x$ as a function of $\beta\gamma$ described in Chapter 6, the particle $\beta\gamma$ can be determine from the associated $\mathrm{d}E/\mathrm{d}x$ measurement and combined with a particle momentum measurement to reconstruct the particle mass.

This search strategy can be used to detect signatures of new physics, including SUSY particles, in a way which is mostly agnostic to specific theoretical details. In Chapter 2, models which predict long-lived charginos, sleptons, and gluinos are discussed. The search power of this analysis will be benchmarked on these sparticles, but the search is designed to be generically sensitive to new heavy charged particles with lifetimes of $\sim$1 ns or longer.

7.1 Signal Models

Three Feynman diagrams are shown in Figure 7.1, one for each benchmark signal model. In the context of SUSY, the chargino model probes our sensitivity to Anomaly-Mediated Supersymmetry Breaking (AMSB) models and the slepton model probes our sensitivity to Gauge-Mediated Supersymmetry Breaking (GMSB) models. These two SUSY-breaking mechanisms can result in long-lived charginos and sleptons. The gluino model probes our sensitivity to split-SUSY models. The signals are simulated in the context of *simplified* models, which are described in Chapter 2. Monte Carlo

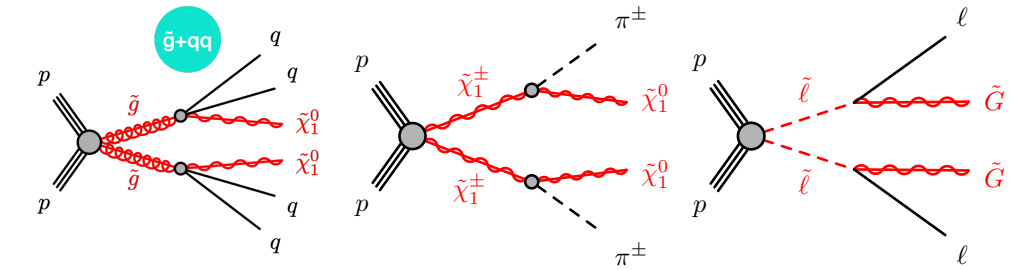

(a) gluino **(b)** chargino **(c)** slepton

Figure 7.1: Feynman diagrams for (a) pair-produced gluinos, (b) pair-produced charginos, and (c) pair-produced sleptons [112]. The pair-produced gluinos in (a) can hadronize and form R-hadrons, represented by the blue circle.

simulated events are generated and used to evaluate the analysis sensitivity. Samples with sparticles that are stable on the scale of the ATLAS detector, as well as *metastable* samples where a fraction of the pair produced sparticles (i.e. the charginos, gluinos, or sleptons) decay within the detector, were generated for this analysis. The metastable samples considered include lifetimes of 1 ns, 3 ns, 10 ns, and 30 ns for the slepton and gluino models, and 1 ns, 4 ns, 10 ns, and 30 ns for the chargino model. Monte Carlo samples were produced using MadGraph5_aMC@NLO [113], Pythia 8 [114] with the `A14_NNPDF23LO` tune [115], and EvtGen [116], with detector interactions simulated through Geant 4 [117].

7.1.1 Gluinos

Figure 7.1a depicts the production of pairs of long-lived gluinos from the LHC proton-proton collisions. Simulated events are produced across a range of gluino lifetimes and masses. The gluinos which decay before they escape the ATLAS detector each decay to two quarks and a neutralino.

Long-lived gluinos carry color charge and therefore hadronize and form colorless composite par-

ticles called R-hadrons. Although gluinos are neutral and do not produce tracks in our detector, the resulting R-hadrons are often charged and produce detectable tracks.

R-hadrons can also change composition as they travel through the detector, which complicates their simulation. Figure 7.2 shows the fraction of R-baryons, R-mesons, and gluinoballs assuming a 1.4 TeVgluino as a function of r in the detector, in simulation. An R-baryon consists of a gluino and a baryon, an R-meson consists of a gluino and a meson, and a gluinoball consists of a gluino and a gluon. A phenomenological framework describing the R-hadron mass spectra and material interactions is discussed in [118]. Details of the ATLAS R-hadron simulation using Pythia 8 [114] and Geant 4 [117] are found in [119].

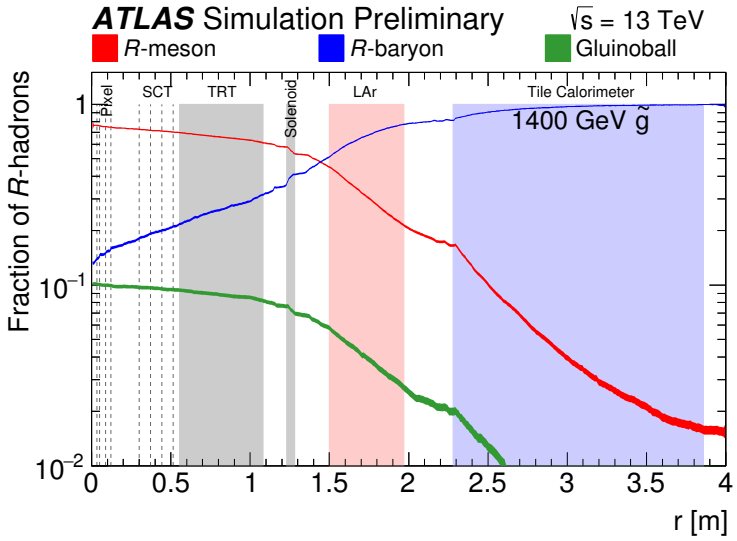

Figure 7.2: For a 1.4 TeV gluino which travels through the detector, the probability that it will be a R-baryon, R-meson, or gluinoball changes as as a function of r [119].

There are two sets of gluino signals: one fixes the neutralino mass to 100 GeV while the other fixes

the mass difference Δm between the gluino and the neutralino at 30 GeV. These two sets of signals explore different areas of kinematic phase space.

7.1.2 Charginos

To probe an AMSB scenario, events containing a superposition of $\tilde{\chi}_1^{\pm}\,\tilde{\chi}_1^0$ and $\tilde{\chi}_1^{\pm}\,\tilde{\chi}_1^{\mp}$ are produced in simulation. The Feynman diagram for the latter contribution is shown in Figure 7.1b. The lightest charginos are pair-produced and decay to soft pions and neutralinos. The mass difference between the lightest chargino and neutralino is set to be approximately 170 MeV. For $\tilde{\chi}_1^{\pm}\,\tilde{\chi}_1^0$ production, the chargino decays in the same manner while the neutralino is assumed to be stable.

For the chargino samples, $\tilde{\chi}_1^{\pm}\,\tilde{\chi}_1^0$ and $\tilde{\chi}_1^{\pm}, \tilde{\chi}_1^{\pm}$ are produced separately and then added for each mass and lifetime point.

7.1.3 Sleptons

In the GMSB scenario, the NLSP can easily be a slepton. Events which contain pair-produced sleptons, specifically staus, are generated. Each stau decays to a tau and a gravitino, as shown in Figure 7.1c. A very light gravitino in the GMSB scenario will result in a long-lived stau, so for simplicity the gravitino is assumed to be massless.

Note on choice of signals The 36 fb^{-1} version of this analysis used gluinos as the only benchmark [35]. As shown in Figure 7.3, gluinos, which are strongly produced, have cross sections that are an order of magnitude larger than sleptons or charginos for a given mass. With the full Run-

2 dataset, ATLAS has sensitivity to sparticles which are produced through electroweak processes. In order to exploit this fact the analysis is expanded to look for charginos and sleptons.

The decision to consider slepton and chargino models not only lets us probe two SUSY-breaking mechanisms but also serves to cover areas of phase space with different detector signatures. The chargino model explores the analysis sensitivity to theorized sparticles which decay to a nearly degenerate daughter sparticle, while the slepton model explores the sensitivity when the daughter sparticle is massless. The use of two sets of gluino models also serve a similar purpose, with the added complication of hadronization.

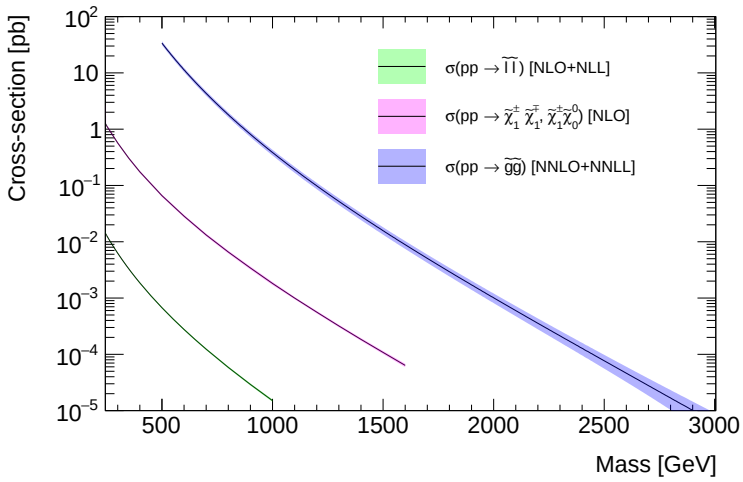

Figure 7.3: The cross sections for the various sparticles as a function of mass. The slepton cross sections are calculated at NLO-NLL for a superposition of left and right-handed sleptons [120–125]. The chargino cross sections are calculated at NLO using `Prospino2` [124, 126]. The gluino cross sections are calculated at NNLO-NNLL$_{\text{approx}}$ [127–135].†

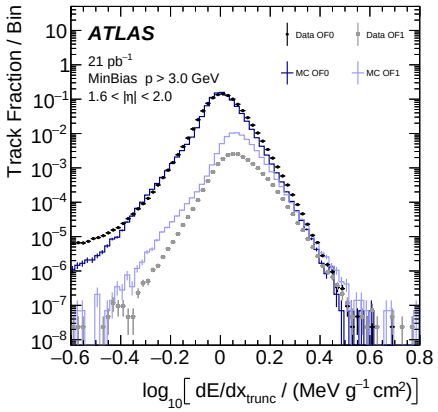

Figure 7.4: A comparison of the log $\mathrm{d}E/\mathrm{d}x$ distribution from simulation and minimum bias data, for an example slice of η. `IBL0` `IBL1` tracks are shown separately. The simulated $\mathrm{d}E/\mathrm{d}x$ distribution does not accurately reflect the shape in data [11].

7.1.4 $\mathrm{d}E/\mathrm{d}x$ DATA-DRIVEN TEMPLATE

$\mathrm{d}E/\mathrm{d}x$ is difficult to model in simulation due to its sensitivity to detector conditions and radiation effects, as discussed in Chapter 6. This motivates the use of a data-driven template to derive the $\mathrm{d}E/\mathrm{d}x$ values for signal events.

The template is derived from the 2017 low p_{T}, low μ dataset used for the $\mathrm{d}E/\mathrm{d}x$ to $\beta\gamma$ calibration. The template depends on the calibration (see 6.4.2 for a description). The fitted $\mathrm{d}E/\mathrm{d}x$ distributions for slices in momentum, $|\eta|$, and (`IBL0`,`IBL1`) are separated into the various particle contributions (pion, kaon, proton). The $\mathrm{d}E/\mathrm{d}x$ distributions are then averaged across the different particles as a function of $\beta\gamma$. This results in a $\mathrm{d}E/\mathrm{d}x$ vs $\beta\gamma$ template that is derived in bins of η and (`IBL0`,`IBL1`). The probability of having a hit in the IBL overflow, for a given η, is also derived as a function of $\beta\gamma$ by calculating the proportion of `IBL1` tracks in bins of η.

Then, both the $\mathrm{d}E/\mathrm{d}x$ value and the IBL OF bit value for signal tracks are replaced by drawing from this template. The simulated η and $\beta\gamma$ value associated to each track is used to draw randomly from the template. First, the IBL OF bit is determined. Then, the $\mathrm{d}E/\mathrm{d}x$ value is drawn from the corresponding $\mathrm{d}E/\mathrm{d}x$ vs $\beta\gamma$ template.

The difference in simulated $\mathrm{d}E/\mathrm{d}x$ and values drawn from the template is shown in Figure 7.4. The distribution derived from data is much wider than that in simulation, likely due to the effect of radiation damage and motivating the use of the data-driven template.

7.2 Selection

To search for these theorized particles, this analysis takes the full Run-2 dataset and applies a series of selections, summarized in Figure 7.5. Events are filtered with a set of event-level requirements. Then ID tracks from events which pass the requirements are filtered with a set of track-level requirements. Tracks which pass both of these filters make up the inclusive signal region `SR-Inclusive`. If multiple tracks in an event pass the requirements, then only the leading track in p_{T} is included in the signal region.

The signal region is conceptually a region in kinematic phase space optimized to be enriched in potential signal and depleted in SM background. It is defined without looking at the data in the region to minimize any bias introduced by over-optimizing the signal region definition to enhance anomalous events in data. Each of the selection requirements is explained in the following section.

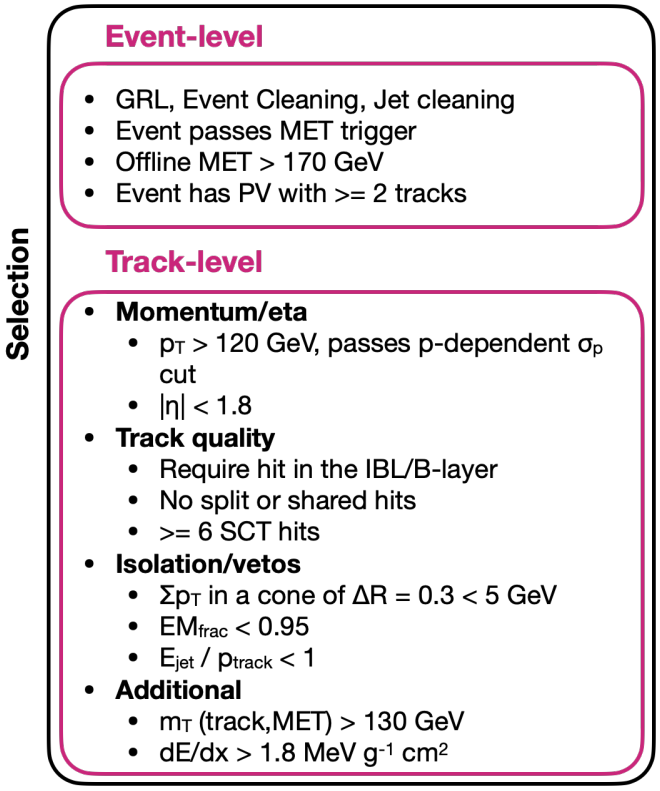

Figure 7.5: A summary of the event and track selection applied to events. The track with the largest p_T passing these track selections and belong to an event which passes the event selections is included in the `SR-Inclusive` signal region.

7.2.1 Event-level selection

Pre-selection Events are required to come from runs which pass the Good Run List (GRL), which contains a list of runs which meet ATLAS data quality requirements. Events must also pass basic event cleaning requirements which remove events in which any subdetector had a raised error flag. A custom jet cleaning requirement is also applied to remove events with noisy calorimeter signals and non-collision background events.

Trigger Events are triggered using the $E_{\mathrm{T}}^{\mathrm{miss}}$ trigger described in Chapter 5.

Because this analysis is designed to look for high $\mathrm{d}E/\mathrm{d}x$, high p_{T} tracks, ideally events would be triggered using a track-based trigger. However, because tracking is computationally time-expensive, tracking was not available at HLT in Run-2 and therefore the $E_{\mathrm{T}}^{\mathrm{miss}}$ trigger is used.

The overall efficiency of the $E_{\mathrm{T}}^{\mathrm{miss}}$ trigger is dependent on the event topology. High online $E_{\mathrm{T}}^{\mathrm{miss}}$ (trigger-level $E_{\mathrm{T}}^{\mathrm{miss}}$) values result from objects which are invisible to the online $E_{\mathrm{T}}^{\mathrm{miss}}$ calculation. As discussed in Chapter 5, the online $E_{\mathrm{T}}^{\mathrm{miss}}$ calculation is based on energy deposits in the calorimeter and is independent of measurements in the muon or tracking subsystems.

An event with two stable sparticles can have high online $E_{\mathrm{T}}^{\mathrm{miss}}$ if they are accompanied by an energetic Initial State Radiation (ISR) jet. The online $E_{\mathrm{T}}^{\mathrm{miss}}$ calculation will include a large energy contribution from the ISR jet, but the sparticles interact minimally with the calorimeter and therefore are largely invisible to the online $E_{\mathrm{T}}^{\mathrm{miss}}$ calculation. An event with two sparticles decaying inside the detector can have high online $E_{\mathrm{T}}^{\mathrm{miss}}$ if the sparticles decay to neutral particles. In the chargino

model, the chargino decays to a neutralino, while in the the slepton model, the slepton decays to a gravitino. Both the gravitino and the neutralino are neutral particles and are invisible to the online $E_{\mathrm{T}}^{\mathrm{miss}}$ calculation. Figure 7.6 illustrates these two scenarios.

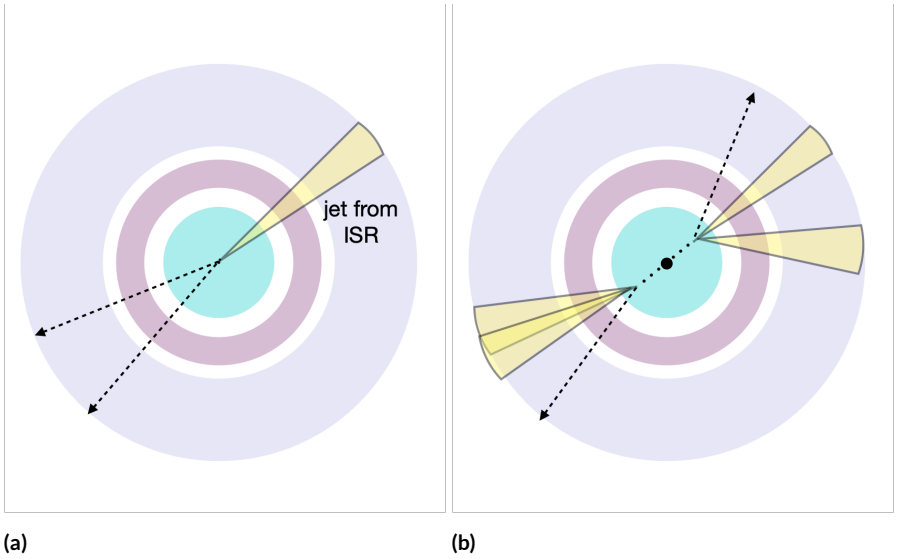

Figure 7.6: Cartoons of event topologies which result in significant online $E_{\mathrm{T}}^{\mathrm{miss}}$. The dotted lines represent tracks which are invisible to the online $E_{\mathrm{T}}^{\mathrm{miss}}$ calculation, and the yellow wedges represent a jet or series of calorimeter deposits. In (a) two sparticles travel in the opposite direction of the initial state radiation jet. This results in signficant online $E_{\mathrm{T}}^{\mathrm{miss}}$ because the sparticles leave minimal deposits in the calorimeters and are effectively invisible. In (b), two sparticles are pair produced and each sparticle decays to two jets and another sparticle (the LSP). The LSP is invisible and therefore the event looks imbalanced.

Figures 7.7 and 7.8 show the efficiency of simulated events to pass both the trigger and jet cleaning requirements for various signals. Any inefficiency largely comes from the trigger requirement since the jet cleaning requirement is $> 98\%$ efficient for all signals. Note that the metastable $\tilde{\chi}_1^0\,\tilde{\chi}_1^{\pm}$ and $\tilde{\chi}_1^{\pm}\,\tilde{\chi}_1^{\mp}$ signals have a truth-level $E_{\mathrm{T}}^{\mathrm{miss}} > 60$ GeV filter, with the exception of the $m = 600$ GeV, $\tau = 30$ ns point.

Across all signal models, the efficiency of triggering on stable signals is lower than on metastable

signals. Triggering on stable signals necessitates an energetic jet coming from initial state radiation. The trigger efficiency also increases as the sparticle lifetime decreases. The probability that the sparticles decay and leave significant energy deposits in the calorimeter is larger for sparticles with shorter lifetimes. Furthermore, the trigger efficiency of metastable signals also increases with the parent sparticle mass because the decay products will be more energetic, resulting in higher trigger-level $E_{\mathrm{T}}^{\mathrm{miss}}$ per event.

The efficiencies also depend on the specific model decay kinematics for metastable signals. $\tilde{\chi}_1^0\,\tilde{\chi}_1^{\pm}$ and $\tilde{\chi}_1^{\pm}\,\tilde{\chi}_1^{\mp}$ metastable samples have lower trigger efficiencies than the slepton metastable samples for the same mass and lifetime. This can be explained by considering the rest frame of the $\tilde{\chi}_1^{\pm}$. Because the $\tilde{\chi}_1^0$ and $\tilde{\chi}_1^{\pm}$ masses are nearly degenerate (the mass difference is about 170 MeV), there is little phase space available to the pion and $\tilde{\chi}_1^0$ decay products. The decay products will therefore be soft and the event will have less online $E_{\mathrm{T}}^{\mathrm{miss}}$ with respect to the slepton samples, which have more phase space available to the decay products due to the assumption that the gravitino is light.

Offline $E_{\mathrm{T}}^{\mathrm{miss}}$ Events are required to have $E_{\mathrm{T}}^{\mathrm{miss}} > 170$ GeV. Offline $E_{\mathrm{T}}^{\mathrm{miss}}$ is described in Chapter 5 and is calculated using ID tracks, muons, electrons, and jets.

The sources of offline $E_{\mathrm{T}}^{\mathrm{miss}}$ also vary significantly depending on event topology. In events with sparticles which decay to neutral LSPs, the LSP will carry away energy and be a source of $E_{\mathrm{T}}^{\mathrm{miss}}$. In events with two stable sparticles, there is no real $E_{\mathrm{T}}^{\mathrm{miss}}$ in the form of invisible neutral particles. Instead, significant $E_{\mathrm{T}}^{\mathrm{miss}}$ can either come from poor momentum measurement or ID tracks failing the requirements to enter the objects considered in the $E_{\mathrm{T}}^{\mathrm{miss}}$ calculation.

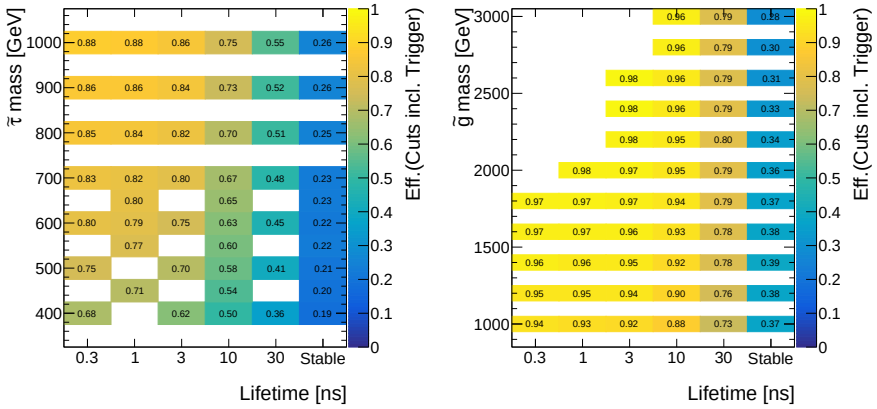

(a) slepton **(b)** gluino, m_{χ} = 100 GeV

Figure 7.7: The efficiency of simulated signal events for (a) sleptons and (b) gluinos with m_{χ} = 100 GeV to pass both the jet cleaning and trigger requirements as a function of lifetime and mass.[†]

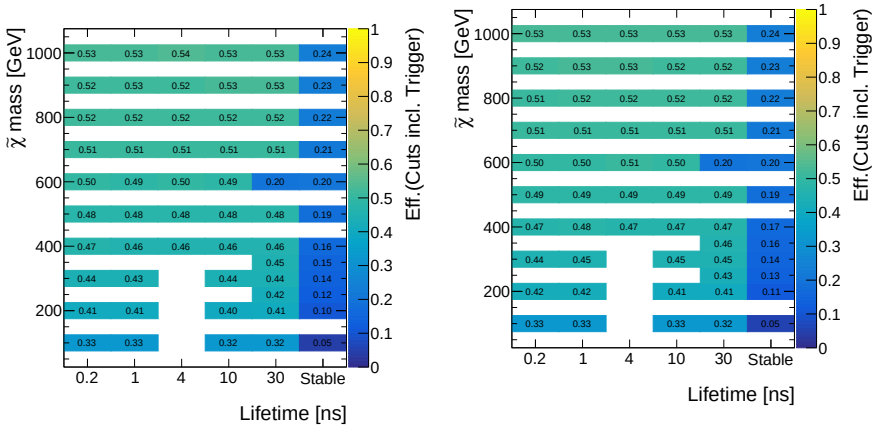

(a) $\tilde{\chi}_1^{\pm}\ \tilde{\chi}_1^{\mp}$ **(b)** $\tilde{\chi}_1^{\pm}\ \tilde{\chi}_1^{0}$

Figure 7.8: The efficiency of simulated signal events for (a) $\tilde{\chi}_1^{\pm}\ \tilde{\chi}_1^{\mp}$ and (a) $\tilde{\chi}_1^{\pm}\ \tilde{\chi}_1^{0}$ to pass both the jet cleaning and trigger requirements as a function of lifetime and mass. Note that the truth-level $E_{\mathrm{T}}^{\mathrm{miss}}$ is required to be greater than 60 GeV for all metastable samples, with the exception of the m = 600 GeV, τ = 30 ns points.[†]

The $E_{\mathrm{T}}^{\mathrm{miss}}$ distributions after the trigger requirement are shown in Figures 7.9 for a few signal points. Stable signals have soft $E_{\mathrm{T}}^{\mathrm{miss}}$ distributions, while the metastable signals have significantly larger $E_{\mathrm{T}}^{\mathrm{miss}}$ distributions due to the neutral particle decay products. Events with a $\tilde{\chi}_1^{\pm}\,\tilde{\chi}_1^0$ pair have slightly more $E_{\mathrm{T}}^{\mathrm{miss}}$ than events with a $\tilde{\chi}_1^{\pm}\,\tilde{\chi}_1^{\mp}$ pair. This is because the $\tilde{\chi}_1^{\pm}\,\tilde{\chi}_1^0$ pair contains a neutral sparticle.

Primary Vertex The primary vertex in each event is required to have two or more associated tracks.

7.2.2 Track-level selection

Track p_{T} and η Candidate ID tracks must be associated to the primary vertex and have $p_{\mathrm{T}} >$ 120 GeV. As seen in Figure 7.10a, the sparticle tracks are energetic and peak at large values of p_{T}, depending on the sparticle mass, while the background falls rapidly with p_{T}.

To ensure that we are accepting well-measured tracks, a momentum uncertainty requirement is applied to the tracks. The momentum uncertainty cut is defined as a linear cut dependent on the momentum of the track. The uncertainty $\sigma_p = \sigma(q/p)/(q/p)$ is required to be:

$$\sigma_p < \min\left(f(p), 2.0\right), \tag{7.1}$$

where

$$f\left(p\right) = \max\left(.01 + 0.9|p|[\mathrm{TeV}], 0.1\right) \tag{7.2}$$

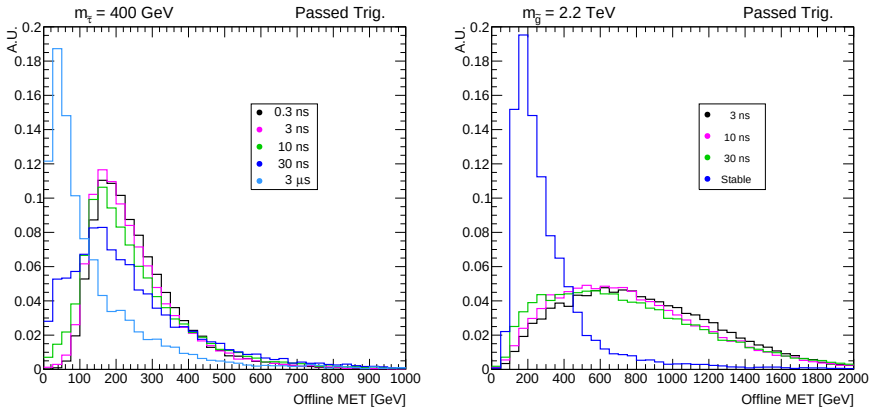

(a) slepton

(b) gluino, m_{χ} = 100 GeV

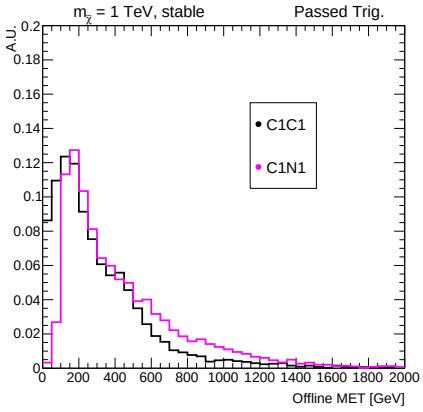

(c) $\tilde{\chi}_1^{\pm}\,\tilde{\chi}_1^{\mp}, \tilde{\chi}_1^{\pm}\,\tilde{\chi}_0^{\pm}$

Figure 7.9: The $E_{\mathrm{T}}^{\mathrm{miss}}$ distributions for (a) 400 GeV sleptons, (b) 2.2 TeV gluinos with m_{χ} = 100 GeV, and (c) stable $\tilde{\chi}_1^{\pm}\,\tilde{\chi}_1^{\mp}$ (referred to as C1C1) and $\tilde{\chi}_1^{\pm}\,\tilde{\chi}_0^{\pm}$ (C1N1) samples with m = 1 TeV, after requiring the that the event pass the trigger and jet cleaning.[†]

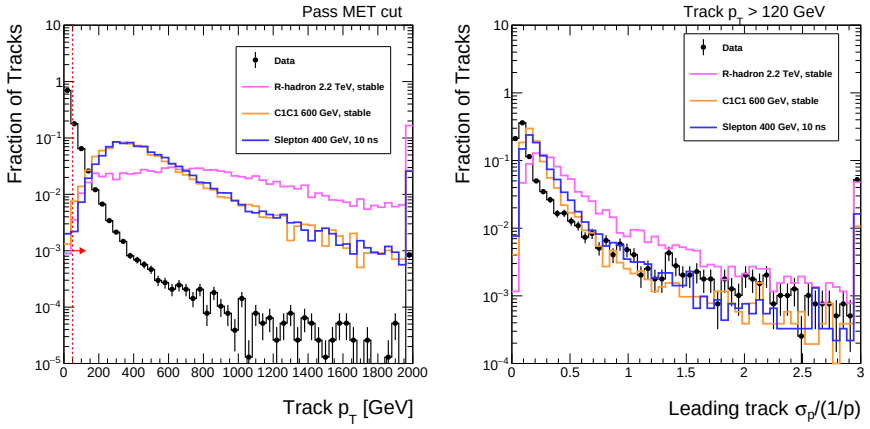

(a) Track p_{T} **(b)** Track σ_p

Figure 7.10: The (a) track p_{T} distribution for all tracks and (b) the momentum uncertainty for the highest p_{T} track. All event-level requirements are applied, and tracks are required to have p_{T} > 120 GeV in (b). Tracks in signal events must be matched to a sparticle. Data is from a portion of the 2018 run. The last bin includes all of the entries in overflow of the plot range.[†]

Tracks are also required to have $|\eta| < 1.8$. The signal particles are produced centrally (i.e. small η) as shown in Figure 7.11a), while the background is less central and has large spikes at high η largely consisting of poor quality tracks. A cut is placed at 1.8 to reduce background and to avoid barrel-endcap transition region, where the number of layers traversed by a particle originating from the collision point changes rapidly (therefore complicating the $\mathrm{d}E/\mathrm{d}x$ measurement).

Track quality Tracks missing a hit in the first layer of the pixel detector often come from photons converting into electron-positron pairs. To reject these tracks, candidate ID tracks must have a hit in the first expected layer (either the IBL or B-layer depending on the detector region).

As discussed in Chapter 5, due to the high particle multiplicity environment at the LHC, clusters are often shared between multiple tracks. Because particle tracks which overlap and ionize the

same pixel can lead to an anomalous large $\mathrm{d}E/\mathrm{d}x$, tracks containing split or shared hits are vetoed. Shared hits are clusters which are used in multiple tracks, and split hits are associated to single tracks but were assigned a high probability of belonging to more than one track by the neural network described in Chapter 5. The distribution of the number of split and shared hits is shown in Figure 7.11b.

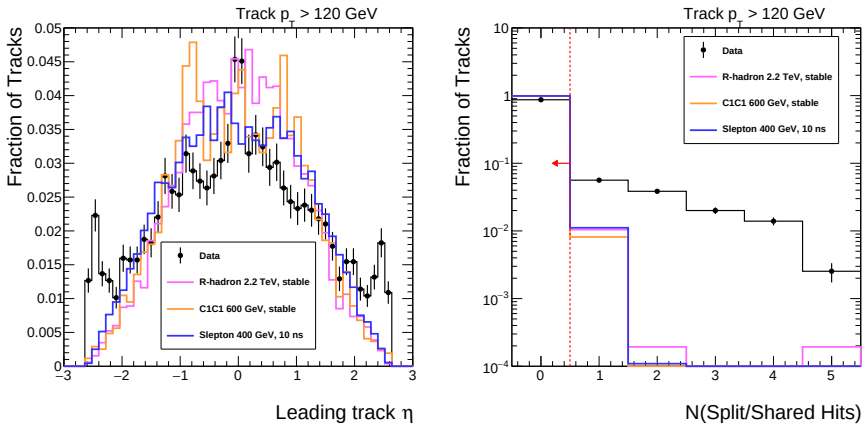

(a) Track η **(b)** Split/shared hits

Figure 7.11: The (a) η and (b) number of split and shared hits associated to the highest p_{T} track. All event-level requirements are applied, and the track is required to have p_{T} > 120 GeVin (b). Tracks in signal events must be matched to a sparticle. Data is from a portion of the 2018 run. The last bin includes all of the entries in overflow of the plot range.[†]

Tracks are additionally required to have at least six SCT hits. The distribution of SCT hits is shown in Figure 7.12b. The distribution was found to have a pileup dependence, where tracks with 5 or fewer SCT hits increase with increasing average μ.

Track isolation and jet vetos The long-lived signals considered create relatively isolated ID tracks. To reject jet-like background, the scalar sum of p_{T} for any tracks in a cone of $\Delta R = 0.3$

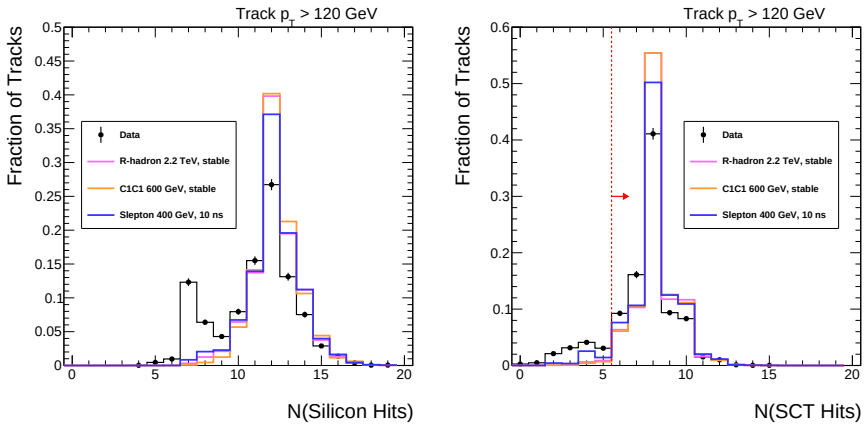

(a) N(silicon hits) **(b)** N(SCT hits)

Figure 7.12: The number of (a) silicon hits and (b)SCT hits associated to the highest p_{T} track. All event-level requirements are applied, and the track is required to have p_{T} > 120 GeV. Tracks in signal events must be matched to a sparticle. Data is from a portion of the 2018 run. The last bin includes all of the entries in overflow of the plot range.[†]

around the candidate track is calculated. The distribution of Σp_{T} is shown in Figure 7.13a, and Σp_{T} is required to be less than 5 GeV.

Candidate tracks are also associated to the nearest jet with $p_{\mathrm{T}} > 20$ GeV in a cone of $\Delta R = 0.4$. If the jet energy is greater than the track momentum, then the track is vetoed. This requirement vetos hadronic particles, which are expected to leave large energy deposits in the calorimeter. The distribution of $E_{\mathrm{jet}}/p_{\mathrm{track}}$ is shown in Figure 7.13b.

Jets with a high fraction of energy in the EM calorimeter are likely to be electrons. The distribution of the EM energy fraction in shown in Figure 7.14a. The associated jet is also required to have less than 95% of its energy in the electromagnetic calorimeter.

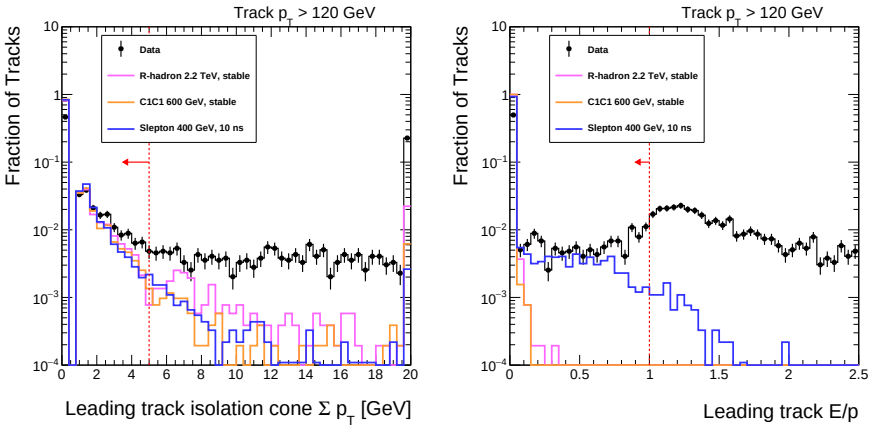

(a) Track isolation **(b)** jet E / track p

Figure 7.13: The (a) Σp_{T} of tracks in a cone of $\Delta R = 0.3$ around the candidate track and (b) the ratio of associated jet energy and track momentum, where the track plotted is the highest p_{T} track in the event. All event-level requirements are applied, and the track is required to have p_{T} > 120 GeV. Tracks in signal events must be matched to a sparticle. Data is from a portion of the 2018 run. The last bin includes all of the entries in overflow of the plot range.[†]

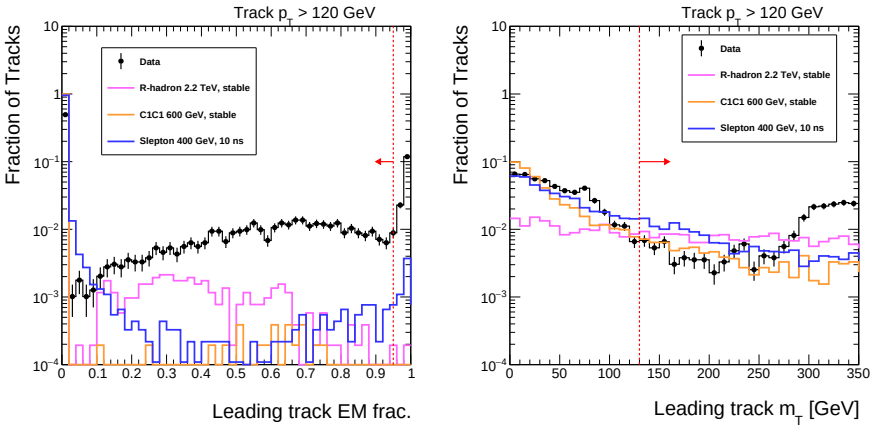

(a) Jet energy EM fraction **(b)** Transverse mass

Figure 7.14: The (a) fraction of jet energy in the EM calorimeter for the nearest associated jet within a $\Delta R = 0.4$ cone to the candidate track, and the (b) m_T distribution for the candidate track and the $E_{\mathrm{T}}^{\mathrm{miss}}$. All event-level requirements are applied, and the track is required to have p_{T} > 120 GeVand to be the highest p_{T} track in the event. Tracks in signal events must be matched to a sparticle. Data is from a portion of the 2018 run. The last bin includes all of the entries in overflow of the plot range.[†]

m_{T} REQUIREMENT To reject events containing W boson decays, the m_T of the track and the $E_{\mathrm{T}}^{\mathrm{miss}}$ is required to be greater than 130 GeV (see Figure 7.14b). m_T is defined as

$$m_T = \sqrt{2E_{\mathrm{T}}^{\mathrm{miss}}\, p_{\mathrm{T}}\,(1 - \cos\Delta\phi)}, \tag{7.3}$$

where p_{T} refers to the p_{T} of the candidate track, and $\Delta\phi$ is the azimuthal angle between the $E_{\mathrm{T}}^{\mathrm{miss}}$ vector and the track.

IONIZATION REQUIREMENT The distribution of $\mathrm{d}E/\mathrm{d}x$ for expected background and signal is shown in Figure 7.15a. All candidate tracks are required to have track $\mathrm{d}E/\mathrm{d}x$ greater than 1.8 $\mathrm{MeV\ g^{-1}cm^2}$. Additionally, the $\mathrm{d}E/\mathrm{d}x$ calculation is required to have at least two averaged pixel hits. The distribution of used pixel hits is shown in Figure 7.15b.

7.3 SIGNAL REGION DEFINITIONS

After applying the event selection, the leading p_{T} track in each event which passes the track-selection is added to the `SR-Inclusive` signal region. Note that `SR-Inclusive` is a collection of tracks, rather than a collection of events.

The tracks in the `SR-Inclusive` region are further divided into various channels. Tracks passing the `SR-Inclusive` requirements are categorized into one of six *exclusion* regions based on (a) muon identification, (b) whether there is an associated hit in the IBL overflow, and (c) $\mathrm{d}E/\mathrm{d}x$ value. Alternatively, tracks are categorized solely by their $\mathrm{d}E/\mathrm{d}x$ value into one of two *discovery* regions.

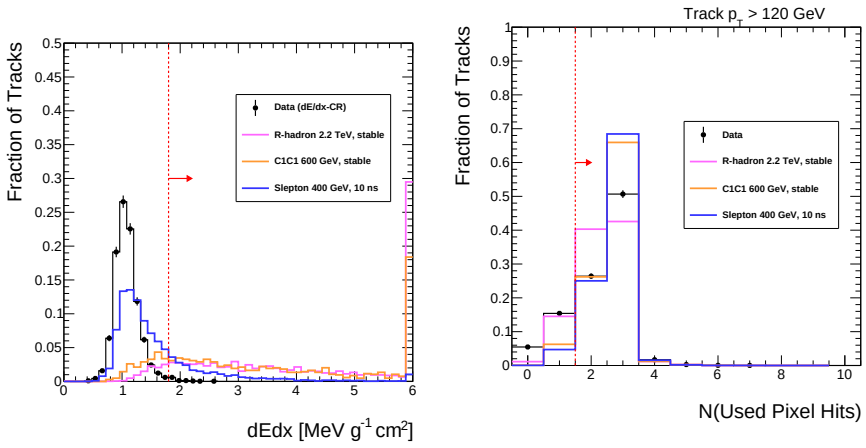

(a) Track $\mathrm{d}E/\mathrm{d}x$

(b) N(Used Pixel Hits) in the $\mathrm{d}E/\mathrm{d}x$ calculation

Figure 7.15: (a) The $\mathrm{d}E/\mathrm{d}x$ distribution for tracks which pass all other track-level and event-level selections, with the exception of the $E_{\mathrm{T}}^{\mathrm{miss}}$ cut which is inverted for data. (b) The number of used hits in the $\mathrm{d}E/\mathrm{d}x$ calculation for the largest p_{T} track with p_{T} > 120 GeV, where all event-level selections are applied. Tracks in signal events must be matched to a sparticle. Data is from a portion of the 2018 run. The last bin includes all of the entries in overflow of the plot range.[†]

The exclusion channels are optimized to exclude various signal models, while the discovery channels yields are less affected by specifics of the model and easier to reinterpret for models other than the benchmark models. The various channels are defined in Table 7.1.

MUON IDENTIFICATION Tracks which are categorized into the `SR-Mu-IBL0_Low`, `SR-Mu-IBL0_High`, and `SR-Mu-IBL1` channels are required to be associated to medium muons that pass a `FixedCutLoose` isolation requirement with $|\eta| < 2.7$, $p_{\mathrm{T}} > 25$ GeV, d_0 significance < 3, and $z_0 < 0.5$ mm.

The fraction of tracks reconstructed as a muon for data and signal is shown in Figure 7.17a. Although the muon information is useful in discriminating signal from background for lower mass

Channel	Muon?	IBL1?	$\mathrm{d}E/\mathrm{d}x$ [MeV g^{-1}cm^2]	Type
SR-Trk-IBL0_Low	No	No	[1.8, 2.4]	Exclusion
SR-Trk-IBL0_High	No	No	> 2.4	Exclusion
SR-Trk-IBL1	No	Yes	> 1.8	Exclusion
SR-Mu-IBL0_Low	Yes	No	[1.8, 2.4]	Exclusion
SR-Mu-IBL0_High	Yes	No	> 2.4	Exclusion
SR-Mu-IBL1	Yes	Yes	> 1.8	Exclusion
SR-Inclusive_Low	Agnostic	Agnostic	[1.8, 2.4]	Discovery
SR-Inclusive_High	Agnostic	Agnostic	> 2.4	Discovery

Table 7.1: Tracks in SR-Inclusive are categorized into the various signal region channels. The first six make up the exclusion channels, and the last two make up the discovery channels.

signals and is thus used in track categorization, requiring that all SR-Inclusive tracks be associated to muons would greatly reduce the selection efficiency for higher mass signals. This is evident in Figure 7.17a, where a larger fraction of stable m = 600 GeV $\tilde{\chi}_1^{\pm}$ $\tilde{\chi}_1^{\pm}$ tracks compared to m = 2.2 TeV R-hadron tracks are reconstructed as muons. This is largely driven by the slower speed of the heavy R-hadron particles. Sparticles with lower masses and therefore larger β are more likely to be reconstructed as muons because the MDT drift circle calculation in reconstruction assumes that incident particles are traveling at the speed of light [136]. The muon reconstruction efficiency as a function of particle β value is shown in Figure 7.16 for simulated chargino events and is seen to drop rapidly for small β. Additionally, R-hadrons can change quark content as they travel through the detector, which also reduces their probability of being reconstructed as muons.

IBL OF Tracks which are categorized into the SR-Mu-IBL1 and SR-Trk-IBL1 regions are required to have a hit in the IBL OF. As discussed in Chapter 4, the IBL has a different set of electronics with respect to the other pixel layers. If the ToT range is saturated, hits will be tagged with an IBL

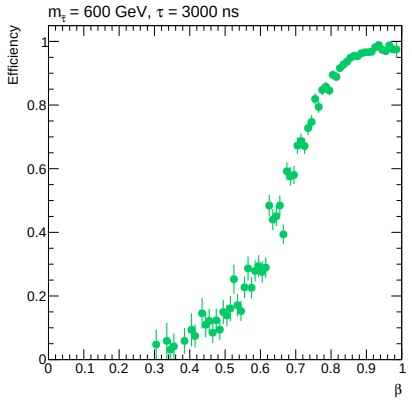

Figure 7.16: The efficiency for tracks to be reconstructed as a muon as a function of β. Tracks come from a sample of m = 600 GeV sleptons with a 3000 ns lifetime.[†]

overflow bit. The fraction of tracks in signal and data with a hit in the IBL overflow is shown in Figure 7.17b. The R-hadron signal tracks have a high probability of having a hit in the IBL overflow due to their high mass and therefore larger expected $\mathrm{d}E/\mathrm{d}x$.

$\mathrm{d}E/\mathrm{d}x$ BINS Tracks are also categorized into a `Low` or `High` channel according to their $\mathrm{d}E/\mathrm{d}x$ measurement. Figure 7.15a shows the $\mathrm{d}E/\mathrm{d}x$ distribution for various signals. Because the track $\mathrm{d}E/\mathrm{d}x$ depends on the mass of the sparticle, multiple ranges of $\mathrm{d}E/\mathrm{d}x$ are useful to maximize signal selection efficiency across a broad range of masses.

7.4 Data formats and cutflow

The primary ATLAS data format is the Analysis Object Data (AOD) format described in [137, 138]. In Run-2, AOD-based datasets were reduced in size using a derivation framework which produces

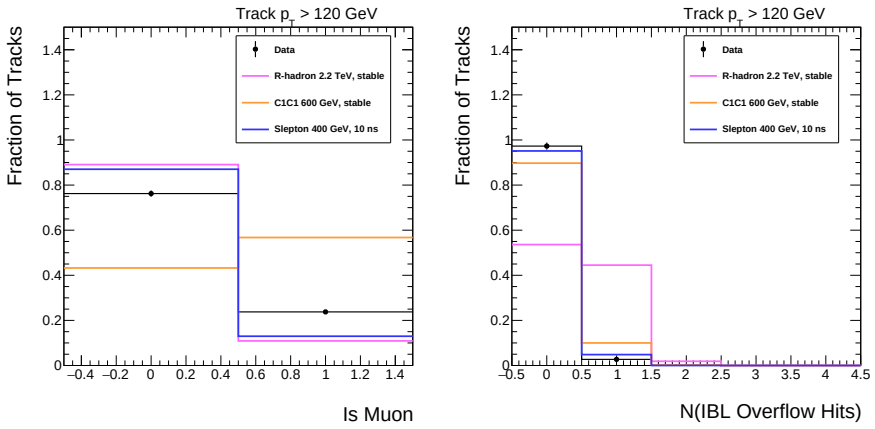

(a) N(muons) **(b)** N(IBL) overflow hits

Figure 7.17: The (a) fraction of tracks reconstructed as muons and (b) with a hit in the IBL overflow for the largest p_T track with p_T > 120 GeV, where all event-level selections are applied. Tracks in signal events must be matched to a sparticle. Data is from a portion of the 2018 run. The last bin includes all of the entries in overflow of the plot range.[†]

derived AOD samples, or DAODs. The data processing unique to this analysis begins with the so-called `SUSY6` DAOD format, which is designed to provide useful objects for several long-lived particle analysis teams.

Signal simulation samples in the `SUSY6` DAOD format are reduced to an ntuple-based format after applying the event and track selection. The data, however, is reduced in a two-step process. The first step converts the `SUSY6` DAOD to a `mini-xAOD` format and applies a loose event and track selection which is shown in Table 7.2.

The second step reduces the `mini-xAOD` to an ntuple-based format, and applies any remaining event and track selection. The cutflow for the second step is shown in Table 7.3. More details about the ATLAS data formats can be found in [137, 138].

The cutflow for events passing each selection is summarized in Tables 7.2 and 7.3 for the full

Selection	N(Events)	Eff.
SUSY6	4497855936	1
GRL	4371758464	0.972
Trigger	800674320	0.178
Track in PV	560531996	0.125
$p_T > 50$ GeV	144883491	0.032
Loose track isolation	50310121	0.011

Table 7.2: Cutflow for data events skimmed in the DAOD to `mini-xAOD` process. The loose track isolation requires that the Σp_T of tracks in a $\Delta R = 0.2$ cone around the candidate track is ≥ 20 GeV.[†]

Run-2 dataset and in Tables 7.4–7.6 for a m = 600 GeV stable chargino signal, a m = 2.2 TeV stable R-hadron signal, and a m = 400 TeV, τ =10 ns slepton signal.

Cut	N(Events)	Eff.	Rel. Eff.
mini-xAOD	50310121	1.000	1.000
Event Cleaning	50265190	0.999	0.999
Jet Cleaning	49666647	0.987	0.988
Primary Vertex	49666647	0.987	1.000
Offline $E_{\mathrm{T}}^{\mathrm{miss}}$	2696480	0.054	0.054
$\mathrm{d}E/\mathrm{d}x$ Used Hits	2451467	0.049	0.909
IBL/B-Layer Hits	2411925	0.048	0.984
Shared/Split Hits	2291630	0.046	0.950
SCT Hits	2187593	0.043	0.955
Track Isolation	1560198	0.031	0.713
$p_{\mathrm{T}} > 120$ GeV	390642	0.008	0.250
Momentum uncertainty	385291	0.008	0.986
$\lvert\eta\rvert < 1.8$	339695	0.007	0.882
$m_{\mathrm{T}} > 130$ GeV	86794	0.002	0.256
Electron veto	36462	0.001	0.420
Hadron veto	25440	0.001	0.698
Signal Region	**N(Events)**	**Fraction**	
SR-Mu-IBL0_Low	22049	0.867	
SR-Trk-IBL0_Low	3058	0.120	
SR-Mu-IBL0_High	22049	0.867	
SR-Trk-IBL0_High	3058	0.120	
SR-Mu-IBL1	286	0.011	
SR-Trk-IBL1	48	0.002	
SR-Inclusive_Low	25441	1.000	
SR-Inclusive_High	25441	1.000	

Table 7.3: Data cutflow for the SR-Inclusive signal region for all selection requirements except for the $\mathrm{d}E/\mathrm{d}x$ cut. The tracks in the SR-Inclusive signal region are then divided into the various channels, described in Section 7.3. Because no $\mathrm{d}E/\mathrm{d}x$ cut is applied, the track yields between the various Low and High regions are equivalent.[†]

Cut	N(Events)	Eff.	Rel. Eff.
Total	49.472	1.000	1.000
GRL	49.472	1.000	1.000
Event Cleaning	49.472	1.000	1.000
Jet Cleaning	49.170	0.994	0.994
Trigger	16.997	0.344	0.346
Primary Vertex	16.997	0.344	1.000
Offline $E_{\mathrm{T}}^{\mathrm{miss}}$	12.672	0.256	0.746
Track in PV	12.592	0.255	0.994
$p_{\mathrm{T}} > 50$ GeV	10.330	0.209	0.820
$\mathrm{d}E/\mathrm{d}x$ Used Hits	9.469	0.191	0.917
IBL/B-Layer Hits	9.418	0.190	0.995
Shared/Split Hits	8.886	0.180	0.944
SCT Hits	8.753	0.177	0.985
Track Isolation	7.125	0.144	0.814
$p_{\mathrm{T}} > 120$ GeV	7.068	0.143	0.992
Momentum uncertainty	6.703	0.135	0.948
$\lvert\eta\rvert < 1.8$	6.225	0.126	0.929
$m_{\mathrm{T}} > 130$ GeV	5.516	0.111	0.886
Electron veto	5.516	0.111	1.000
Hadron veto	5.516	0.111	1.000
$\mathrm{d}E/\mathrm{d}x > 1.8$ MeVg^{-1}cm^2	5.036	0.102	0.913
Signal Region	**N(Events)**	**Fraction**	
SR-Mu-IBL0_Low	0.162	0.032	
SR-Trk-IBL0_Low	0.408	0.081	
SR-Mu-IBL0_High	0.313	0.062	
SR-Trk-IBL0_High	1.698	0.337	
SR-Mu-IBL1	0.165	0.033	
SR-Trk-IBL1	2.290	0.455	
SR-Inclusive_Low	0.731	0.145	
SR-Inclusive_High	4.305	0.855	

Table 7.4: R-hadron signal event cutflow for the SR-Inclusive signal region for a stable signal with m_{χ} = 100 GeV. The tracks in the SR-Inclusive signal region are then divided into the various signal region channels, described in Section 7.3.[†]

Cut	N(Events)	Eff.	Rel. Eff.
Total	258.364	1.000	1.000
GRL	258.364	1.000	1.000
Event Cleaning	258.364	1.000	1.000
Jet Cleaning	255.914	0.991	0.991
Trigger	128.823	0.499	0.503
Primary Vertex	128.823	0.499	1.000
Offline $E_{\mathrm{T}}^{\mathrm{miss}}$	87.042	0.337	0.676
Track in PV	84.859	0.328	0.975
$p_{\mathrm{T}} > 50$ GeV	83.710	0.324	0.986
$\mathrm{d}E/\mathrm{d}x$ Used Hits	82.237	0.318	0.982
IBL/B-Layer Hits	82.193	0.318	0.999
Shared/Split Hits	81.784	0.317	0.995
SCT Hits	80.351	0.311	0.982
Track Isolation	79.401	0.307	0.988
$p_{\mathrm{T}} > 120$ GeV	78.927	0.305	0.994
Momentum uncertainty	78.314	0.303	0.992
$\lvert\eta\rvert < 1.8$	73.317	0.284	0.936
$m_{\mathrm{T}} > 130$ GeV	60.581	0.234	0.826
Electron veto	60.022	0.232	0.991
Hadron veto	58.820	0.228	0.980
$\mathrm{d}E/\mathrm{d}x > 1.8$ MeV$\mathrm{g}^{-1}\mathrm{cm}^2$	12.977	0.050	0.221

Signal Region	N(Events)	Fraction
SR-Mu-IBL0_Low	0.423	0.033
SR-Trk-IBL0_Low	5.889	0.454
SR-Mu-IBL0_High	0.108	0.008
SR-Trk-IBL0_High	4.725	0.364
SR-Mu-IBL1	0.012	0.001
SR-Trk-IBL1	1.819	0.140
SR-Inclusive_Low	6.791	0.523
SR-Inclusive_High	6.186	0.477

Table 7.5: Slepton signal event cutflow for the SR-Inclusive signal region with 400 GeV TeV sleptons with lifetime 10 ns. The tracks in the SR-Inclusive signal region are then divided into the various channels, described in Section 7.3.[†]

Cut	N(Events)	Eff.	Rel. Eff.
Total	2293.477	1.000	1.000
GRL	2293.477	1.000	1.000
Event Cleaning	2293.477	1.000	1.000
Jet Cleaning	2280.484	0.994	0.994
Trigger	481.429	0.210	0.211
Primary Vertex	481.429	0.210	1.000
Offline $E_{\mathrm{T}}^{\mathrm{miss}}$	330.357	0.144	0.686
Track in PV	329.945	0.144	0.999
$p_{\mathrm{T}} > 50$ GeV	319.115	0.139	0.967
$\mathrm{d}E/\mathrm{d}x$ Used Hits	309.647	0.135	0.970
IBL/B-Layer Hits	308.426	0.134	0.996
Shared/Split Hits	305.051	0.133	0.989
SCT Hits	302.184	0.132	0.991
Track Isolation	289.454	0.126	0.958
$p_{\mathrm{T}} > 120$ GeV	282.996	0.123	0.978
Momentum uncertainty	281.288	0.123	0.994
$\lvert\eta\rvert < 1.8$	247.263	0.108	0.879
$m_{\mathrm{T}} > 130$ GeV	225.914	0.099	0.914
Electron veto	225.914	0.099	1.000
Hadron veto	225.860	0.098	1.000
$\mathrm{d}E/\mathrm{d}x > 1.8$ MeVg^{-1}cm^2	98.766	0.043	0.437

Signal Region	N(Events)	Fraction
SR-Mu-IBL0_Low	25.403	0.257
SR-Trk-IBL0_Low	10.752	0.109
SR-Mu-IBL0_High	14.693	0.149
SR-Trk-IBL0_High	34.480	0.349
SR-Mu-IBL1	1.180	0.012
SR-Trk-IBL1	12.257	0.124
SR-Inclusive_Low	36.757	0.372
SR-Inclusive_High	62.009	0.628

Table 7.6: Chargino signal event cutflow for the SR-Inclusive signal region with stable charginos (superposition of $\tilde{\chi}_1^{\pm}\,\tilde{\chi}_1^0$ and $\tilde{\chi}_1^{\pm}\,\tilde{\chi}_1^{\mp}$) with mass 600 GeV. The tracks in the SR-Inclusive signal region are then divided into the various channels, described in Section 7.3.[†]

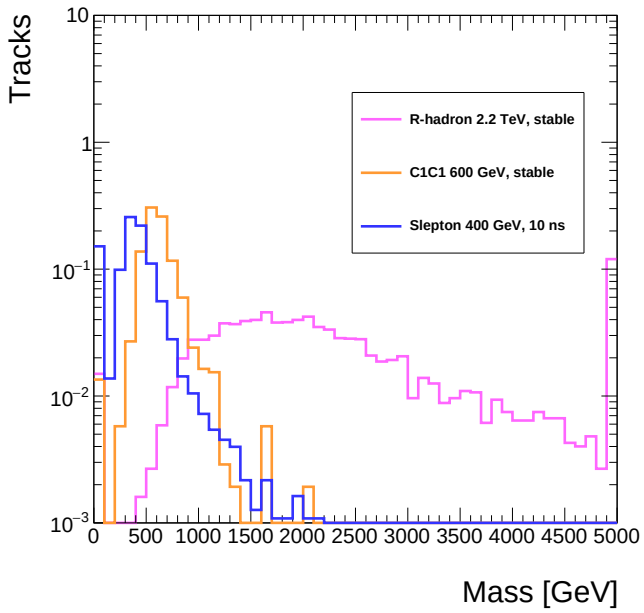

Figure 7.18: The mass distribution for tracks which pass all other track-level and event-level selections except for the ionization requirement. Tracks in signal events must be matched to a sparticle. The spike at 0 corresponds to tracks with $\mathrm{d}E/\mathrm{d}x$ < 0.975 which are considered MIP-like and assigned a pion mass in the mass calibration. The last bin includes all of the entries in overflow of the plot range.

As discussed in Chapter 6, using the $\mathrm{d}E/\mathrm{d}x$ to $\beta\gamma$ calibration and the track momentum measurement, a mass for each candidate track can be reconstructed. The reconstructed mass is shown in Figure 7.18 for several representative signal points with varying mass and lifetime to illustrate the expected mass resolution.

After tracks are categorized into the various signal regions, a series of sliding mass windows are applied to the candidate tracks as a final step to further improve the signal-to-background discrimination. The observed yields in these windows, which are defined in Table 7.7, are the numbers which

are used in the statistical analysis and limit setting described in Chapter 10. The mass windows are shown in Table 7.7.

To define the mass window bounds, the estimated SM background mass distribution later described in Chapter 8 and the signal mass distributions in the `SR-Inclusive_High` region were used to optimize the windows. For each signal sample, the lower and upper bounds of the mass window were iteratively scanned to maximize the $s/\sqrt{b}$ ratio (where s is the signal yield and b is the expected background) and have approximately 70% signal efficiency for tracks within the window. Samples across the various signal models which share a mass and lifetime were found to have compatible optimal mass windows. The optimization results were then used to define two windows for each target signal mass, one for $\tau \leq 1$ ns and one for $\tau > 1$ ns.

The window sizes increase as a function of mass due to the worsening mass resolution. This is largely driven by the track momentum resolution which degrades as a function of momentum due to the smaller sagitta. The expected background also decreases sharply as a function of mass which motivates the asymmetry of the window.

Target Mass [GeV]	Target Lifetime	m_{low}	m_{high}
100	All	120	200
200	Long	150	225
200	Short	120	225
300	Long	250	350
300	Short	200	350
400	Long	350	500
400	Short	300	500
450	Long	400	550
450	Short	350	600
500	Long	450	650
500	Short	400	700
550	Long	450	700
550	Short	400	800
600	Long	500	800
600	Short	450	900
650	Long	550	850
650	Short	500	1000
700	Long	550	950
700	Short	550	1100
800	Long	650	1150
800	Short	600	1200
900	Long	700	1250
900	Short	650	1400
1000	Long	800	1550
1000	Short	700	1850
1100	Long	900	1800
1200	Long	950	2100
1200	Short	800	2400
1300	Long	1000	2200
1400	Long	1100	2800
1400	Short	900	2900
1500	Long	1150	2900
1600	Long	1250	3400
1600	Short	1000	3450
1800	Long	1400	4250
1800	Short	1100	4000
2000	Long	1550	4650
2000	Short	1200	4600
2200	Long	1650	5900
2400	Long	1750	6300
2600	Long	1900	6500
2800	Long	2000	6700
3000	Long	2100	6700

Table 7.7: Mass window definitions for various target mass and lifetimes. The first column refers to the target mass, the second column refers to the target lifetime, and the last two columns define the bounds of the window. The short lifetime refers to lifetimes of 1 ns or less, while the long lifetime window applies for lifetimes of greater than 1 ns.[†]

8

Background Estimation

8.1 Sources of background

The signal region selects for high p_{T}, isolated tracks with large $\mathrm{d}E/\mathrm{d}x$. There are many sources of high p_{T} tracks in Standard Model processes which produce high p_{T} electrons, muons, and hadrons. The event selection requirements are not perfectly efficient at removing all SM-like activity. Therefore residual tracks which populate the tails of the selection variables, coupled with high fluctuations

in $\mathrm{d}E/\mathrm{d}x$ due to a limited number of pixel measurements, make up the background in the signal region. The rate of these processes is difficult to predict in simulation, so this analysis employs an entirely data-driven background estimation technique that is agnostic to the background composition.

8.2 Background estimation technique

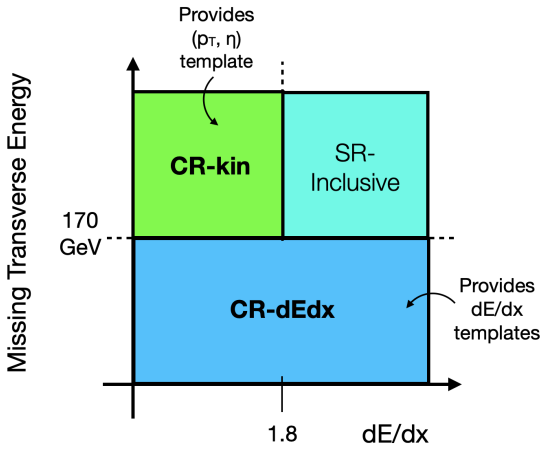

Figure 8.1: The two control regions, `CR-kin` and `CR-dEdx`, are defined by inverting the $\mathrm{d}E/\mathrm{d}x$ and $E_{\mathrm{T}}^{\mathrm{miss}}$ cuts of the inclusive signal region, respectively. p_{T} and η are sampled from the `CR-kin` region and $\mathrm{d}E/\mathrm{d}x$ is sampled from the `CR-dEdx` region to predict the background mass distribution in the signal region.

As discussed in Chapter 7, the final step of the analysis is applying a mass window to the reconstructed mass of the track candidates that pass the signal region requirements. The background estimation therefore must predict the expected background mass distribution of the track candidates in the signal region.

To predict the expected mass distribution, two control regions per signal region, `CR-kin` and `CR-dEdx`, are defined. The two dimensional $\mathrm{q}/p_{\mathrm{T}}$ versus η distribution from data in the `CR-kin`

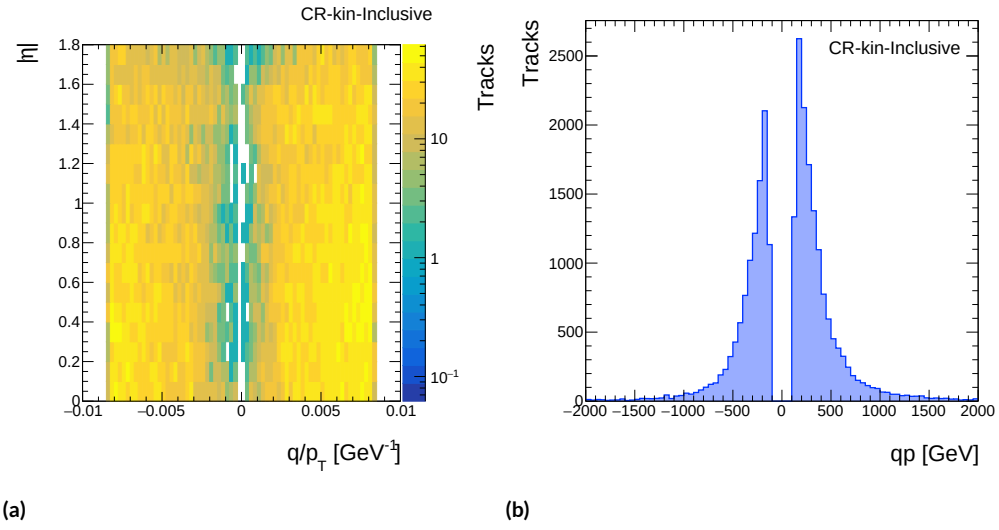

Figure 8.2: The (a) q/p_{T} versus $|\eta|$ distribution and (b) qp distribution in the `CR-kin` region. (a) forms the kinematic template, which is sampled along with the $\mathrm{d}E/\mathrm{d}x$ template to generate the estimated background mass distribution in the signal regions. Tracks are from the Run-2 dataset and share a common selection with the tracks in the `SR-Inclusive` region, with the exception of the $\mathrm{d}E/\mathrm{d}x$ requirement which is inverted.

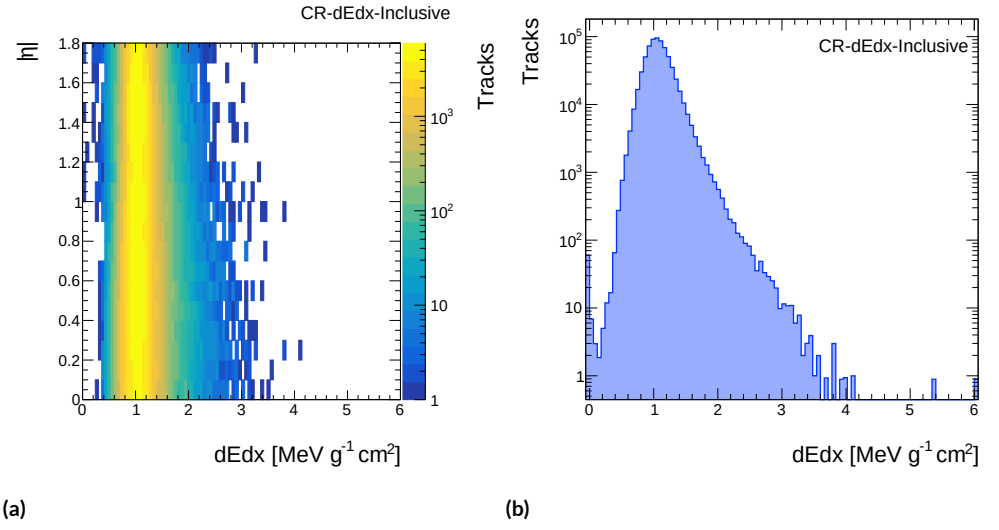

Figure 8.3: The (a) $\mathrm{d}E/\mathrm{d}x$ versus $|\eta|$ distribution and (b) $\mathrm{d}E/\mathrm{d}x$ distribution in the `CR-dEdx` region. (a) forms the $\mathrm{d}E/\mathrm{d}x$ template, which is sampled along with the kinematic template to generate the estimated background mass distribution in the signal regions. Tracks are from the Run-2 dataset and share a common selection with the tracks in the `SR-Inclusive` region, with the exception of the $E_{\mathrm{T}}^{\mathrm{miss}}$ requirement which is inverted.

forms the *kinematic template*. Similarly, the $\mathrm{d}E/\mathrm{d}x$ distribution from data in the `CR-dEdx` forms the $\mathrm{d}E/\mathrm{d}x$ *template*. Figure 8.1 is a cartoon of the region definitions. The `CR-kin` region shares all of the signal region requirements except for the $\mathrm{d}E/\mathrm{d}x$ requirement, which is inverted. Similarly the `CR-dEdx` region shares all of the signal region requirements except for the offline $E_{\mathrm{T}}^{\mathrm{miss}}$ requirement, which is inverted. Note that the signal regions which differ only by the $\mathrm{d}E/\mathrm{d}x$ requirement, i.e. the `Low` and `High` regions, share the same `CR-kin` region, which is defined to require $\mathrm{d}E/\mathrm{d}x$ $< 1.8\ \mathrm{MeV\ g^{-1}cm^2}$. For example, `SR-Mu-IBL0_Low` and `SR-Mu-IBL0_High` share a kinematic template.

The expected mass distribution is then generated by randomly sampling the kinematic and $\mathrm{d}E/\mathrm{d}x$ template to get a set of $\mathrm{q}/p_{\mathrm{T}}$, η, and $\mathrm{d}E/\mathrm{d}x$ values. Because $|p| = p_{\mathrm{T}}\cosh\eta$ and $\mathrm{d}E/\mathrm{d}x$ is a function of $\beta\gamma$, a toy mass value (using $m = p/\beta\gamma$) can be calculated with each set of sampled values.

These templates are sampled 10 million times to form the mass distribution for all regions except those defined to require $\mathrm{d}E/\mathrm{d}x > 2.4$ $[\mathrm{MeV\ g^{-1}cm^2}]$, in which case the templates are sampled 50 million times. The toy mass distribution is then scaled by a normalization factor to calculate the correct number of expected background events in the signal region. The factor r_{norm} is defined as

$$r_{\mathrm{norm}} = \frac{\text{\# toy tracks with } \mathrm{d}E/\mathrm{d}x < 1.8\ \mathrm{MeV\ g^{-1}cm^2}, m < 160\ \mathrm{GeV}}{\text{\# data tracks with } \mathrm{d}E/\mathrm{d}x < 1.8\ \mathrm{MeV\ g^{-1}cm^2}, m < 160\ \mathrm{GeV}} \tag{8.1}$$

The low mass region is used to normalize the toys because sparticle masses less than 160 GeV have been excluded for most of the relevant signal models and otherwise has little signal contamination

due to large background at low mass.

8.3 Special treatment of the IBL1 regions

The kinematic templates for IBL0 regions are populated across the full q/p_T and η range, as shown in Figure 8.4. The kinematic template for the IBL1 regions (Figure 8.5), conversely, are extremely sparse in statistics with large areas of q/p_T-η space without any tracks.

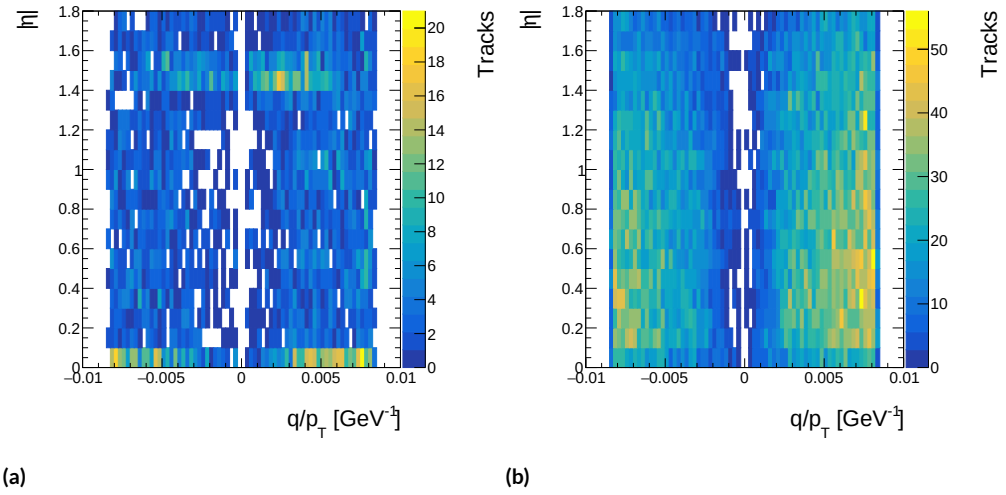

Figure 8.4: The kinematic templates for the IBL0 signal regions (which include tracks without a hit in the IBL OF), for (a) Trk and (b) Mu. The excess of tracks at $|\eta| < 0.1$ for the Trk region is due to gaps in muon detector coverage, which migrate tracks from the Mu category to the Trk category.

To avoid large statistical uncertainties on the IBL1 kinematic templates, the q/p_T and η samples are taken from a reweighted version of the kinematic template from IBL0.

Before reweighting, the p_T distributions of the IBL1 and IBL0 regions are similar, but the IBL1 tracks are concentrated at high $|\eta|$ while the IBL0 tracks gradually fall as a function of $|\eta|$ (see Fig-

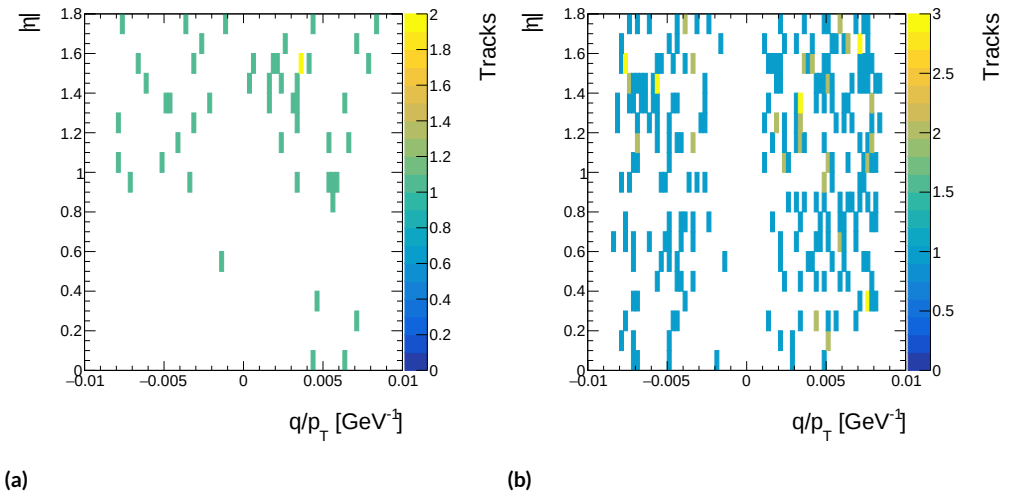

Figure 8.5: The kinematic templates for the `IBL1` signal regions (which include tracks with a hit in the IBL OF), for `Trk` (a) and `Mu` (b). Due to the low probability of having a track with a hit in the IBL OF, these templates have fewer tracks than the `IBL0` templates.

ure 8.6). The difference in η distributions can be attributed to a combination of increased path length x of the tracks through silicon as a function of η and η-dependent radiation damage, discussed in Chapter 3.0.5. As the silicon path length increases, the MPV of the $\mathrm{d}E/\mathrm{d}x$ distribution increases and the width of the distribution decreases. Due to the differences in the η distributions for `IBL1` and `IBL0`, a set of weights are generated to reweight the `IBL0` η distribution to match the `IBL1` η distribution. These weights are shown in Figure 8.7.

8.4 η-sliced $\mathrm{d}E/\mathrm{d}x$ template

As discussed in Chapter 6.3, there are significant correlations between $\mathrm{d}E/\mathrm{d}x$ and η. Although corrections are applied to minimize the $\mathrm{d}E/\mathrm{d}x$ dependence on η, there is still a significant

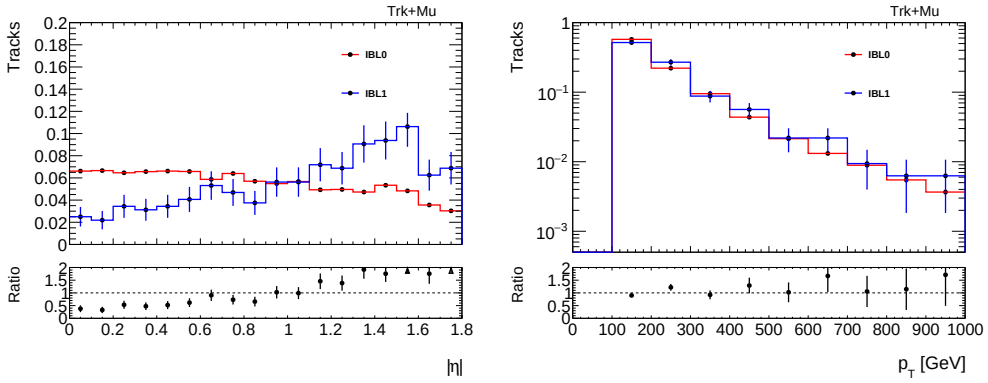

(a) η **(b)** p_{T}

Figure 8.6: A comparison of the p_{T} and η distributions for `IBL0` and `IBL1` regions. The p_{T} distributions for the two track types are similar, but the η distributions differ significantly. The η distribution of `IBL1` tracks has a higher proportion of tracks at high η. This is due to the increase in the path length of a particle through the silicon at high η, which increases the probability of having a hit in the IBL overflow.

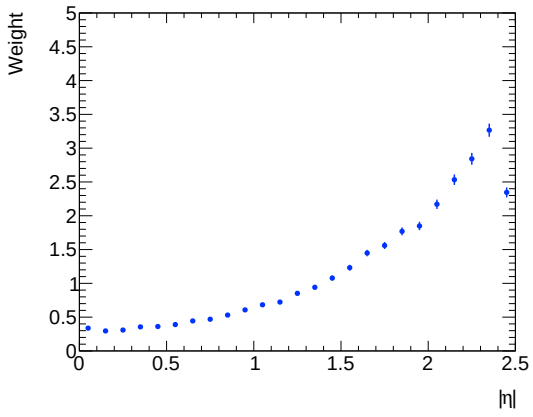

Figure 8.7: The η dependent weights used to reweight the `IBL0` kinematic template. The size of the weights reflects the difference in the η distributions between `IBL1` and `IBL0` tracks.

shape difference between $\mathrm{d}E/\mathrm{d}x$ distributions at central and forward η, as shown in Figure 8.8. The $\mathrm{d}E/\mathrm{d}x$ distribution for tracks at small η has a longer tail compared to that for tracks at large η in part due to the $\mathrm{d}E/\mathrm{d}x$ dependence on silicon path length. To account for this correlation, the $\mathrm{d}E/\mathrm{d}x$ template from the control region is sliced in η to form eight separate templates for the nominal and validation regions. The η binning is chosen have bin edges $[0, 0.1, 0.5, 0.7, 0.9, 1.1, 1.3, 1.5, 1.8, 2.1, 2.5]$ for all templates except those for the `IBL1` regions, which have bin edges $[0, 0.1, 1.0, 1.5, 1.8, 2.5]$. The bin edges define roughly equal bins in η for the non-`IBL1` regions, with the exception of the $[0, 0.1]$ bin which is chosen due to the gap in the muon spectrometer coverage at $|\eta| < 0.1$. This gap causes an excess of tracks in the `Trk` regions at $|\eta| < 0.1$ due to low muon identification efficiency. The `IBL1` regions have larger bins due to the fewer statistics in these regions. Any bias due to this arbitrary choice is evaluated and taken as a systematic uncertainty, as described in Chapter 9.

8.5 $E_{\mathrm{T}}^{\mathrm{miss}}$ Trigger Reweighting

The $\mathrm{d}E/\mathrm{d}x$ control regions differ from the signal regions by an inverted $E_{\mathrm{T}}^{\mathrm{miss}}$ cut. Because there is no minimum requirement on the offline $E_{\mathrm{T}}^{\mathrm{miss}}$ from these regions, the number of events per fb^{-1} in the $\mathrm{d}E/\mathrm{d}x$ control region depends on the $E_{\mathrm{T}}^{\mathrm{miss}}$ trigger threshold.

In Run-2 the $E_{\mathrm{T}}^{\mathrm{miss}}$ trigger algorithm and threshold changed several times, as shown in Table 8.1. As a result, the ratio R of events with $E_{\mathrm{T}}^{\mathrm{miss}} < 170$ GeV to events with $E_{\mathrm{T}}^{\mathrm{miss}} > 170$ is nonuniform across Run-2. To ensure that the data taking periods with the lowest trigger threshold do not bias

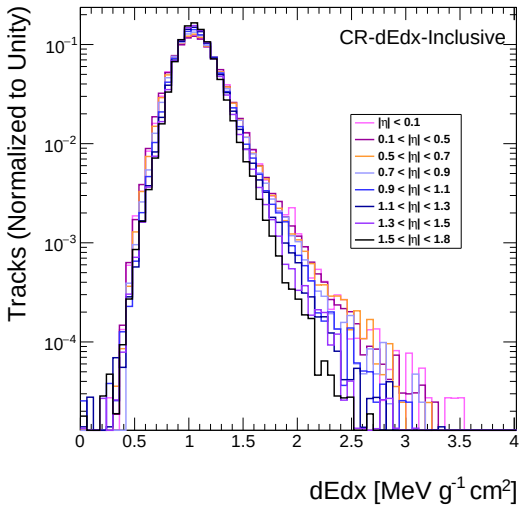

Figure 8.8: The various η-binned $\mathrm{d}E/\mathrm{d}x$ templates in `CR-kin`. The width of the $\mathrm{d}E/\mathrm{d}x$ distribution narrows with increasing $|\eta|$. This is likely due to a combination of varying radiation dose across η, as well as the intrinsic $\mathrm{d}E/\mathrm{d}x$ dependence on x.

the final result due to larger statistics, a weight for each period with a constant trigger is derived and assigned to the associated events in the $\mathrm{d}E/\mathrm{d}x$ control regions.

The weight for period i is defined as

$$w_i = R_{i_0}/R_i, \tag{8.2}$$

where i_0 is defined to be the period with the largest integrated luminosity.

The weights for `CR-dEdx` were calculated by comparing the ratio of events in the `CR-dEdx` region and the `SR-Inclusive` region (without the $\mathrm{d}E/\mathrm{d}x$ cut applied).

The weight values are shown in the last column of Table 8.1.

Period	Lumi [fb^{-1}]	Trigger	Event Weight CR-LowPt-dEdx CR-HiEta-dEdx	Event Weight CR-dEdx
2015	3.2	HLT_xe70_mht	0.53	0.94
2016 A-D3	6.1	HLT_xe90_mht_L1XE50	0.60	0.89
2016 D4-F1	5.4	HLT_xe100_mht_L1XE50	0.68	1.00
2016 F2-L	21.4	HLT_xe110_mht_L1XE50	0.80	0.93
2017 B-D5	12.8	HLT_xe110_pufit_L1XE55	1.04	1.00
2017 D6-N	31.5	HLT_xe110_pufit_L1XE50	0.85	0.99
2018 B-C5	6.4	HLT_xe110_pufit_xe70_L1XE50	1.00	0.99
2018 C5-R	52.0	HLT_xe110_pufit_xe65_L1XE50	1.00	1.00

Table 8.1: Event weights for the dE/dx control region due to changing trigger thresholds.[†]

8.6 Validation of the background estimation

To validate the background estimation, regions distinct from the signal region in phase space are defined as validation regions (see Figure 8.9). The yield and mass shape in each validation region is predicted using the background estimation procedure. The agreement of data with the prediction serves as a check of the background esimation.

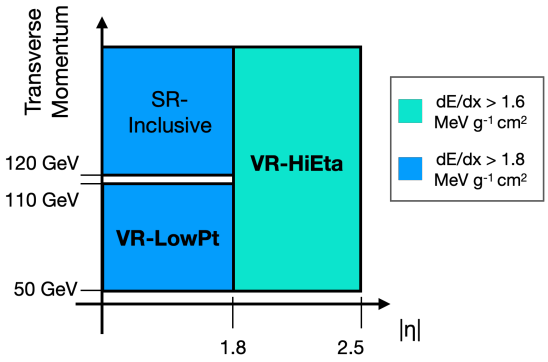

Figure 8.9: The validation regions `VR-LowPt` and `VR-HiEta` are defined by lowering the p_{T} cut and changing the $|\eta|$ cuts with respect to the signal regions. The $\mathrm{d}E/\mathrm{d}x$ cut is also lowered for the `VR-HiEta` region to 1.6 $\mathrm{MeV\ g^{-1}cm^{2}}$ due to the different $\mathrm{d}E/\mathrm{d}x$ tail shape in the high η region.

VR-LowPt is defined to have the same requirements as the signal region except with a lower transverse momentum (50 GeV< p_{T} < 110 GeV) track requirement. VR-HiEta is defined with a loosened transverse momentum requirement (p_{T} > 50 GeV), inverted η requirement (1.8 < $|\eta|$ < 2.5) and lower $\mathrm{d}E/\mathrm{d}x$ cut (1.6 $\mathrm{MeV\ g^{-1}cm^2}$) with respect to the signal region definition. Note that despite the loosened p_{T} cut, the VR-HiEta region was designed to test the background estimation for tracks with a comparable *momentum* range to tracks in the nominal region. For a track with p_{T} =50 GeVand η = 1.8 , the corresponding momentum is around 155 GeV. The momentum distribution of tracks in the CR-kin and CR-HiEta-kin regions, where CR-HiEta-kin provides the (q/p_{T}, η) template for the VR-HiEta region, is shown in Figure 8.10. The $\mathrm{d}E/\mathrm{d}x$ cut in this region, which has a narrow $\mathrm{d}E/\mathrm{d}x$ distribution due to the high η requirement, was chosen to probe a similar fraction of the $\mathrm{d}E/\mathrm{d}x$ tail as the SR and VR-LowPt regions.

The inclusive validation regions are subdivided based on the $\mathrm{d}E/\mathrm{d}x$ measurement, IBL overflow information, and muon information to parallel the structure of the signal regions. The subdivision for the validation regions is the same as for the signal regions (defined in Table 7.1), with the exception that the VR-HiEta region is not subdivided into IBL0_Low and IBL0_High but is instead agnostic to the $\mathrm{d}E/\mathrm{d}x$ range above 1.6 $\mathrm{MeV\ g^{-1}cm^2}$.

The control regions used to predict the background in the validation regions are defined similarly to the control regions for the signal region. The control regions share all of the selection requirements of the corresponding validation regions, with the exception of the $\mathrm{d}E/\mathrm{d}x$ cut which is inverted for the CR-LowPt-kin and CR-HiEta-kin regions, as well as the $E_{\mathrm{T}}^{\mathrm{miss}}$ cut which is inverted for the CR-LowPt-dEdx and CR-HiEta-dEdx regions. $E_{\mathrm{T}}^{\mathrm{miss}}$ trigger reweighting (see Section 8.5) is

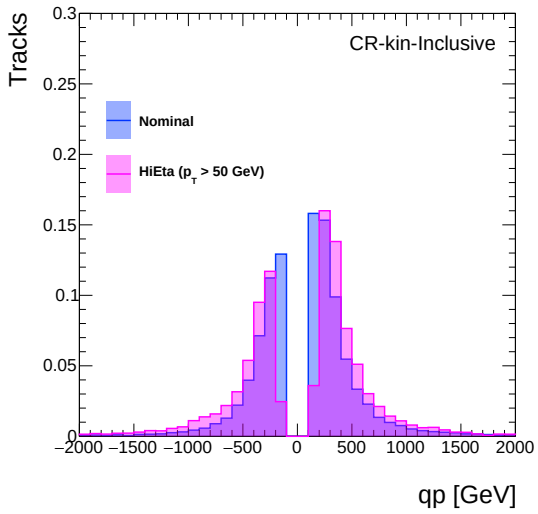

Figure 8.10: The qp distributions for tracks in the `CR-kin` (also referred to as the nominal control region) and `CR-HiEta-kin` regions. The momentum distribution for tracks in `CR-HiEta-kin` is higher than for tracks in `CR-kin`.

also applied for the control regions used to predict the validation region yields. The weights for the `CR-LowPt-dEdx` and `CR-HiEta-dEdx` regions are calculated in a similar procedure as for the nominal `CR-dEdx` region; the ratio of events in the `CR-LowPt-dEdx` region and the `VR-LowPt` region is used as the weight.

The agreement between the validation region predicted and observed total yields is shown in Figure 8.11. Agreement within 1-2 sigma of the total uncertainty is observed.

Note that without the full set of systematic uncertainties, the predicted yield in the `VR-LowPt-Trk-IBL0_Low` region is significantly overestimated relative to the observed yield (see Figure 8.14a). This disagreement has been studied and is included as an empirical systematic uncertainty on the background estimate. Chapter 9 describes this uncertainty as well as the other

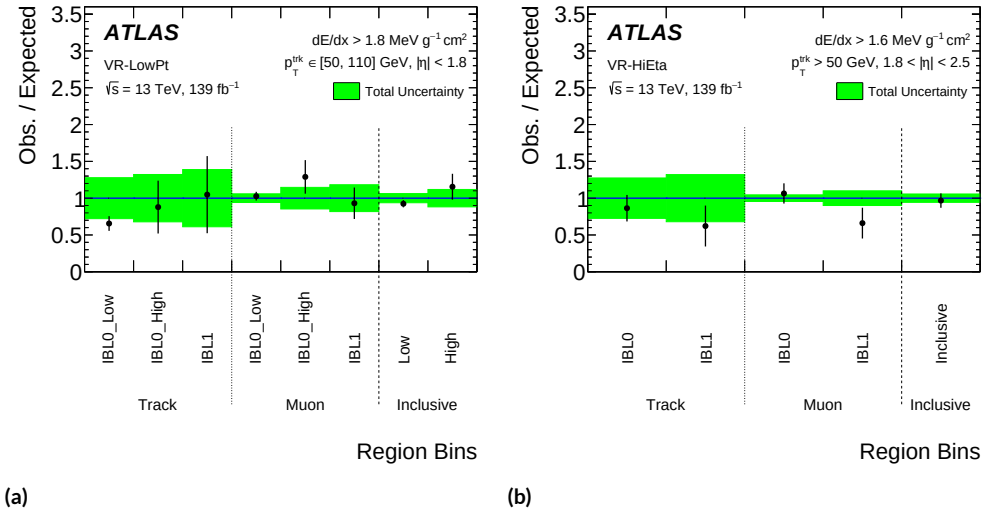

Figure 8.11: The overall predicted and observed yield agreement in the (a) `LowPt` validation regions and the (b) `HiEta` validation regions [11].

uncertainties on the background in further detail.

The expected and observed mass distributions for each of the validation regions are shown in Figures ??–8.16. The mass shape prediction agrees well with data in each of these regions. As expected, the `VR-LowPt` tracks are distributed at low masses, and the `VR-HiEta` tracks are distributed at higher masses.

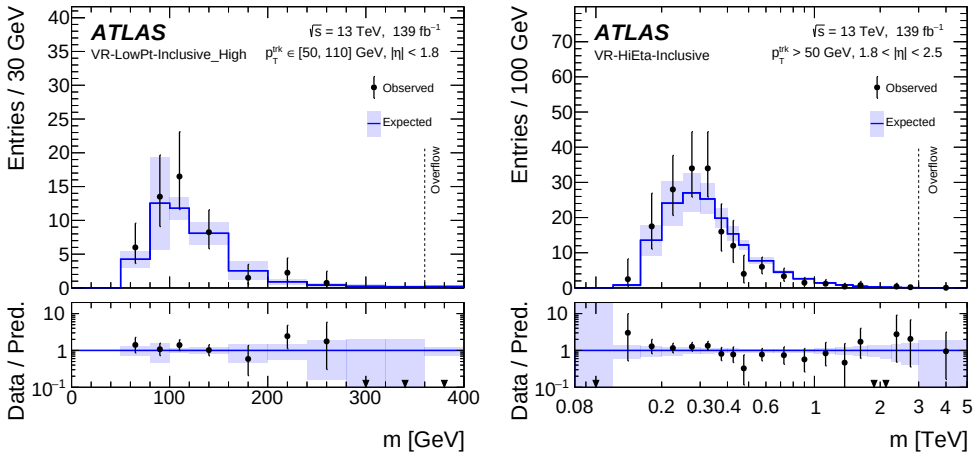

(a) `VR-LowPt-Inclusive_High` **(b)** `VR-HiEta-Inclusive`

Figure 8.12: The predicted and observed mass distributions in the (a) `VR-LowPt-Inclusive_High` and the (b) `VR-HiEta-Inclusive` regions. The total uncertainty is shown as a purple band [11].

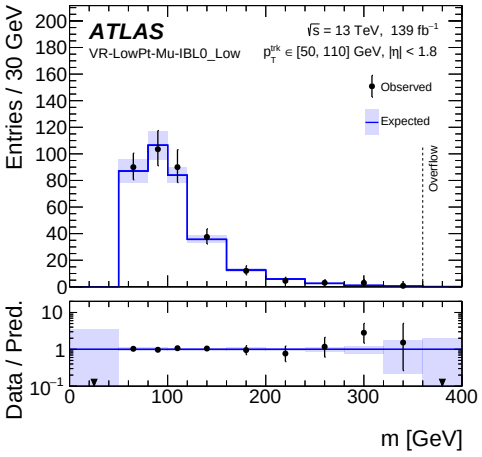

(a) `VR-LowPt-Mu-IBL0_Low`

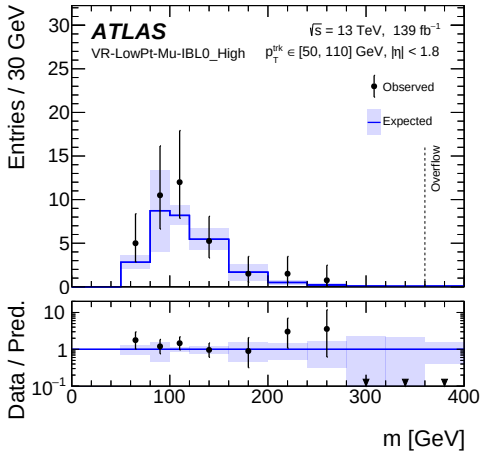

(b) `VR-LowPt-Mu-IBL0_High`

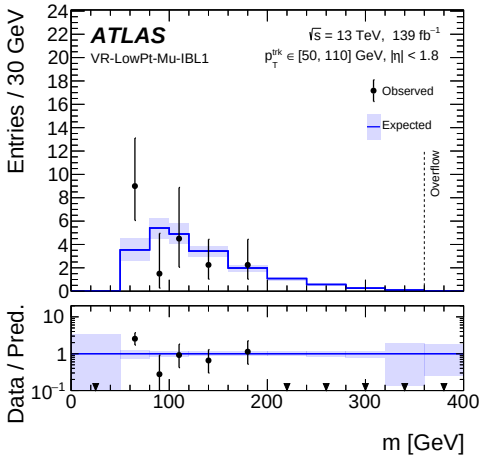

(c) `VR-LowPt-Mu-IBL1`

Figure 8.13: The predicted and observed mass distributions in the (a) `VR-LowPt-Mu-IBL0_Low` region, the (b) `VR-LowPt-Mu-IBL0_High`, and the (c) `VR-LowPt-Mu-IBL1` validation regions. The total uncertainty is shown as a purple band [11].

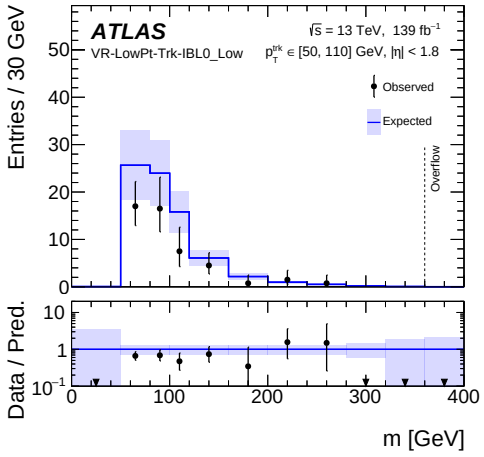

(a) `VR-LowPt-Trk-IBL0_Low`

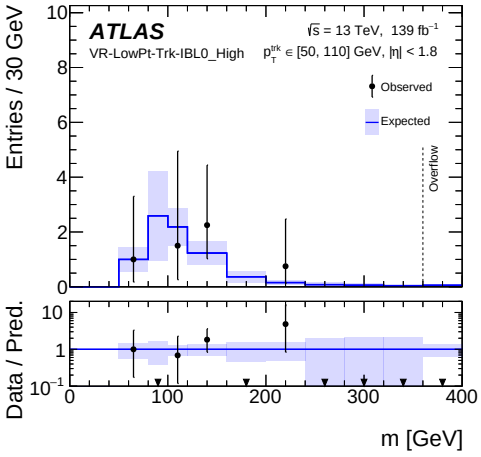

(b) `VR-LowPt-Trk-IBL0_High`

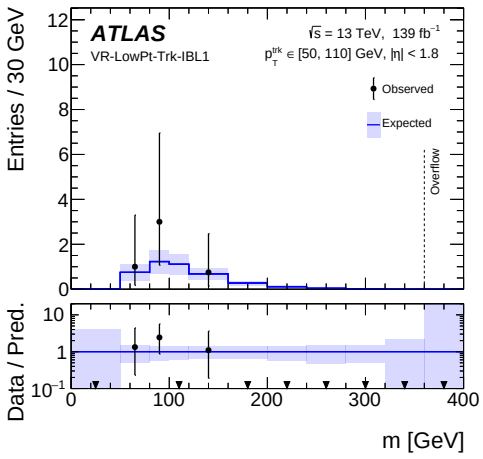

(c) `VR-LowPt-Trk-IBL1`

Figure 8.14: The predicted and observed mass distributions in the (a) `VR-LowPt-Trk-IBL0_Low` region, the (b) `VR-LowPt-Trk-IBL0_High`, and the (c) `VR-LowPt-Trk-IBL1` validation regions. The total uncertainty is shown as a purple band [11].

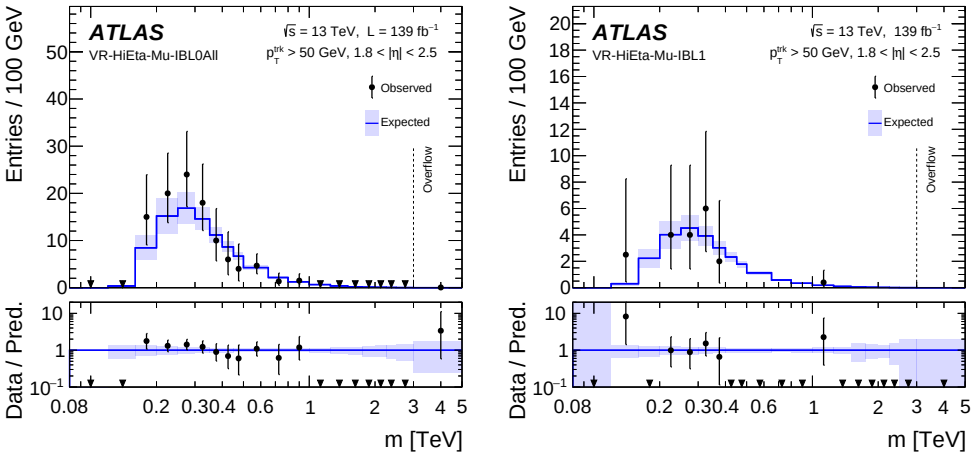

(a) `VR-HiEta-Mu-IBL0` **(b)** `VR-HiEta-Mu-IBL1`

Figure 8.15: The predicted and observed mass distributions in the (a) `VR-HiEta-Mu-IBL0` region and the (b) `VR-HiEta-Mu-IBL1` validation regions. The total uncertainty is shown as a purple band [11].

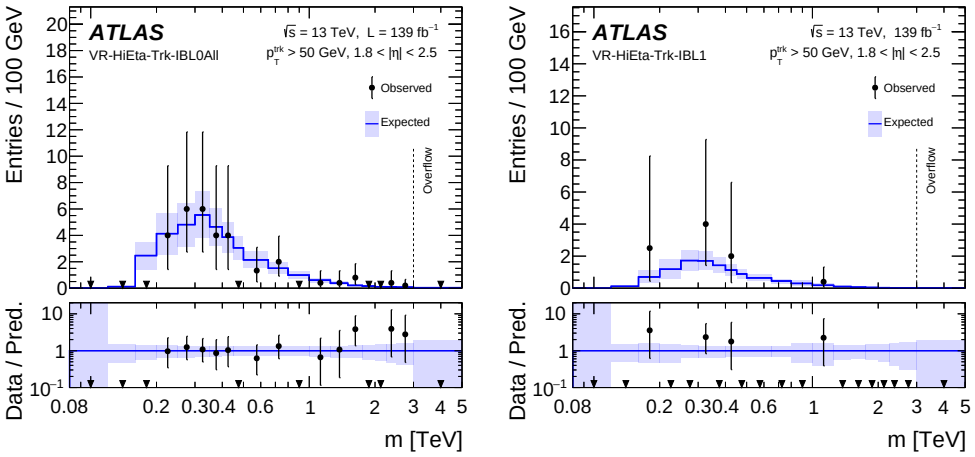

(a) `VR-HiEta-Trk-IBL0` **(b)** `VR-HiEta-Trk-IBL1`

Figure 8.16: The predicted and observed mass distributions in the (a) `VR-HiEta-Trk-IBL0` region and the (b) `VR-HiEta-Trk-IBL1` validation regions. The total uncertainty is shown as a purple band [11].

9

Systematic Uncertainties

9.1 Uncertainties on the background estimation

The following sections describe the uncertainties associated to the background estimate. All of the uncertainties, with the exception of the normalization uncertainty and the $\mathrm{d}E/\mathrm{d}x$ scale uncertainty, are calculated as a function of reconstructed track mass.

9.1.1 Background template correlations

The background estimation technique discussed in Chapter 8 relies on the assumption that $\mathrm{d}E/\mathrm{d}x$ and p_{T} for background tracks are uncorrelated. In order to evaluate this assumption, a fake signal region is defined at high $\mathrm{d}E/\mathrm{d}x$ in the `CR-dEdx` region, which has an inverted $E_{\mathrm{T}}^{\mathrm{miss}}$ cut with respect to `SR-Inclusive`. The background in this fake signal region is estimated using the usual background estimation technique, except the kinematic template is taken from `CR-dEdx` instead of the `CR-kin` region. Because the kinematic template, the $\mathrm{d}E/\mathrm{d}x$ template, and the fake signal region are all taken from the `CR-dEdx` region, any difference in the predicted and observed mass distribution in the fake signal region must be due to unaccounted-for correlations between $\mathrm{d}E/\mathrm{d}x$ and momentum.

The predicted and observed mass distributions for tracks with $\mathrm{d}E/\mathrm{d}x$ between 1.8 and 2.4 and greater than 2.4 $\mathrm{MeV\,g^{-1}cm^2}$ are shown in Figure 9.1. The predicted and observed distributions diverge at high mass. This discrepancy is taken as a systematic on the background estimation and is the largest uncertainty on the background estimation at high masses. To avoid unphysical fluctuations due to limited statistics, the value of the uncertainty applied to regions requiring $\mathrm{d}E/\mathrm{d}x > 2.4$ $\mathrm{MeV\,g^{-1}cm^2}$ is smoothed in each mass window using a running average across the adjacent mass windows. The uncertainty applied to the mass window n is the average of the raw uncertainty in the $n-1$, n, and $n+1$ windows. To further minimize the statistical uncertainty, the mass window definition used to calculate the systematic uncertainties always corresponds to the short lifetime definition (which is larger than the corresponding long lifetime window). The final values applied in

each window are shown later in Figures 9.8–9.15.

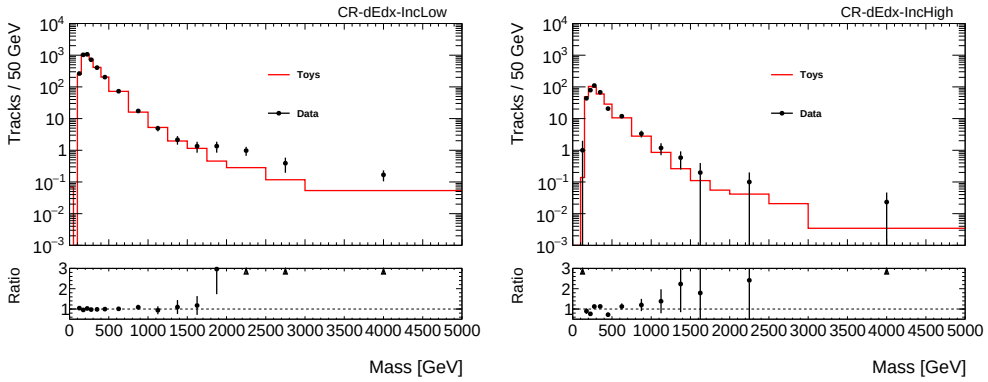

(a) `Fake Inclusive_Low` **(b)** `Fake Inclusive_High`

Figure 9.1: The predicted and observed mass distributions for tracks in the fake signal region with $E_{\mathrm{T}}^{\mathrm{miss}}$ < 170 GeV and (a) 2.4 > $\mathrm{d}E/\mathrm{d}x$ > 1.8 $\mathrm{MeV\,g^{-1}cm^2}$ and (b) $\mathrm{d}E/\mathrm{d}x$ > 2.4 $\mathrm{MeV\,g^{-1}cm^2}$. The disagreement in the distributions is attributed to unaccounted correlations between the $\mathrm{d}E/\mathrm{d}x$ and momentum measurements for background tracks.[†]

9.1.2 Uncertainties on the $\mathrm{d}E/\mathrm{d}x$ and kinematic templates

The $(\mathrm{q}/p_{\mathrm{T}}, \eta)$ and $\mathrm{d}E/\mathrm{d}x$ templates are derived from regions which have an inverted $\mathrm{d}E/\mathrm{d}x$ and $E_{\mathrm{T}}^{\mathrm{miss}}$ requirement, respectively. To evaluate any potential bias which might come from taking the templates from these regions, a set of p_{T} dependent weights and a set of $\mathrm{d}E/\mathrm{d}x$ dependent weights are calculated.

To derive the $\mathrm{d}E/\mathrm{d}x$ dependent weights, the $\mathrm{d}E/\mathrm{d}x$ distribution for tracks from events at low and high $E_{\mathrm{T}}^{\mathrm{miss}}$ are compared using tracks in the `LowPt` region. The ratio of these distributions is used to derive weights which are then applied to the $\mathrm{d}E/\mathrm{d}x$ template, where the weights are defined as

$\mathrm{d}E/\mathrm{d}x$ range [$\mathrm{MeV\,g^{-1}cm^2}$]	Weight
0–0.6	0.954 ± 0.074
0.6–1.2	0.997 ± 0.006
1.2–1.5	1.009 ± 0.012
1.5–1.8	1.022 ± 0.030
1.8–2.4	0.950 ± 0.057
2.4–3.0	1.250 ± 0.247
3.0–6.0	0.951 ± 0.409

p_{T} range [GeV]	Weight
50–100	1.000 ± 0.004
100–200	1.000 ± 0.002
200–300	1.000 ± 0.003
300–400	1.000 ± 0.007
400–500	1.001 ± 0.013
500–1000	1.002 ± 0.015
1000–1500	1.008 ± 0.049
1500–2500	1.008 ± 0.073

Table 9.1: The weights used to reweight the $\mathrm{d}E/\mathrm{d}x$ and p_{T} distributions to estimate the bias from taking the $\mathrm{d}E/\mathrm{d}x$ and kinematic templates from regions with an inverted $\mathrm{d}E/\mathrm{d}x$ and $E_{\mathrm{T}}^{\mathrm{miss}}$ requirement with respect to the signal region.

$$w(\mathrm{d}E/\mathrm{d}x) = \frac{\mathrm{d}E/\mathrm{d}x(E_{\mathrm{T}}^{\mathrm{miss}} > 170\ \mathrm{GeV})}{\mathrm{d}E/\mathrm{d}x(E_{\mathrm{T}}^{\mathrm{miss}} < 170\ \mathrm{GeV})}. \tag{9.1}$$

An alternative mass distribution is generated using the reweighted $\mathrm{d}E/\mathrm{d}x$ template and compared to the original mass distribution. The difference in these distributions is taken as the uncertainty on the $\mathrm{d}E/\mathrm{d}x$ template.

To derive the p_{T} dependent weights, a similar procedure is followed, except the weights are instead defined as

$$w(p_{\mathrm{T}}) = \frac{p_{\mathrm{T}}(\text{all tracks})}{p_{\mathrm{T}}(\text{tracks with } \mathrm{d}E/\mathrm{d}x < 1.8\ \mathrm{MeV\,g^{-1}cm^2})}. \tag{9.2}$$

These weights are observed to be extremely close to unity since the bulk of the $\mathrm{d}E/\mathrm{d}x$ distribution is below $1.8\ \mathrm{MeV\,g^{-1}cm^2}$.

These weights, shown in Table 9.1, are both calculated without using IBL overflow information or muon information (to reduce statistical uncertainty). They are consistent with unity and are not implemented in the final statistical analysis. The $\mathrm{d}E/\mathrm{d}x$ tail systematic, described in the next

section, supersedes the $\mathrm{d}E/\mathrm{d}x$ dependent weights.

9.1.3 $\mathrm{d}E/\mathrm{d}x$ tail dependence on $E_{\mathrm{T}}^{\mathrm{miss}}$

For each validation region, the yield and mass distribution of events passing the validation region selection is predicted using the data-driven background estimation described in Chapter 8. The agreement between the prediction and the observed yield and mass distribution serves as a check on the background estimation procedure.

The observed and predicted yields and mass distributions in the validation regions are shown in Chapter 8.6. In one of the validation regions, `VR-LowPt-Trk-IBL0_Low`, the predicted and observed yield in the region shows a significant disagreement. This disagreement is taken as a systematic uncertainty.

This discrepancy was studied and can be attributed to a subtle but significant dependence of the $\mathrm{d}E/\mathrm{d}x$ tail on $E_{\mathrm{T}}^{\mathrm{miss}}$, therefore biasing the $\mathrm{d}E/\mathrm{d}x$ template from `CR-`$\mathrm{d}E/\mathrm{d}x$. To illustrate this, the double ratio of the $\mathrm{d}E/\mathrm{d}x$ tail fraction as a function of a $E_{\mathrm{T}}^{\mathrm{miss}}$ cut in the `LowPt-Trk-IBL0` region is shown as the black points in Figure 9.2. The double ratio DR is defined as

$$DR(E_{\mathrm{T}}^{\mathrm{miss}} > X) = \frac{\text{\% tracks with } \mathrm{d}E/\mathrm{d}x > 1.8\ \mathrm{MeV\,g^{-1}cm^2} \text{and } E_{\mathrm{T}}^{\mathrm{miss}} > X}{\text{\% tracks with } \mathrm{d}E/\mathrm{d}x > 1.8\ \mathrm{MeV\,g^{-1}cm^2} \text{and } E_{\mathrm{T}}^{\mathrm{miss}} < 170\ \mathrm{GeV}}, \qquad (9.3)$$

where X is the $E_{\mathrm{T}}^{\mathrm{miss}}$ threshold specified in the x-axis of the plot.

The dependence of this ratio on $E_{\mathrm{T}}^{\mathrm{miss}}$ reflects a non-negligible correlation which is not captured

by the inclusive $\mathrm{d}E/\mathrm{d}x$ template uncertainty. To check the assumption that the discrepancy can be measured in the `LowPt` regions and extrapolated to the signal regions defined at high p_{T}, the DR is also plotted for two different p_{T} slices in Figure 9.2. No significant p_{T} dependence is observed.

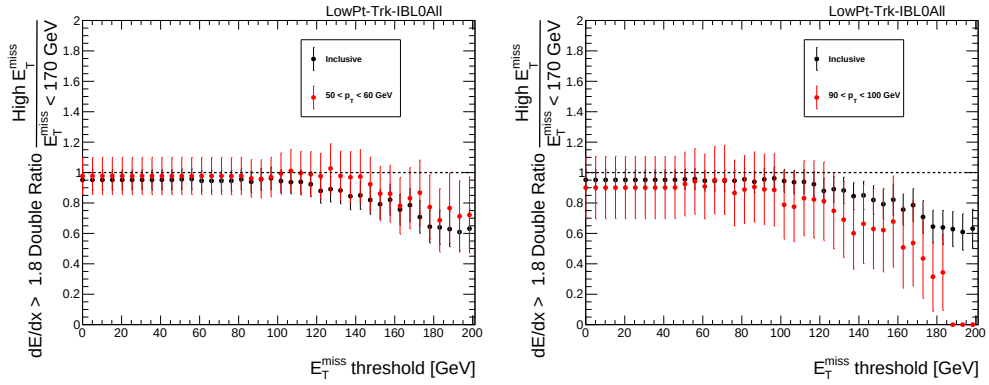

(a) 50 < p_{T} < 60 GeV **(b)** 90 < p_{T} < 100 GeV

Figure 9.2: The double ratio of the $\mathrm{d}E/\mathrm{d}x$ tail fraction as a function of $E_{\mathrm{T}}^{\mathrm{miss}}$. The numerator of the ratio is the fraction of tracks with $\mathrm{d}E/\mathrm{d}x$ > 1.8 $\mathrm{MeV\,g^{-1}cm^2}$ that also pass the $E_{\mathrm{T}}^{\mathrm{miss}}$ cut specified on the x-axis. The denominator is the same fraction of tracks which have $E_{\mathrm{T}}^{\mathrm{miss}}$ < 170 GeV. Tracks are taken from the `CR-`$\mathrm{d}E/\mathrm{d}x$`-LowPt-Trk-IBL0` and `VR-LowPt-Trk-IBL0` regions. (a) shows the ratio for all tracks passing these requirements and for tracks restricted to a p_{T} range of [50, 60] GeV. (b) shows the ratio for tracks restricted to a p_{T} range of [90, 100] GeV. No significant p_{T} dependence is observed.

To calculate the size of the uncertainty, a product of likelihoods is constructed

$$L_j(R_j) = \prod_i \mathrm{Poisson}(n_i | R_j \times b_i), \tag{9.4}$$

where n_i is the observed yield in the validation region i and b_i is the predicted yield in validation region i. The product is computed over all of the regions associated to j, where $j \in \{\mathtt{Trk}, \mathtt{Mu}, \mathtt{Inc}\}$. The value of the likelihood L_j is maximized in a fit scanning R_j.

The choice of j is motivated by the dependence of the $\mathrm{d}E/\mathrm{d}x$ distribution on track quality. The

fitted R value is calculated separately for the `Trk` and `Mu` validation region channels (both `LowPt` and `HiEta`) and applied as a systematic uncertainty to the relevant exclusion signal region channels. For the discovery region channels, one R_{Inc} value is calculated and applied to both channels. The resulting R values from the likelihood fit are:

- $R_{\text{Mu}} = 0.73$
- $R_{\text{Trk}} = 1.03$
- $R_{\text{Inc}} = 0.95$

These values are translated to a 27% uncertainty on `Mu` channels, a 3% uncertainty on `Trk` channels, and a 5% uncertainty on `Inclusive` channels.

9.1.4 Normalization

The statistical uncertainty on the normalization factor used in the background estimate is taken as a flat systematic as a function of mass. The uncertainty is determined by the number of tracks which fail the high $\mathrm{d}E/\mathrm{d}x$ requirement and have mass < 160 GeV in the `CR-dEdx` regions. The size of this uncertainty ranges from ∼1-20%, with the largest uncertainty associated to the `IBL1` regions.

9.1.5 IBL overflow reweighting

As discussed in Chapter 8 the the kinematic templates from `IBL0` regions are reweighted and used as the template for the `IBL1` regions due to lack of statistics. To estimate the effect of this method, the expected mass distribution using the original `IBL1` template is compared to the reweighted template,

as shown in Figure 9.3. The difference is taken as a systematic uncertainty and is one of the leading uncertainties for the `IBL1` regions.

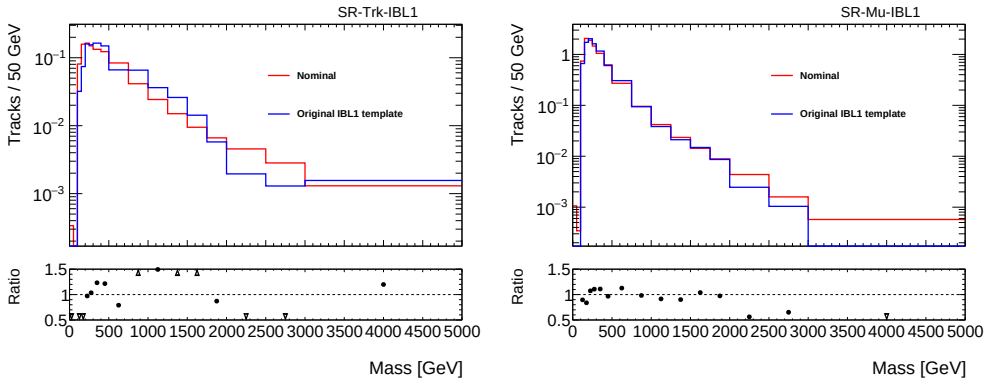

(a) `Trk-IBL1` **(b)** `Mu-IBL1`

Figure 9.3: The predicted mass distributions using the reweighted and original kinematic templates in the (a) `SR-Trk-IBL1` and (b) `SR-Mu-IBL1` regions. The fluctuations of the ratio as a function mass around 1 are due to the statistical uncertainty on the original template, which motivates the utiility of the reweighting method.

9.1.6 $E_{\mathrm{T}}^{\mathrm{miss}}$ TRIGGER REWEIGHTING

An alternative mass distribution is generated without applying the period-dependent $E_{\mathrm{T}}^{\mathrm{miss}}$ trigger weights described in Chapter 8.5. The difference between this and the nominal mass distribution, shown in Figure 9.4 is taken as an uncertainty on the $E_{\mathrm{T}}^{\mathrm{miss}}$ trigger reweighting and is less than $\sim$5% across all regions.

9.1.7 η SLICING

To evaluate any bias that might arise from our choice of η binning for the $\mathrm{d}E/\mathrm{d}x$ templates, the background estimation procedure is run using a different choice of binning: [0, 0.1, 0.45,

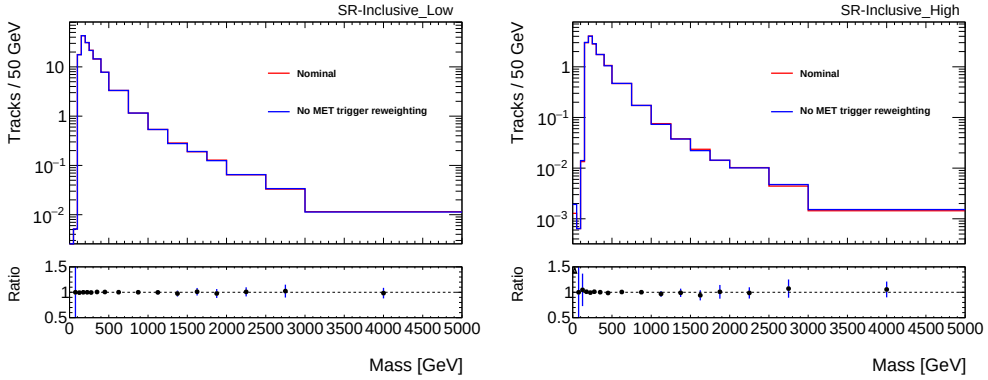

(a) `Inclusive_Low` **(b)** `Inclusive_High`

Figure 9.4: The predicted mass distributions using the $\mathrm{d}E/\mathrm{d}x$ template with and without reweighting to account for the $E_{\mathrm{T}}^{\mathrm{miss}}$ trigger threshold in the (a) `SR-Inclusive_Low` and (b) `SR-Inclusive_High` regions. The difference betwen the two distributions is less than 5% across all regions.

0.65, 0.85, 1.05, 1.25, 1.45, 1.8, 2.2, 2.5]. The alternative distributions are shown in Figure 9.5 for `SR-Inclusive_Low` and `SR-Inclusive_High`. The difference between the nominal and alternative distributions is less than 20% for all regions.

9.1.8 Background template statistics

The $\mathrm{d}E/\mathrm{d}x$ and kinematic toy distributions come from templates derived from data. As a result, the templates have statistical flucatuations and an associated statistical uncertainty. To estimate this uncertainty, the kinematic template is first smoothed using a kernel algorithm (see `ROOT` documentation [58]) and each bin in both templates is fluctuated following a Poisson distribution with a mean equal to the number of bin entries divided by the total number of entries. After generating thirty randomly fluctuated copies of the original template, alternative mass distributions are generated using these templates. The root mean square deviation of these mass distributions is then taken as the

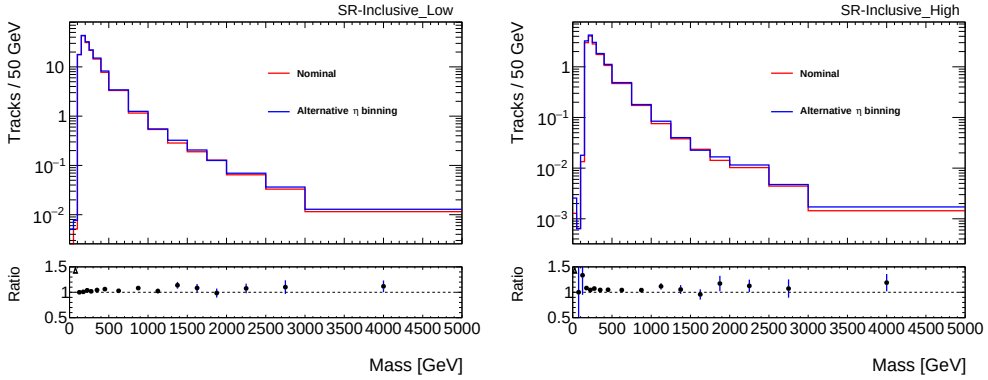

(a) `Inclusive_Low` **(b)** `Inclusive_High`

Figure 9.5: The predicted mass distributions using the original and alternative η binning of the $\mathrm{d}E/\mathrm{d}x$ template in the (a) `SR-Inclusive_Low` and (b) `SR-Inclusive_High` regions. The difference betwen the two distributions is less than 20% across all regions.

statistical uncertainty on the template. The statistical uncertainty for the `SR-Inclusive_Low` and `SR-Inclusive_High` regions is shown in Figure 9.6.

9.1.9 $\mathrm{d}E/\mathrm{d}x$ TAIL

Figure 8.8 shows the $\mathrm{d}E/\mathrm{d}x$ templates in each η slice. The tail of the $\mathrm{d}E/\mathrm{d}x$ template has a large effect on the background estimate in the signal and validation regions. The bias due to large statistical uncertainties in the tail is partially accounted for with the background template statistics uncertainty. However, bins in the smoothed template with zero entries, for example, are not fluctuated in the background template statistics uncertainty calculation procedure and their effect can be underestimated.

To account for this, a Crystal Ball function is fit to the tails of the $\mathrm{d}E/\mathrm{d}x$ templates. The $\mathrm{d}E/\mathrm{d}x$ distribution of the toy tracks is instead sampled from the fitted function for $\mathrm{d}E/\mathrm{d}x > 1.8$ (2.8) for

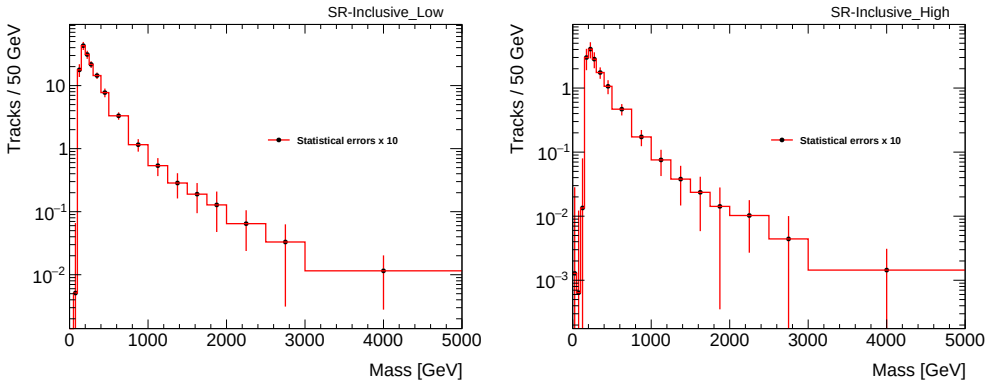

(a) `Inclusive_Low` **(b)** `Inclusive_High`

Figure 9.6: The predicted mass distributions in the (a) `SR-Inclusive_Low` and (b) `SR-Inclusive_High` regions, with the statistical uncertainty from the templates shown as the error on each bin (inflated by a factor of 10 for visibility).

`SR-Inclusive_Low`, `SR-Trk-IBL0_Low`, and `SR-Mu-IBL0_Low` regions (all other regions). The function is defined as

$$f(x) = \begin{cases} N \exp\left[-\frac{\alpha^2}{2}\right] \left(\frac{n}{|\alpha|} / \left(\frac{n_1}{|\alpha|} - |\alpha| - \frac{x-x_0}{\sigma}\right)\right)^n & \frac{x-x_0}{\sigma} \leq -\alpha \\ N \exp\left[-\frac{1}{2}\left(\frac{x-x_0}{\sigma}\right)^2\right] & \frac{x-x_0}{\sigma} > -\alpha \end{cases} \tag{9.5}$$

with free parameters $N, \sigma, x_0, n, \alpha$.

A few example fits are shown in Figure 9.7.

9.1.10 Summary of background uncertainties

The final statistical interpretation is determined using the observed and predicted yields within restricted regions of mass. The relevant systematic uncertainties, therefore, are those calculated for

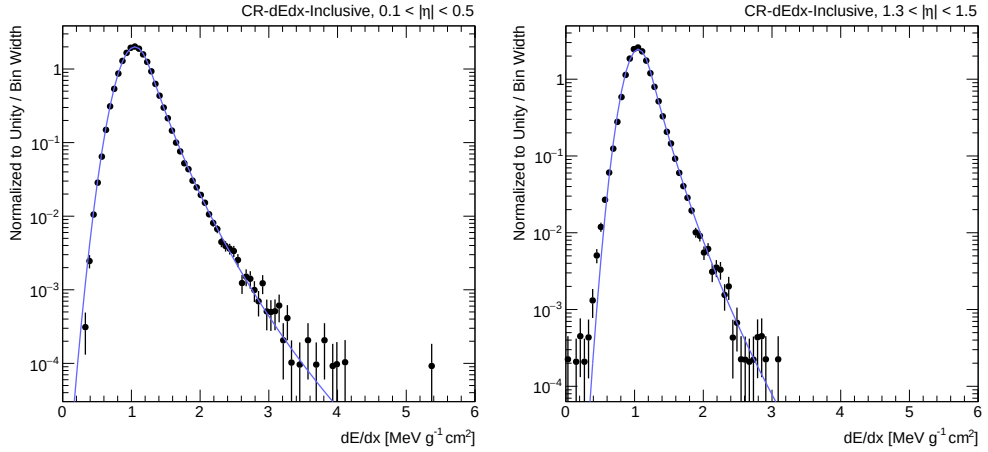

(a) 0.1 < $|\eta|$ < 0.5 **(b)** 1.3 < $|\eta|$ < 1.5

Figure 9.7: Examples of the Crystal Ball fits to the $\mathrm{d}E/\mathrm{d}x$ distributions for (a) tracks with 0.1 < $|\eta|$ < 0.5 in the `Inclusive` region and (b) tracks with 1.3 < $|\eta|$ < 1.5 in the `Inclusive` region.

each mass window. Mass window definitions are shown in Figure 7.7 and are optimized to target signals of varying masses and lifetimes. The associated uncertainties on the background prediction in each window are shown in Figures 9.8 and 9.9 for the discovery regions. The associated uncertainties for the exclusion regions are shown in Figures 9.10–9.15. Note that in these plots, the $\mathrm{d}E/\mathrm{d}x$ tail dependence on $E_{\mathrm{T}}^{\mathrm{miss}}$ uncertainty is abbreviated as the $\mathrm{d}E/\mathrm{d}x$ scale uncertainty.

The leading uncertainty for high target masses is the uncertainty associated with the unaccounted for background template correlations. For the `IBL1` regions, the uncertainty associated with using the reweighted `IBL0` kinematic template for the `IBL1` kinematic template is also significant, particularly at lower masses. For the `Trk` regions, the largest uncertainty at low masses is the $\mathrm{d}E/\mathrm{d}x$ scale uncertainty (the uncertainty due to the $\mathrm{d}E/\mathrm{d}x$ tail dependence on $E_{\mathrm{T}}^{\mathrm{miss}}$).

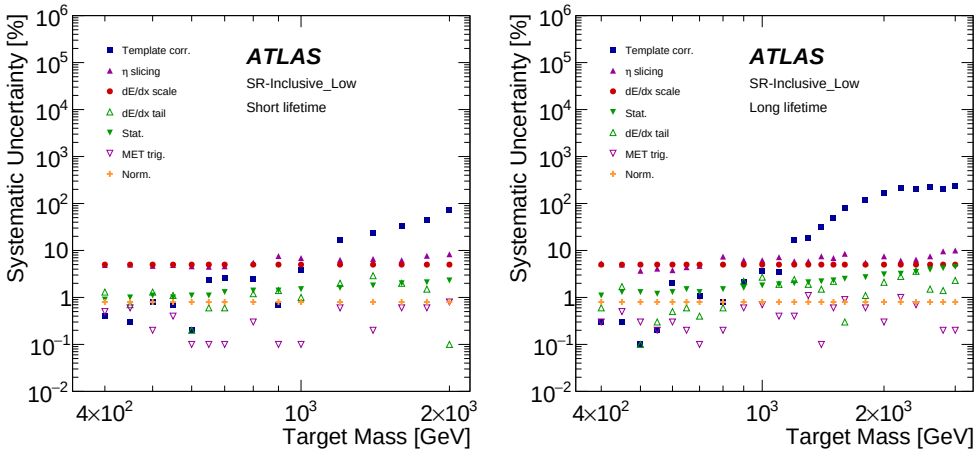

(a) SR-Inclusive_Low, $\tau \leq 1$ ns **(b)** SR-Inclusive_Low, $\tau > 1$ ns

Figure 9.8: The values for all of the background systematic uncertainties as a function of target mass for signals with lifetime(a) $\tau \leq 1$ ns and (b) $\tau > 1$ ns in the SR-Inclusive_Low region. For each mass point, the systematic uncertainty is integrated over the entire mass window associated to that mass [11].

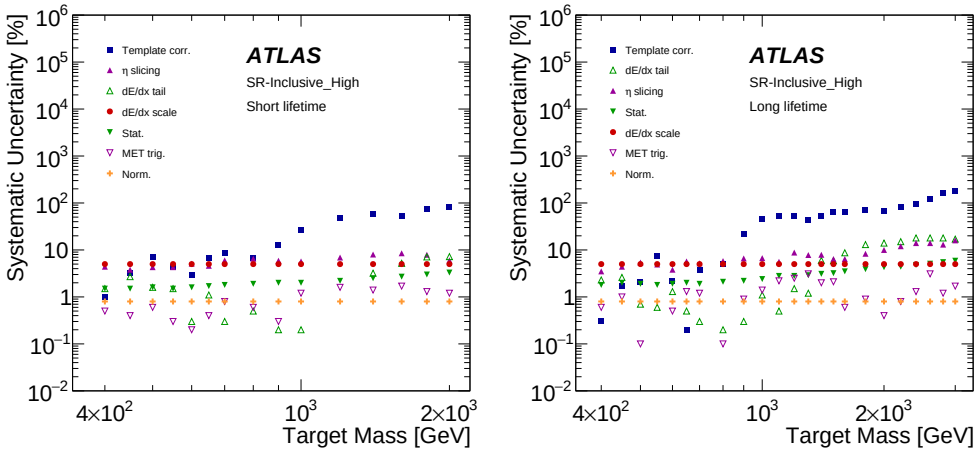

(a) SR-Inclusive_High, $\tau \leq 1$ ns **(b)** SR-Inclusive_High, $\tau > 1$ ns

Figure 9.9: The values for all of the background systematic uncertainties as a function of target mass for signals with lifetime(a) $\tau \leq 1$ ns and (b) $\tau > 1$ ns in the SR-Inclusive_High region. For each mass point, the systematic uncertainty is integrated over the entire mass window associated to that mass [11].

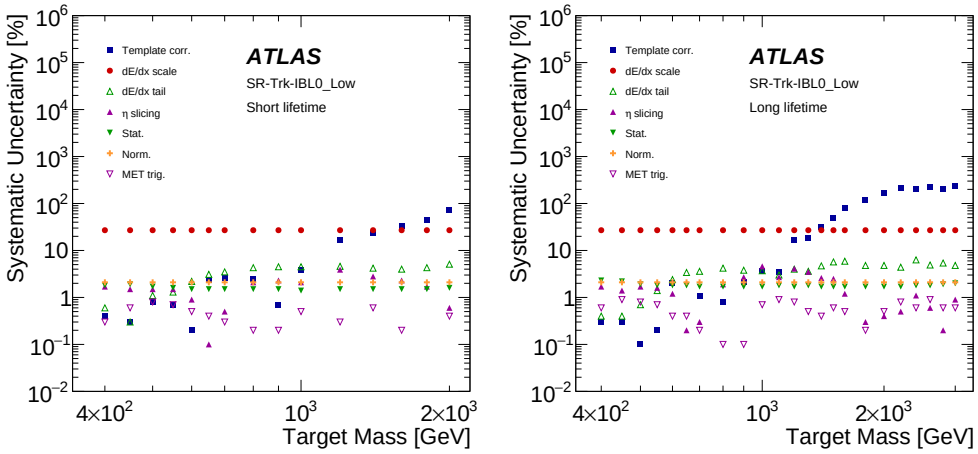

(a) SR-Trk-IBL0_Low, $\tau \leq 1$ ns **(b)** SR-Trk-IBL0_Low, $\tau > 1$ ns

Figure 9.10: The values for all of the background systematic uncertainties as a function of target mass for signals with lifetime(a) $\tau \leq 1$ ns and (b) $\tau > 1$ ns in the SR-Inclusive_Low region. For each mass point, the systematic uncertainty is integrated over the entire mass window associated to that mass [11].

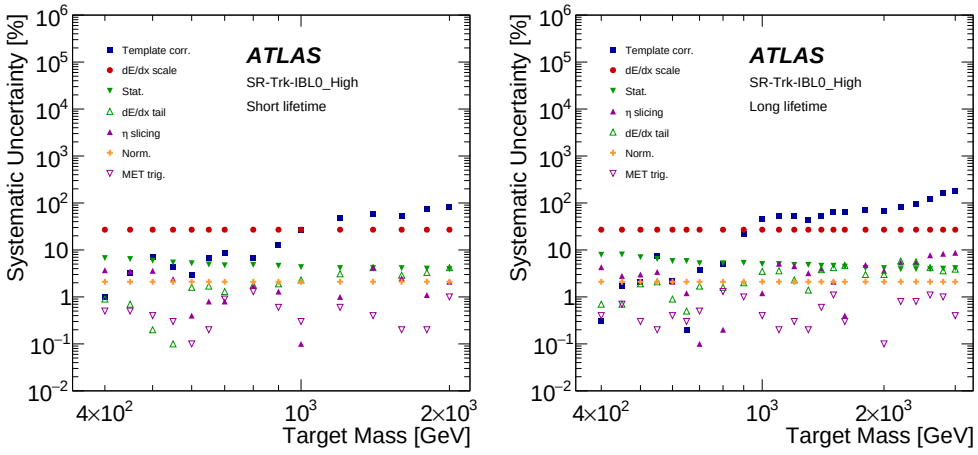

(a) SR-Trk-IBL0_High, $\tau \leq 1$ ns **(b)** SR-Trk-IBL0_High, $\tau > 1$ ns

Figure 9.11: The values for all of the background systematic uncertainties as a function of target mass for signals with lifetime(a) $\tau \leq 1$ ns and (b) $\tau > 1$ ns in the SR-Inclusive_High region. For each mass point, the systematic uncertainty is integrated over the entire mass window associated to that mass [11].

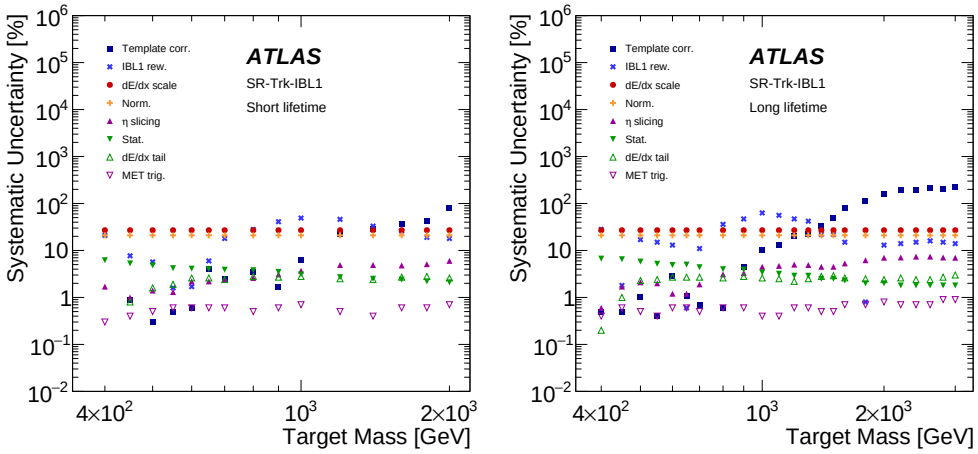

(a) SR-Trk-IBL1, $\tau \leq 1$ ns **(b)** SR-Trk-IBL1, $\tau > 1$ ns

Figure 9.12: The values for all of the background systematic uncertainties as a function of target mass for signals with lifetime(a) $\tau \leq 1$ ns and (b) $\tau > 1$ ns in the SR-Inclusive_High region. For each mass point, the systematic uncertainty is integrated over the entire mass window associated to that mass [11].

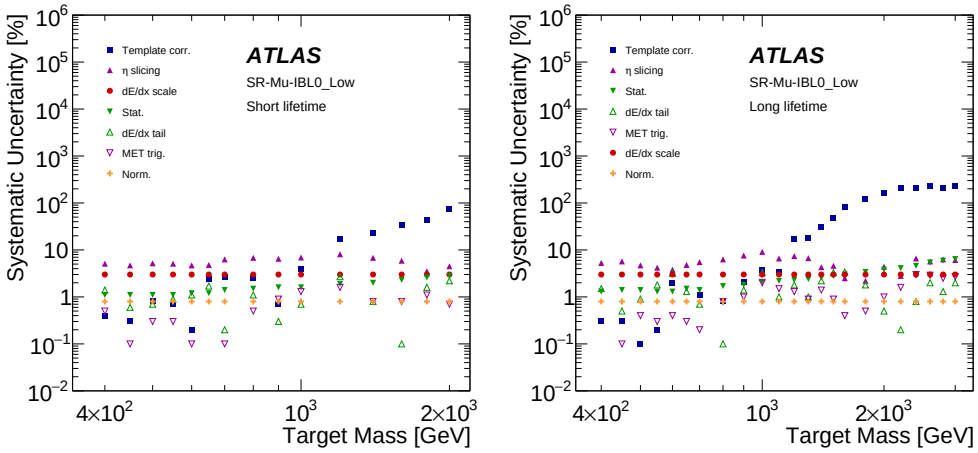

(a) SR-Mu-IBL0_Low, $\tau \leq 1$ ns **(b)** SR-Mu-IBL0_Low, $\tau > 1$ ns

Figure 9.13: The values for all of the background systematic uncertainties as a function of target mass for signals with lifetime(a) $\tau \leq 1$ ns and (b) $\tau > 1$ ns in the SR-Inclusive_Low region. For each mass point, the systematic uncertainty is integrated over the entire mass window associated to that mass [11].

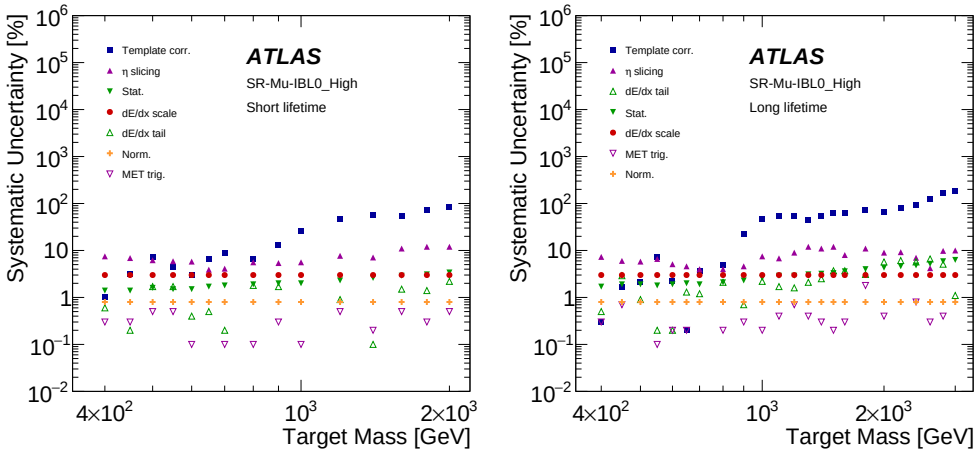

(a) SR-Mu-IBL0_High, $\tau \leq 1$ ns **(b)** SR-Mu-IBL0_High, $\tau > 1$ ns

Figure 9.14: The values for all of the background systematic uncertainties as a function of target mass for signals with lifetime(a) $\tau \leq 1$ ns and (b) $\tau > 1$ ns in the SR-Inclusive_High region. For each mass point, the systematic uncertainty is integrated over the entire mass window associated to that mass [11].

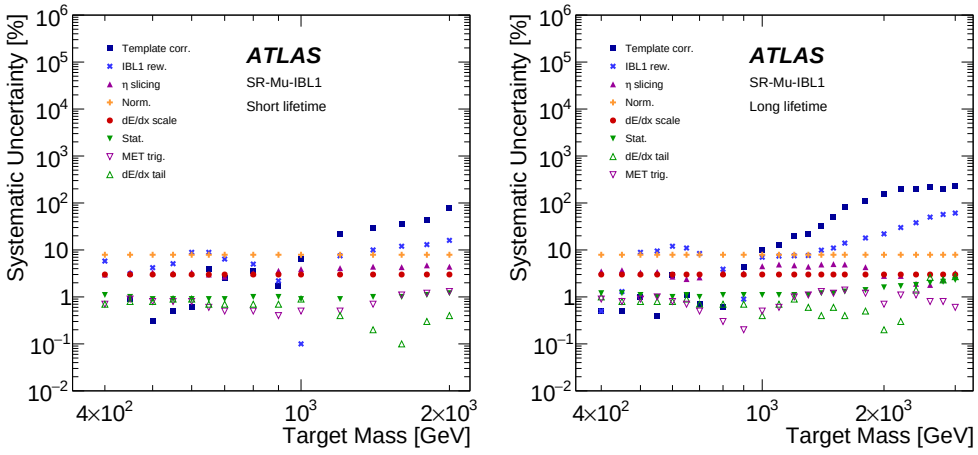

(a) SR-Mu-IBL1, $\tau \leq 1$ ns **(b)** SR-Mu-IBL1, $\tau > 1$ ns

Figure 9.15: The values for all of the background systematic uncertainties as a function of target mass for signals with lifetime(a) $\tau \leq 1$ ns and (b) $\tau > 1$ ns in the SR-Inclusive_High region. For each mass point, the systematic uncertainty is integrated over the entire mass window associated to that mass [11].

9.2 Uncertainties on the signal modeling

When setting limits on the various signal models, uncertainties on the various signal models are applied. The majority of these uncertainties are calculated and applied following ATLAS-wide recommendations.

Uncertainties on the signal yield include the luminosity uncertainty, which is measured to be 1.7% in $x - y$ beam scans [139], and theoretical uncertainties on the signal cross-section. Uncertainties on the Monte Carlo simulation modeling of the track and muon reconstruction, track kinematic properties, QCD radiation, the offline $E_{\mathrm{T}}^{\mathrm{miss}}$ calculation, and the trigger efficiency are also applied.

Although the probability of a track having an `IBL1` hit in simulation is calculated using the data-driven template described in Chapter 6, the low μ dataset with low momentum reconstruction, used to derive the template, was taken in 2017. In 2018, changes in the IBL front-end configuration led to a significantly increased probability of a track having an `IBL1` hit. The fraction of tracks with a hit in the IBL OF was monitored in a similar low μ dataset taken in 2018 as a function of $\beta\gamma$.

To assess the effect of this change, the fraction of tracks with a hit in the IBL OF as a function of $\beta\gamma$ were fit in slices of $|\eta|$. The ratio of these fits is used to reweight signal Monte Carlo tracks (see Figure 9.16b) and the difference in the signal yields is taken as a systematic uncertainty.

Overall, the leading signal uncertainties are the uncertainty on the probability of a track having a hit in the IBL OF, uncertainties on the modeling of ISR, the uncertainty on the modeling of the track momentum measurement due to a bias in the sagitta measurement, and uncertainties associated to the modeling of the offline $E_{\mathrm{T}}^{\mathrm{miss}}$ calculation.

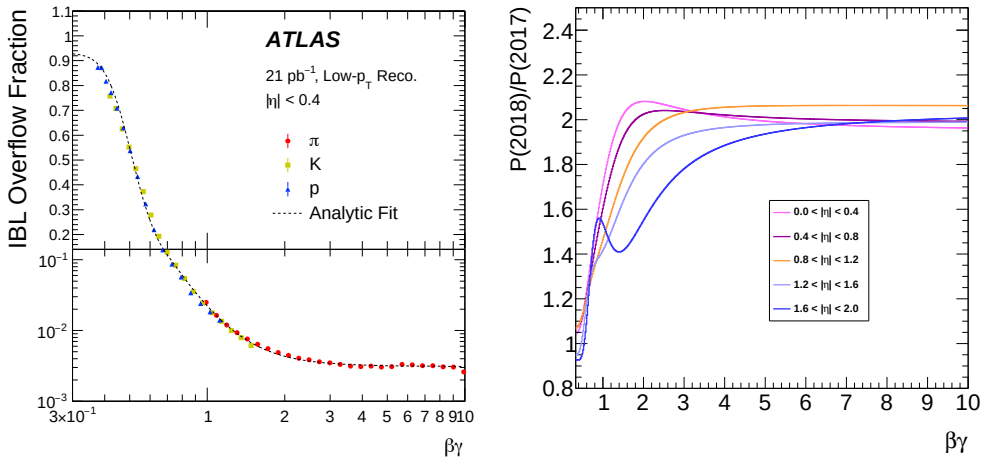

(a) 2017

(b) OF probability in 2018 vs 2017

Figure 9.16: The fraction of tracks with a hit in the IBL OF as a function of track $\beta\gamma$, in a low-μ calibration dataset taken in (a) 2017 [11]. Tracks are required to have $|\eta| < 0.4$. (b) shows the probability of a track having a hit in the IBL OF in 2018 compared to 2017.†

10

Results

The results and statistical interpretation are described in this chapter.

The observed mass distributions in the signal regions are shown in Section 10.1. For each signal region, the number of observed and expected tracks in a series of mass windows are extracted along with the corresponding systematic uncertainties.

To evaluate whether or not there is evidence for new physics in the observed data, a preliminary

statistical test is performed to quantify the agreement of the predicted and observed yields. The statistical test construction is described in Section 10.2, including the choice of a test statistic variable which is used to conduct a hypothesis test. This analysis employs a test statistic which is based on a ratio of likelihoods and is commonly used in high energy physics [140]. The likelihoods quantify the compatibility of an assumed distribution with the observed data. The likelihood and statistical analysis is implemented using the `pyhf` package [141, 142], which is a python-based implementation of the `HistFactory` package [143].

Finally, the results of the statistical test are shown in Section 10.3.

10.1 Signal region results

The observed and predicted mass distributions for tracks in each of the signal regions is shown in Figures 10.1–10.4.* The data agrees with the predicted background distribution in the `SR-Inclusive_Low` and `SR-Inclusive_High`, except for a deviation at high mass in the `SR-Inclusive_High` region. This deviation can be seen in Figure 10.1b and is split across the exclusion signal regions shown in Figures 10.3b, 10.2b, 10.4b, 10.4a.

The observed and predicted yields for each mass window are shown in Table 10.1–10.4. The mass windows, which increase as a function of target mass, are overlapping and therefore correlated. In the following section, the agreement is quantified in each window.

*Note that for these plots, the displayed systematic uncertainty does not have the smoothing procedure described in Chapter 9.1.1 because the procedure is only applicable to a defined mass window.

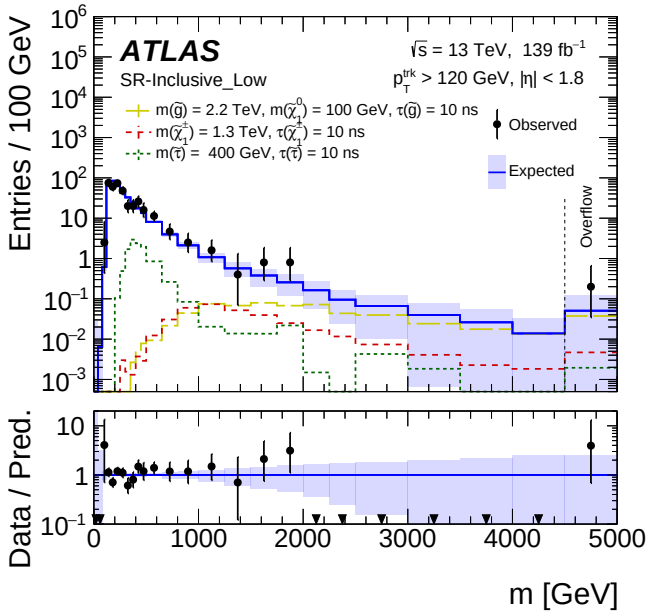

(a) SR-Inclusive_Low

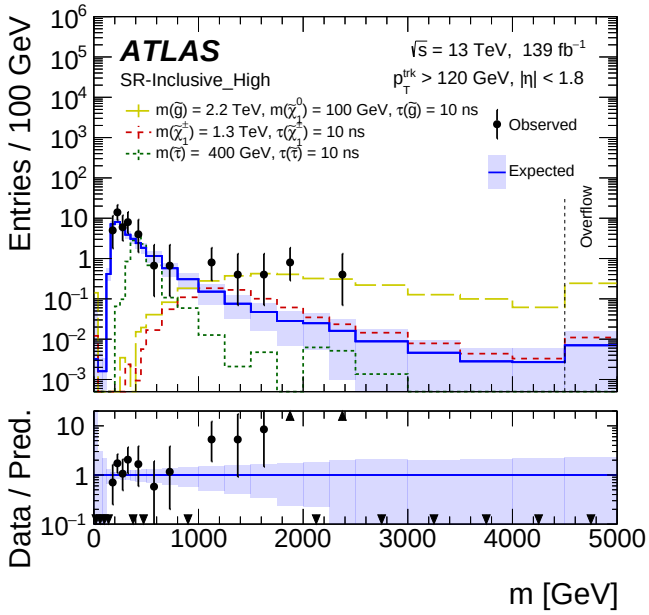

(b) SR-Inclusive_High

Figure 10.1: The predicted and observed mass distributions in the (a) SR-Inclusive_Low and the (b) SR-Inclusive_High signal regions. Example distributions expected from signal are overlaid [11].

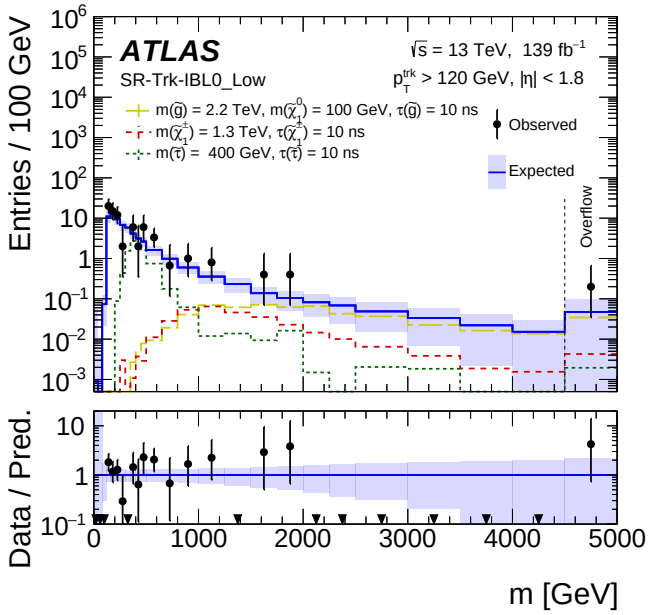

(a) SR-Trk-IBL0_Low

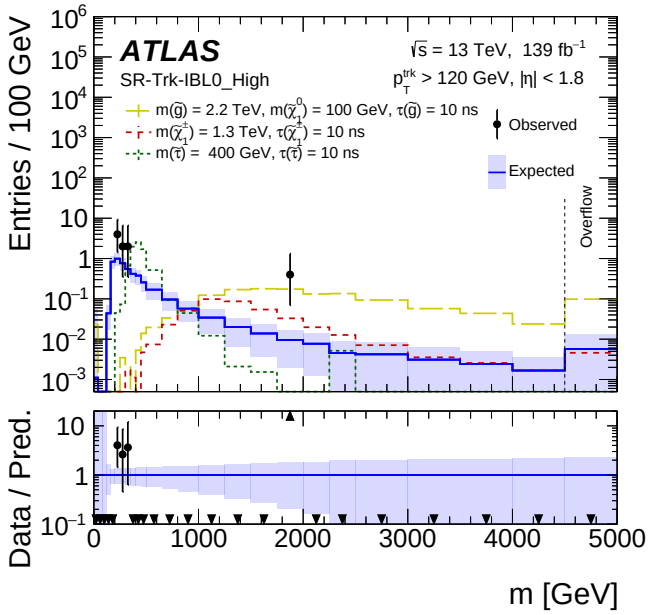

(b) SR-Trk-IBL0_High

Figure 10.2: The predicted and observed mass distributions in the (a) SR-Trk-IBL0_Low and the (b) SR-Trk-IBL0_High signal regions. Example distributions expected from signal are overlaid [11].

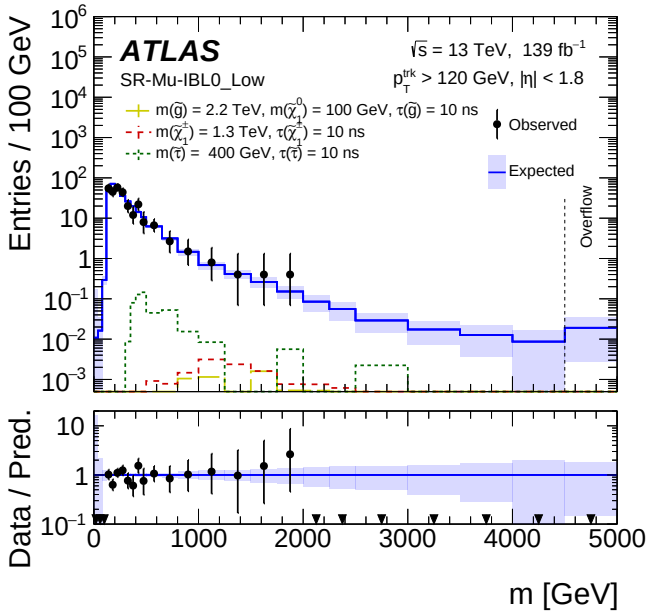

(a) SR-Mu-IBL0_Low

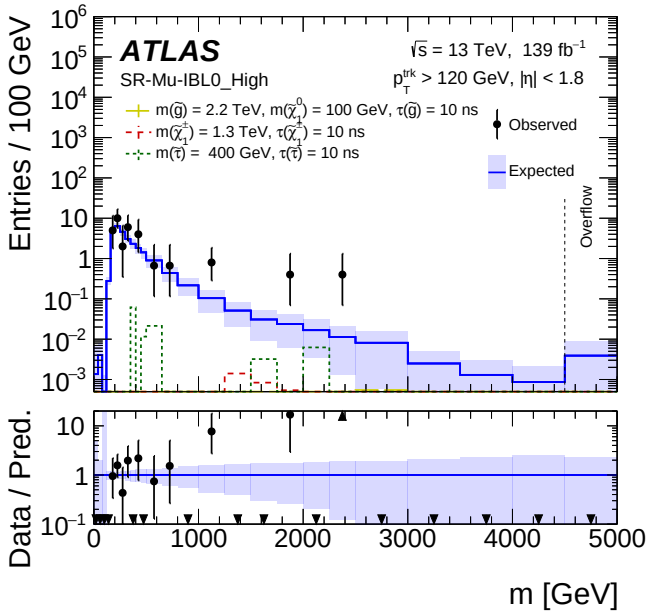

(b) SR-Mu-IBL0_High

Figure 10.3: The predicted and observed mass distributions in the (a) SR-Mu-IBL0_Low and the (b) SR-Mu-IBL0_-High signal regions. Example distributions expected from signal are overlaid [11].

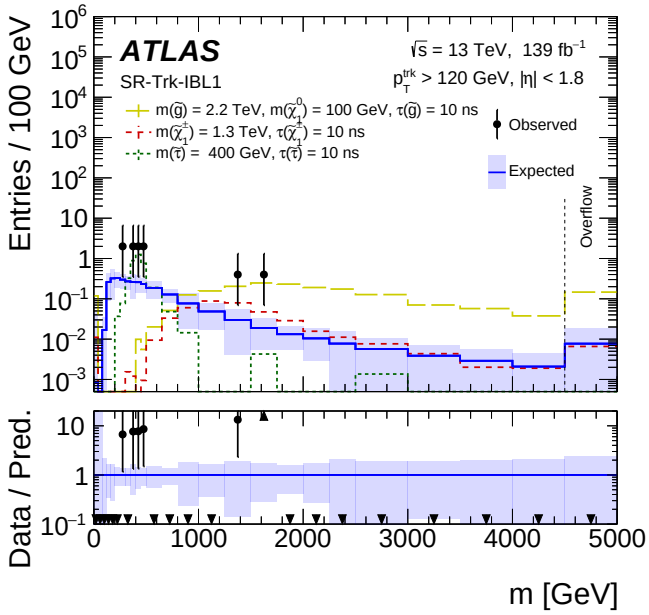

(a) SR-Trk-IBL1

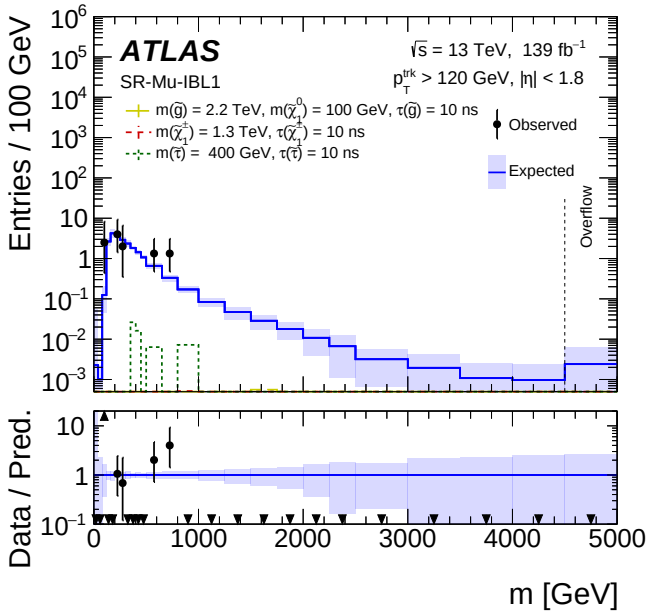

(b) SR-Mu-IBL1

Figure 10.4: The predicted and observed mass distributions in the (a) SR-Trk-IBL1 and the (b) SR-Mu-IBL1 signal regions. Example distributions expected from signal are overlaid [11].

SR-Inclusive_Low			
Mass	Lifetime	Obs. Yield	Exp. Yield
100	long	63	68 ± 4
200	long	54	63 ± 4
300	long	35	40.9 ± 2.7
400	long	33	29.2 ± 2.2
450	long	30	21.5 ± 1.6
500	long	27	19.4 ± 1.2
550	long	29	21.8 ± 1.5
600	long	24	18.4 ± 1.3
650	long	19	15 ± 1
700	long	21	16.6 ± 1.2
800	long	14	12.0 ± 1.1
900	long	13	10.4 ± 0.9
1000	long	11	8.6 ± 0.8
1100	long	10	7.1 ± 0.7
1200	long	10	6.7 ± 1.3
1300	long	9	6.1 ± 1.2
1400	long	8	5.2 ± 1.7
1500	long	7	4.9 ± 2.4
1600	long	5	4.2 ± 3.4
1800	long	4	3^{+4}_{-3}
2000	long	3	3^{+4}_{-3}
2200	long	4	2^{+5}_{-2}
2400	long	3	2^{+4}_{-2}
2600	long	1	2^{+4}_{-2}
2800	long	1	$1.5^{+3.1}_{-1.5}$
3000	long	1	$1.4^{+3.1}_{-1.4}$

SR-Inclusive_High			
Mass	Lifetime	Obs. Yield	Exp. Yield
100	long	5	3.9 ± 0.6
200	long	7	5.5 ± 0.6
300	long	7	5.1 ± 0.5
400	long	2	3.83 ± 0.26
450	long	2	3.00 ± 0.23
500	long	1	2.73 ± 0.22
550	long	2	3.06 ± 0.32
600	long	2	2.64 ± 0.19
650	long	2	2.07 ± 0.17
700	long	2	2.4 ± 0.2
800	long	3	1.74 ± 0.16
900	long	3	1.5 ± 0.4
1000	long	4	1.2 ± 0.6
1100	long	4	1.0 ± 0.5
1200	long	6	0.9 ± 0.5
1300	long	6	0.8 ± 0.4
1400	long	7	0.7 ± 0.4
1500	long	6	0.6 ± 0.4
1600	long	5	0.54 ± 0.35
1800	long	4	0.44 ± 0.32
2000	long	3	0.36 ± 0.25
2200	long	3	0.33 ± 0.28
2400	long	3	0.29 ± 0.28
2600	long	3	$0.25^{+0.31}_{-0.25}$
2800	long	1	$0.2^{+0.4}_{-0.2}$
3000	long	1	$0.2^{+0.4}_{-0.2}$

Table 10.1: Observed and predicted yields within each mass window in the SR-Inclusive_Low and SR-Inclusive_High regions. The error on the expected yield is the sum in quadrature of the systematic uncertainties, including the statistical error on the background template.

SR-Trk-IBL0_Low				SR-Trk-IBL0_High			
Mass	Lifetime	Obs. Yield	Exp. Yield	Mass	Lifetime	Obs. Yield	Exp. Yield
100	long	14	10.6 ± 2.9	100	long	0	0.45 ± 0.15
200	long	12	9.6 ± 2.6	200	long	1	0.65 ± 0.19
300	long	1	6.8 ± 1.9	300	long	2	0.7 ± 0.2
400	long	8	5.2 ± 1.4	400	long	0	0.55 ± 0.16
450	long	8	4.1 ± 1.1	450	long	0	0.43 ± 0.12
500	long	8	3.9 ± 1.1	500	long	0	0.40 ± 0.11
550	long	8	4.4 ± 1.2	550	long	0	0.45 ± 0.13
600	long	6	4.0 ± 1.1	600	long	0	0.40 ± 0.11
650	long	3	3.3 ± 0.9	650	long	0	0.34 ± 0.09
700	long	4	3.9 ± 1.1	700	long	0	0.40 ± 0.11
800	long	5	3.3 ± 0.9	800	long	0	0.32 ± 0.09
900	long	5	3.0 ± 0.8	900	long	0	0.3 ± 0.1
1000	long	4	2.8 ± 0.8	1000	long	0	0.26 ± 0.14
1100	long	5	2.4 ± 0.7	1100	long	0	0.22 ± 0.13
1200	long	4	2.4 ± 0.8	1200	long	1	0.23 ± 0.14
1300	long	4	2.3 ± 0.7	1300	long	1	0.21 ± 0.11
1400	long	3	2.2 ± 0.9	1400	long	1	0.20 ± 0.12
1500	long	2	2.1 ± 1.1	1500	long	1	0.19 ± 0.13
1600	long	2	1.9 ± 1.7	1600	long	1	0.17 ± 0.12
1800	long	2	$1.7^{+2.1}_{-1.7}$	1800	long	1	0.16 ± 0.12
2000	long	2	$1.5^{+2.5}_{-1.5}$	2000	long	1	$0.1^{+0.1}_{-0.1}$
2200	long	3	$1.5^{+3.1}_{-1.5}$	2200	long	1	0.14 ± 0.12
2400	long	2	$1.4^{+2.9}_{-1.4}$	2400	long	1	$0.13^{+0.13}_{-0.13}$
2600	long	1	$1.2^{+2.7}_{-1.2}$	2600	long	1	$0.12^{+0.15}_{-0.12}$
2800	long	1	$1.1^{+2.3}_{-1.1}$	2800	long	0	$0.11^{+0.18}_{-0.11}$
3000	long	1	$1.0^{+2.4}_{-1.0}$	3000	long	0	$0.10^{+0.18}_{-0.10}$

Table 10.2: Observed and predicted yields within each mass window in the SR-Trk-IBL0_Low and SR-Trk-IBL0_High regions. The error on the expected yield is the sum in quadrature of the systematic uncertainties, including the statistical error on the background template.

SR-Mu-IBL0_Low			
Mass	Lifetime	Obs. Yield	Exp. Yield
100	long	48	56.2 ± 1.9
200	long	40	53.4 ± 2.1
300	long	33	33.0 ± 1.9
400	long	22	23.2 ± 1.5
450	long	20	17.1 ± 1.1
500	long	14	15.1 ± 0.9
550	long	16	17 ± 1
600	long	14	14.3 ± 0.9
650	long	12	11.1 ± 0.7
700	long	13	12.5 ± 0.8
800	long	7	8.9 ± 0.7
900	long	8	7.5 ± 0.7
1000	long	7	5.9 ± 0.7
1100	long	5	4.8 ± 0.4
1200	long	6	4.5 ± 0.8
1300	long	5	4.0 ± 0.8
1400	long	5	3.4 ± 1.1
1500	long	5	3.1 ± 1.5
1600	long	3	2.6 ± 2.1
1800	long	2	$2.0^{+2.4}_{-2.0}$
2000	long	1	$1.6^{+2.6}_{-1.6}$
2200	long	1	$1.4^{+2.9}_{-1.4}$
2400	long	1	$1.1^{+2.4}_{-1.1}$
2600	long	0	1^{+2}_{-1}
2800	long	0	$0.8^{+1.6}_{-0.8}$
3000	long	0	$0.7^{+1.5}_{-0.7}$

SR-Mu-IBL0_High			
Mass	Lifetime	Obs. Yield	Exp. Yield
100	long	5	2.9 ± 0.5
200	long	6	4.2 ± 0.4
300	long	4	4.1 ± 0.3
400	long	2	2.91 ± 0.24
450	long	2	2.30 ± 0.18
500	long	1	2.12 ± 0.15
550	long	2	2.35 ± 0.25
600	long	2	2.03 ± 0.13
650	long	2	1.61 ± 0.10
700	long	2	1.81 ± 0.12
800	long	3	1.27 ± 0.10
900	long	2	1.10 ± 0.25
1000	long	2	0.8 ± 0.4
1100	long	2	0.65 ± 0.35
1200	long	3	0.63 ± 0.34
1300	long	3	0.56 ± 0.26
1400	long	4	0.51 ± 0.28
1500	long	3	0.46 ± 0.29
1600	long	2	0.39 ± 0.25
1800	long	2	0.31 ± 0.23
2000	long	2	0.26 ± 0.17
2200	long	2	0.23 ± 0.19
2400	long	2	0.20 ± 0.19
2600	long	2	$0.17^{+0.22}_{-0.17}$
2800	long	1	$0.15^{+0.24}_{-0.15}$
3000	long	1	$0.13^{+0.23}_{-0.13}$

Table 10.3: Observed and predicted yields within each mass window in the SR-Mu-IBL0_Low and SR-Mu-IBL0_-High regions. The error on the expected yield is the sum in quadrature of the systematic uncertainties, including the statistical error on the background template.

SR-Trk-IBL1				SR-Mu-IBL1			
Mass	Lifetime	Obs. Yield	Exp. Yield	Mass	Lifetime	Obs. Yield	Exp. Yield
100	long	0	0.27 ± 0.17	100	long	1	3.2 ± 0.6
200	long	0	0.26 ± 0.15	200	long	2	3.3 ± 0.5
300	long	1	0.31 ± 0.11	300	long	1	2.8 ± 0.5
400	long	3	0.40 ± 0.18	400	long	0	2.26 ± 0.21
450	long	2	0.37 ± 0.13	450	long	0	1.74 ± 0.16
500	long	1	0.41 ± 0.16	500	long	4	1.6 ± 0.2
550	long	1	0.49 ± 0.18	550	long	4	1.76 ± 0.23
600	long	0	0.48 ± 0.18	600	long	4	1.51 ± 0.23
650	long	0	0.42 ± 0.15	650	long	4	1.21 ± 0.17
700	long	0	0.50 ± 0.18	700	long	4	1.37 ± 0.17
800	long	0	0.43 ± 0.21	800	long	2	0.99 ± 0.10
900	long	1	0.40 ± 0.23	900	long	0	0.85 ± 0.09
1000	long	2	0.36 ± 0.26	1000	long	0	0.69 ± 0.11
1100	long	2	0.32 ± 0.22	1100	long	0	0.55 ± 0.10
1200	long	2	0.3 ± 0.2	1200	long	0	0.52 ± 0.12
1300	long	2	0.30 ± 0.18	1300	long	0	0.47 ± 0.12
1400	long	2	0.29 ± 0.15	1400	long	0	0.40 ± 0.14
1500	long	2	0.27 ± 0.17	1500	long	0	0.36 ± 0.19
1600	long	2	0.25 ± 0.22	1600	long	0	0.30 ± 0.25
1800	long	1	$0.22^{+0.26}_{-0.22}$	1800	long	0	$0.23^{+0.27}_{-0.23}$
2000	long	0	$0.2^{+0.3}_{-0.2}$	2000	long	0	$0.18^{+0.28}_{-0.18}$
2200	long	0	$0.2^{+0.4}_{-0.2}$	2200	long	0	$0.2^{+0.3}_{-0.2}$
2400	long	0	$0.17^{+0.34}_{-0.17}$	2400	long	0	$0.13^{+0.26}_{-0.13}$
2600	long	0	$0.15^{+0.33}_{-0.15}$	2600	long	0	$0.10^{+0.23}_{-0.10}$
2800	long	0	$0.14^{+0.29}_{-0.14}$	2800	long	0	$0.09^{+0.18}_{-0.09}$
3000	long	0	$0.1^{+0.3}_{-0.1}$	3000	long	0	$0.07^{+0.18}_{-0.07}$

Table 10.4: Observed and predicted yields within each mass window in the SR−Trk−IBL1 and SR−Mu−IBL1 regions. The error on the expected yield is the sum in quadrature of the systematic uncertainties, including the statistical error on the background template.

To quantify the extent of the deviation of observation from prediction, a hypothesis test to reject the background-only hypothesis is conducted for each mass window and signal region. The hypothesis test quantifies the compatibility of the observed data originating solely from background-like processes.

The test is conducted by calculating the value of a test statistic variable which is designed to be a powerful handle on the compatibility of the observed data with the hypothesis. The observed test statistic value is then compared with the expected distribution of the test statistic values which would originate from a background-only hypothesis. The probability of the observed test statistic can then be calculated from the expected distribution and is quoted as the p-value. The significance of the observation is then computed from the p-value.

The chosen test statistic q_0 is defined as [140]:

$$q_0 = \begin{cases} -2\ \ln\lambda(0) & \hat{\mu} < 0, \\ 0 & \hat{\mu} > 0, \end{cases} \tag{10.1}$$

where μ is the strength of the signal.

$\lambda(\mu)$ is the profile likelihood ratio

$$\lambda(\mu) = \frac{L(\mu, \hat{\hat{\theta}})}{L(\hat{\mu}, \hat{\theta})}. \tag{10.2}$$

L is the likelihood of the given parameters describing the underlying distribution given the observed data. The underlying distribution is parameterized by μ, θ, where μ is the parameter of interest and θ is the set of nuisance parameters. $\hat{\mu}$ and $\hat{\theta}$ are the values of μ, θ which maximize the likelihood L, while $\hat{\hat{\theta}}$ represents the set of θ values which maximize the likelihood with a fixed μ. For q_0, $\mu = 0$.

For excluding the existence of a certain signal model, a statistical test is conducted assuming a signal-and-background hypothesis. The following test statistic $\tilde{q}_\mu$ is used [140].

$$\tilde{q}_\mu = \begin{cases} -2 \ln \dfrac{L(\mu, \hat{\hat{\theta}}(\mu))}{L(0, \hat{\hat{\theta}}(0))} & \hat{\mu} < 0, \\ -2 \ln \dfrac{L(\mu, \hat{\hat{\theta}}(\mu))}{L(\hat{\mu}, \hat{\theta})} & 0 \leq \hat{\mu} \leq \mu, \\ 0 & \hat{\mu} > \mu, \end{cases} \tag{10.3}$$

Note that the use of this test statistic relies on a positive signal; i.e. $\mu \geq 0$.

10.2.1 Likelihood construction

The likelihood construction and notation in the following section is based on [141, 143, 144].

The likelihood L is defined as:

$$L(\boldsymbol{\phi}) = \prod_{c \in \text{channels}} \text{Poisson}\,(n_c|\nu_c) \prod_{\theta \in \boldsymbol{\theta}} c_\theta(a_\theta|\theta). \tag{10.4}$$

$\boldsymbol{\phi}$ is the set of all parameters $\boldsymbol{\phi} = (\mu, \boldsymbol{\theta})$. ν_c is the expected event rate in each channel c defined in the set of signal regions, and n_c is the observed number of events. The term Poisson $(n_c|\nu_c)$ is

the likelihood that, given n_c events are observed, ν_c describes the mean of the underlying Poisson distribution. Analytically this is expressed as

$$\text{Poisson}\,(n_c|\nu_c) = {\nu_c}^{n_c}\frac{e^{-\nu_c}}{n_c!}. \tag{10.5}$$

$c_\theta(a_\theta|\theta)$ is a constraint on the parameter θ, typically Gaussian or Poisson.

ν_c can be expressed as

$$\nu_c(\phi) = \prod_{\kappa\in\boldsymbol{\kappa}} \kappa_c(\boldsymbol{\mu},\boldsymbol{\theta}) \left(\nu_c^0(\boldsymbol{\mu},\boldsymbol{\theta}) + \sum_{\Delta\in\boldsymbol{\Delta}} \Delta_c(\boldsymbol{\mu},\boldsymbol{\theta})\right) \tag{10.6}$$

For this analysis, $\nu_c^0(\boldsymbol{\mu},\boldsymbol{\theta})$ is the expected number of events in a given signal region. For a background-only hypothesis, this is equivalent to the expected background prediction b_c in channel c. For the signal-and-background hypothesis, $\nu_c^0 = \mu s_c + b_c$, where s_c is the expected signal in channel c scaled by the parameter of interest, μ.

The modifiers Δ_c and κ_c are used to include the effect of systematic uncertainties on the background prediction. Each modifier is parameterized by an undetermined nuisance parameter θ. The systematic uncertainties are used to constrain the value of the nuisance parameter θ through the constraint terms $c_\theta(a_\theta|\theta)$ in the maximum likelihood fit where θ is allowed to float.

Δ_c is an additive modifier and κ_c is a multiplicative modifier to the expected yield. All of the systematic uncertainties are included in the likelihood through multiplicative modifiers.

The multiplicative modifiers and the associated normally-distributed constraints for all systematics with the exception of the statistical template uncertainty are defined as

$$\begin{aligned} \kappa_c(\theta_i) &= (1+\sigma_c)^{\theta_i} \\ c(\theta_i) &= \text{Gaussian}\,(a=0|\theta_i, \sigma=1) \end{aligned} \tag{10.7}$$

where σ_c is the relative systematic uncertainty associated to channel c, as estimated in Chapter 9, and θ_i is the associated nuisance parameter. Analytically Gaussian $(a=0|\theta_i, \sigma=1)$ is expressed as

$$c(\theta_i) = \frac{1}{\sqrt{2\pi}}\text{Exp}\left[-\frac{1}{2}\frac{\theta_i^2}{\sigma^2}\right] \tag{10.8}$$

Finally, the multiplicative modifier associated to the statistical template uncertainty is defined with a Poisson constraint:

$$\begin{aligned} \kappa_c(\theta_i) &= \theta_i \\ c(\theta_i) &= \text{Poisson}\left(\sigma_c^{-2}|\sigma_c^{-2}\theta_i\right) \end{aligned} \tag{10.9}$$

More details on likelihood construction in high energy physics are in [143].

One added complication is that any systematic effects introduced in the likelihood through the modifiers may have a shared source across several signal regions. To account for this, nuisance parameters can be shared across various regions. The detailed treatment of shared nuisance parameters is shown in Table 10.5 for the exclusive signal regions and Table 10.6 for the discovery signal regions.

For setting limits on signal models, uncertainties on the signal modeling are also considered. Table 10.7 describes the nuisance parameters allocated for the signal systematics and how any correlations between signal regions are accounted for. To reduce the number of nuisance parameters and

Systematic	Channel					
	Trk IBLOF0_Low	Trk IBLOF0_High	Trk IBLOF1	Mu IBLOF0_Low	Mu IBLOF0_High	Mu IBLOF1
Template correlations	θ_0	θ_0	θ_0	θ_1	θ_1	θ_1
$\mathrm{d}E/\mathrm{d}x$ scale	θ_2	θ_2	θ_2	θ_3	θ_3	θ_3
IBL1 reweighting	θ_4	θ_4	θ_4	θ_5	θ_5	θ_5
η slicing	θ_6	θ_6	θ_7	θ_6	θ_6	θ_7
$\mathrm{d}E/\mathrm{d}x$ tail	θ_8	θ_8	θ_8	θ_8	θ_8	θ_8
Statistics	θ_9	θ_{10}	θ_{11}	θ_{12}	θ_{13}	θ_{14}
Normalization	θ_{15}	θ_{15}	θ_{16}	θ_{17}	θ_{17}	θ_{18}
$E_{\mathrm{T}}^{\mathrm{miss}}$ trig.	θ_{19}	θ_{19}	θ_{19}	θ_{19}	θ_{19}	θ_{19}

Table 10.5: The treatment of correlations across the exclusion signal regions is encapsulated in the nuisance parameters assigned to each systematic uncertainty. If the regions share a nuisance parameter, they are treated as fully correlated in the likelihood. Otherwise the effect of the uncertainty can vary independently between regions.[†]

Systematic	Channel	
	SR-Inclusive_Low	SR-Inclusive_High
Template correlations	θ_0	θ_0
$\mathrm{d}E/\mathrm{d}x$ scale	θ_1	θ_1
IBL1 reweighting	θ_2	θ_2
η slicing	θ_3	θ_3
$\mathrm{d}E/\mathrm{d}x$ tail	θ_4	θ_4
Statistics	θ_5	θ_6
Normalization	θ_7	θ_7
$E_{\mathrm{T}}^{\mathrm{miss}}$ trig.	θ_8	θ_8

Table 10.6: The treatment of correlations across the discovery signals is encapsulated in the nuisance parameters assigned to each systematic uncertainty. If the regions share a nuisance parameter, they are treated as fully correlated in the likelihood. Otherwise the effect of the uncertainty can vary independently between regions.[†]

improve the stability of the multibin fit, the subleading systematic uncertainties are summed in quadrature into one *combined* systematic, while the three dominant signal systematics are incorporated separately.

Systematic	Channel					
	Trk IBLOF0_Low	Trk IBLOF0_High	Trk IBLOF1	Mu IBLOF0_Low	Mu IBLOF0_High	Mu IBLOF1
Combined	θ_0^s	θ_1^s	θ_2^s	θ_3^s	θ_4^s	θ_5^s
ISR (Var3c tune)	θ_6^s	θ_6^s	θ_6^s	θ_6^s	θ_6^s	θ_6^s
IBL OF probability	θ_7^s	θ_7^s	θ_7^s	θ_7^s	θ_7^s	θ_7^s
Track q/p sagitta bias	θ_8^s	θ_8^s	θ_8^s	θ_8^s	θ_8^s	θ_8^s

Table 10.7: The treatment of correlations for the signal systematics across the exclusion signal regions is encapsulated in the nuisance parameters assigned to each systematic uncertainty. All signal systematic uncertainties are summed in quadrature into one combined number, with the exception of the uncertainties on the probability of having a hit in the IBL OF, the modeling of the track momentum measurement due to a sagitta measurement bias, and the radiation modeling uncertainty on the initial state radiation (Var3C, see [115]). If the regions share a nuisance parameter, they are treated as fully correlated in the likelihood. Otherwise the effect of the uncertainty can vary independently between regions.

10.3 Statistical interpretation

With the observed and expected data in each mass window (and the associated uncertainties), the value of the test statistic can be computed. The profile likelihood $\lambda(\mu) = \frac{L(\mu,\hat{\hat{\theta}})}{L(\hat{\mu},\hat{\theta})}$ requires a fit for μ, θ using the observed data.

Due to the low-count nature of the signal regions, the asymptotic formulae in [140] for the test statistic distributions do not apply. For each mass window, the expected distribution of the test statistic assuming a background-only hypothesis is generated using Monte Carlo toys. The observed and auxiliary data described by the likelihood function are randomly fluctuated for each toy. These data are then treated as sample observations and used to calculate a sample test statistic value. 1 mil-

lion toys are thrown to generate the background-only distribution. Using these toy distributions, the corresponding probability of the observed test statistic, or *p-value*, can be calculated.

The *significance* Z can then be calculated from the p-value through the formula [140]

$$Z = \Phi^{-1}(1 - p), \tag{10.10}$$

where Φ^{-1} refers to the inverse cumulative normal distribution.

The local p-values and associated significances in each mass window for the signal region is shown in Figures 10.5– 10.8. The maximum deviation is observed for the mass window targeting long lifetime signals of mass 1.4 TeV in the `SR-Inclusive_High` region, with a local significance of 3.6σ. The effect of the excess can be observed over several mass windows, which are defined to be overalapping in mass, in the `SR-Inclusive_High` region. This excess is also visible in the exclusion regions, although with a smaller significance.

For low mass windows, the observed data is compatible with SM expectation, largely within $1 - 2\sigma$. The largest significance at lower mass is in the `SR-Trk-IBL1` region, with a significance of $\approx 2.5\sigma$.

Because the analysis defines multiple mass windows, the look-elsewhere effect must be taken into account to calculate a global significance. This involves running 1 million toy analysis experiments. In each experiment the expected background mass distribution in the `SR-Inclusive_High` region, generated according to the procedure in Chapter 8, is smeared by a scale factor α. α is defined as

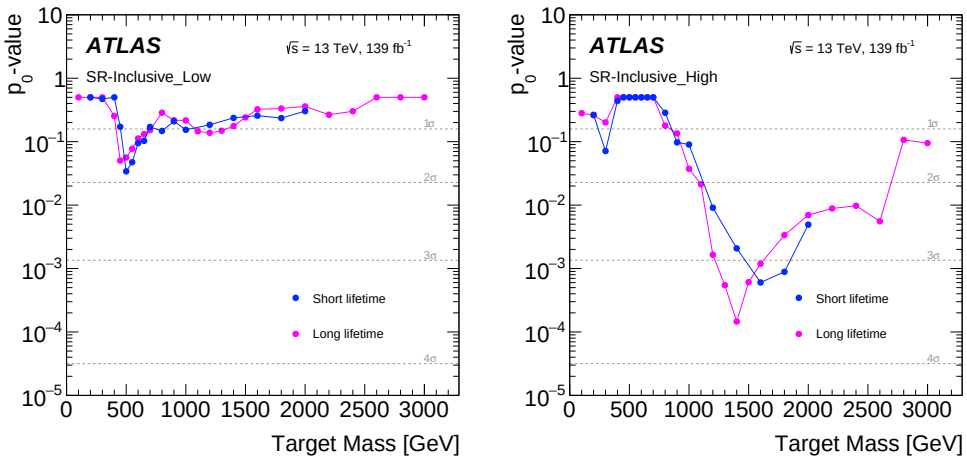

(a) p-values for `SR-Inclusive_Low` **(b)** p-values `SR-Inclusive_High`

Figure 10.5: The local p-values for (a) `SR-Inclusive_Low` and (b) `SR-Inclusive_High` [11].

$$\alpha(m) = (1 + \sigma(m))^s \,, \tag{10.11}$$

where m is the track mass, s is a parameter which is randomly sampled from a Gaussian distribution, and $\sigma(m)$ is the dominant systematic uncertainty on the background as a function of mass. After smearing the mass distribution, the signal region yield is then Poisson fluctuated to compute a yield for the given toy experiment. Then, the mass of each pseudo-track in the signal region is assigned by sampling the smeared background mass distribution. Finally, treating these pseudo-tracks as the observed tracks for the toy experiment, the significance of the deviation in each mass window is calculated, and the largest significance across all of the mass windows is treated as the local significance for the given experiment. This is repeated with 1 million toys to generated the distribution of local significances given the background-only hypothesis. Finally, the p-value of the true observed

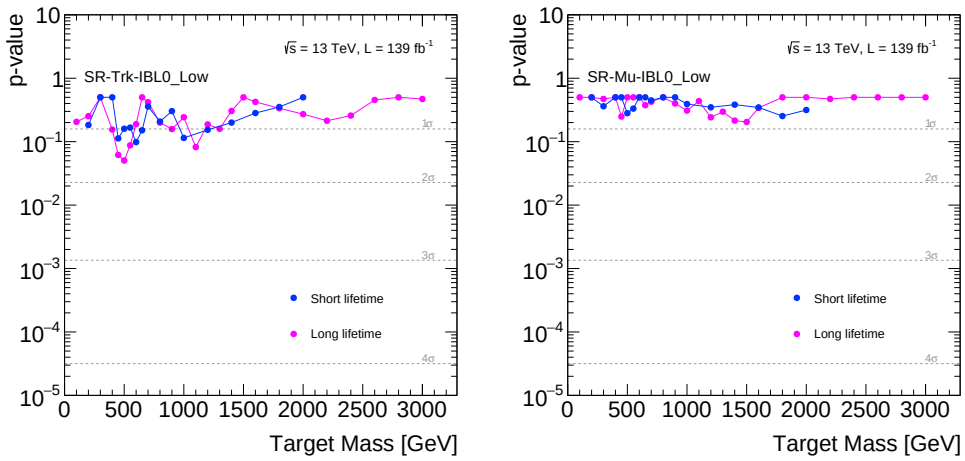

(a) p-values for `SR-Trk-IBL0_Low` **(b)** p-values for `SR-Mu-IBL0_Low`

Figure 10.6: The local p-values for (a) `SR-Trk-IBL0_Low` and (b) `SR-Mu-IBL0_Low`.[†]

local significance can be calculated from this distribution, resulting in a global significance of 3.3σ.

Limits are also set on the cross-sections of the processes discussed in Chapter 7 for long-lived gluinos, charginos, and sleptons. A multibin likelihood function is constructed incorporating the six exclusion regions. In addition to the uncertainties on the background prediction, the uncertainties on the signal prediction, described in Chapter 9, are also considered when setting limits.

The test statistic in Equation 10.3 is used and limits are calculated using the CL_s procedure [145]. All limits are calculated at 95% confidence level (CL). To calculate the upper limit on the signal-cross section that is excluded, for each signal point (mass, lifetime), background-only and signal-and-background hypotheses are generated with 10k toys for 20 fixed μ values, where μ represents the signal strength.

The background-only and signal-and-background hypotheses are generated using 10,000 toys for

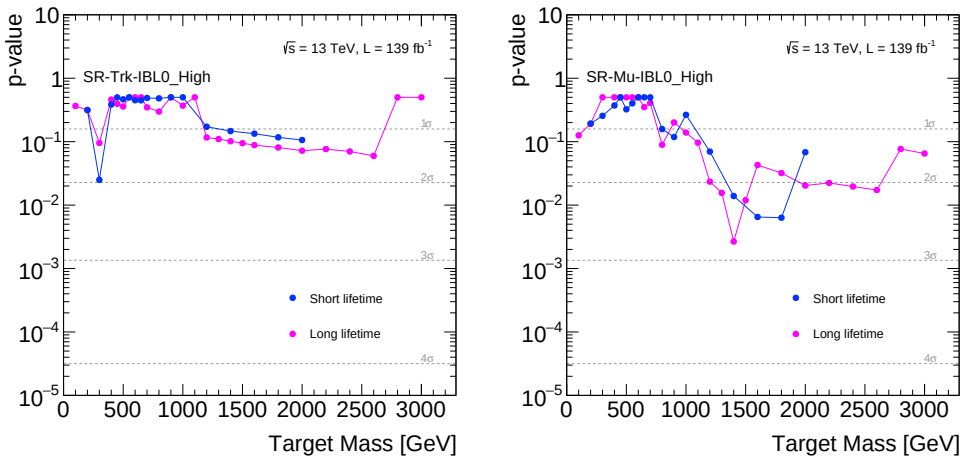

(a) p-values for `SR-Trk-IBL0_High` **(b)** p-values for `SR-Mu-IBL0_High`

Figure 10.7: The local p-values for (a) `SR-Trk-IBL0_High` and (b) `SR-Mu-IBL0_High`.[†]

each fixed μ point. The test statistic for the observed data (or expected data for expected limits) is then calculated from the toy distributions for the background-only and signal-and-background hypotheses. The p-values of these two hypotheses (p_μ and p_0) are then calculated and used to calculate the CL_s value, which is defined as [16]

$$CL_s = \frac{p_\mu}{1 - p_0}. \tag{10.12}$$

If the CL_s is less than 0.05, the point is said to be excluded at the 95% CL. The CL_s values at various μ values are then interpolated to calculate the largest excluded μ, which is then converted to the cross-section. The cross-section is then compared to the theoretical signal cross-section to calculated the excluded signal mass range.

Figures 10.9 and 10.10 show the expected and observed limits for the signal models considered.

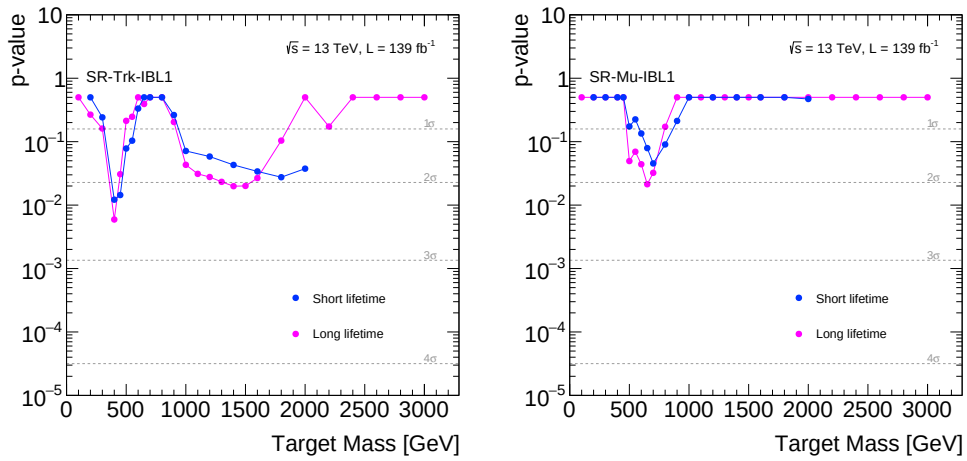

(a) p-values for `SR-Trk-IBL1` **(b)** p-values for `SR-Mu-IBL1`

Figure 10.8: The local p-values for (a) `SR-Trk-IBL1` and (b) `SR-Mu-IBL1`.[†]

For the gluino and chargino limits, the largest excluded mass for each lifetime is shown. For lifetime points without dedicated Monte Carlo signal samples, samples adjacent in lifetime were reweighted to have the desired lifetime. The analysis is most sensitive for lifetimes larger than $\approx$ 10 ns. For shorter lifetimes, the sensitivity is reduced due to the reduced track reconstruction efficiency.

For metastable signals, gluinos decaying to 100 GeV neutralinos are excluded up to masses of 2.27 TeV for τ = 20 ns. For the compressed gluino signals, gluino masses of 2.06 TeVare excluded for τ = 30 ns. Charginos are excluded up to 1.07 TeV for τ = 30 ns. Stable gluinos and charginos are excluded up to 2.06 and 1.07 TeV, respectively.

For the slepton signal, Figure 10.10b shows the largest and smallest slepton mass excluded for a range of lifetimes. The analysis sensitivity decreases at the smallest masses due to the reduced discrimination power of the $\mathrm{d}E/\mathrm{d}x$ variable. Staus with masses of 220 to 360 GeVand τ = 10 ns are

excluded.

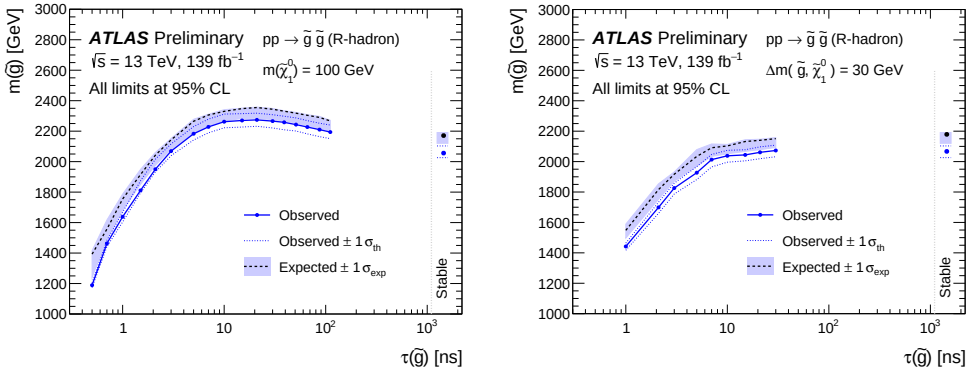

(a) m_χ = 100 GeV **(b)** Δm = 30 GeV

Figure 10.9: Limits at 95% CL for long-lived gluino signals with the neutralino mass fixed at (a) 100 GeV and (b) 30 GeV less than the gluino mass [11].

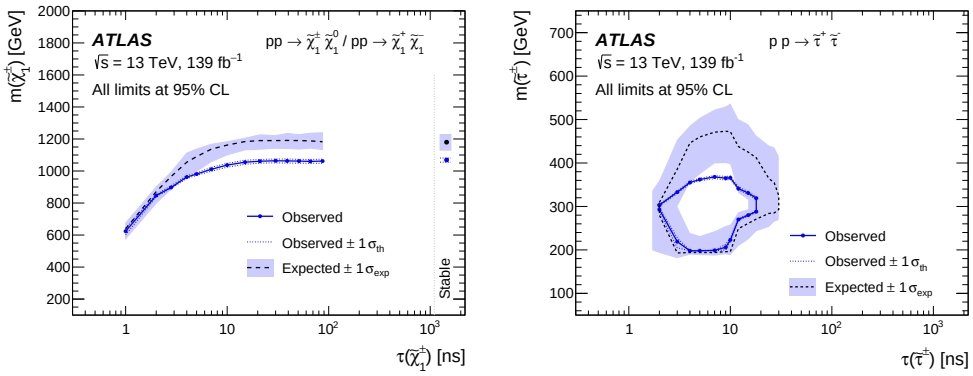

(a) chargino **(b)** slepton

Figure 10.10: Limits at 95% CL for long-lived (a) charginos and (b) sleptons [11].

11

Conclusion

A search for highly ionizing long-lived particles using the $\mathrm{d}E/\mathrm{d}x$ measurement in the ATLAS pixel detector was conducted with proton-proton collisions at the LHC. The full Run-2 dataset, with an integrated luminosity of 139 fb^{-1}, was used for this search. The analysis was designed to look for high momentum tracks with large $\mathrm{d}E/\mathrm{d}x$ deposits in the four pixel detector layers.

Eight signal regions were used to search for evidence of new physics. Using the $\mathrm{d}E/\mathrm{d}x$ measure-

ment and the momentum measurement for each track, the mass of tracks in the signal regions was reconstructed. A series of mass windows were applied to the mass distribution in each signal region. The observed and predicted yields in each window were reported.

The observed yields are compatible with Standard Model expectation across the signal regions at low mass. At high mass, the largest excess above Standard Model expectation was observed in the `SR-Inclusive_High` region targeting long lifetimes in a mass window from 1100 GeV to 2800 GeV. 7 events were observed and 0.7 ± 0.4 events were expected. A statistical test was conducted using a likelihood-based test statistic to quantify the disagreement with Standard Model expectation. The local (global) significance of this deviation is 3.6 (3.3)σ. Further investigation with future LHC data or complementary analyses is required to understand the origin of the deviation.

References

[1] M Gell-Mann. The eightfold way: A theory of strong interaction symmetry. doi: 10.2172/4008239. URL https://www.osti.gov/biblio/4008239.

[2] Y Ne'eman. Derivation of strong interactions from a gauge invariance. *Nuclear Phys.* doi: 10.1016/0029-5582(61)90134-1. URL https://www.osti.gov/biblio/4839172.

[3] V. E. Barnes et al. Observation of a hyperon with strangeness minus three. *Phys. Rev. Lett.*, 12:204–206, Feb 1964. doi: 10.1103/PhysRevLett.12.204. URL https://link.aps.org/doi/10.1103/PhysRevLett.12.204.

[4] Peter W. Higgs. Broken symmetries and the masses of gauge bosons. *Phys. Rev. Lett.*, 13: 508–509, Oct 1964. doi: 10.1103/PhysRevLett.13.508. URL https://link.aps.org/doi/10.1103/PhysRevLett.13.508.

[5] Peter W. Higgs. Broken symmetries, massless particles and gauge fields. *Phys. Lett.*, 12:132–133, 1964. doi: 10.1016/0031-9163(64)91136-9. URL https://cds.cern.ch/record/641590.

[6] F. Englert and R. Brout. Broken symmetry and the mass of gauge vector mesons. *Phys. Rev. Lett.*, 13:321–323, Aug 1964. doi: 10.1103/PhysRevLett.13.321. URL https://link.aps.org/doi/10.1103/PhysRevLett.13.321.

[7] G. S. Guralnik, C. R. Hagen, and T. W. B. Kibble. Global conservation laws and massless particles. *Phys. Rev. Lett.*, 13:585–587, Nov 1964. doi: 10.1103/PhysRevLett.13.585. URL https://link.aps.org/doi/10.1103/PhysRevLett.13.585.

[8] The CMS Collaboration. Observation of a new boson at a mass of 125 GeV with the CMS experiment at the LHC. *Physics Letters B*, 716(1):30–61, 2012. ISSN 0370-2693. doi: https://doi.org/10.1016/j.physletb.2012.08.021. URL https://www.sciencedirect.com/science/article/pii/S0370269312008581.

[9] The ATLAS Collaboration. Observation of a new particle in the search for the Standard Model Higgs boson with the ATLAS detector at the LHC. *Physics Letters B*, 716(1):1–29,

2012. ISSN 0370-2693. doi: https://doi.org/10.1016/j.physletb.2012.08.020. URL https://www.sciencedirect.com/science/article/pii/S037026931200857X.

[10] The ATLAS Collaboration. Search for heavy, long-lived, charged particles with large ionization energy loss in pp collisions at $\sqrt{s}$ = 13 TeV using the ATLAS experiment and the full Run 2 dataset. Technical Report ATL-COM-PHYS-2021-031, CERN, Geneva, May 2021. URL https://cds.cern.ch/record/2751231.

[11] The ATLAS Collaboration. Search for heavy, long-lived charged particles with large ionisation energy loss in pp collisions at $\sqrt{s} = 13$ TeV using the ATLAS experiment and the full Run 2 dataset. 2022.

[12] The Super-Kamiokande Collaboration. Evidence for oscillation of atmospheric neutrinos. *Phys. Rev. Lett.*, 81:1562–1567, Aug 1998. doi: 10.1103/PhysRevLett.81.1562. URL https://link.aps.org/doi/10.1103/PhysRevLett.81.1562.

[13] The SNO Collaboration. Measurement of the Rate of $\nu_e + d \rightarrow p + p + e^-$ Interactions Produced by ^8B Solar Neutrinos at the Sudbury Neutrino Observatory. *Phys. Rev. Lett.*, 87: 071301, Jul 2001. doi: 10.1103/PhysRevLett.87.071301. URL https://link.aps.org/doi/10.1103/PhysRevLett.87.071301.

[14] J. Barranco. Some Standard model problems and possible solutions. *Journal of Physics: Conference Series*, 761:012007, oct 2016. doi: 10.1088/1742-6596/761/1/012007. URL https://doi.org/10.1088/1742-6596/761/1/012007.

[15] Mary K. Gaillard, Paul D. Grannis, and Frank J. Sciulli. The standard model of particle physics. *Rev. Mod. Phys.*, 71:S96–S111, Mar 1999. doi: 10.1103/RevModPhys.71.S96. URL https://link.aps.org/doi/10.1103/RevModPhys.71.S96.

[16] P.A. Zyla et al. Review of Particle Physics. *PTEP*, 2020(8):083C01, 2020. doi: 10.1093/ptep/ptaa104.

[17] J. H. Oort. The force exerted by the stellar system in the direction perpendicular to the galactic plane and some related problems. *Bulletin of the Astronomical Institutes of the Netherlands*, 6:249, August 1932.

[18] F. Zwicky. Die Rotverschiebung von extragalaktischen Nebeln. *Helvetica Physica Acta*, 6: 110–127, January 1933.

[19] F. Zwicky. On the Masses of Nebulae and of Clusters of Nebulae. *Astrophysical Journal*, 86: 217, October 1937. doi: 10.1086/143864.

[20] Vera C. Rubin. The rotation of spiral galaxies. *Science*, 220(4604):1339–1344, 1983. ISSN 0036-8075. doi: 10.1126/science.220.4604.1339. URL https://science.sciencemag.org/content/220/4604/1339.

[21] D. Walsh, R. F. Carswell, and R. J. Weymann. 0957+561 A, B: twin quasistellar objects or gravitational lens? *Nature*, 279:381–384, May 1979. doi: 10.1038/279381a0.

[22] Katherine Garrett and Gintaras Duda. Dark matter: A primer. *Advances in Astronomy*, 2011:1–22, 2011. ISSN 1687-7977. doi: 10.1155/2011/968283. URL http://dx.doi.org/10.1155/2011/968283.

[23] Stephen P. Martin. A supersymmetry primer. *Advanced Series on Directions in High Energy Physics*, page 1–98, Jul 1998. ISSN 1793-1339. doi: 10.1142/9789812839657_0001. URL http://dx.doi.org/10.1142/9789812839657_0001.

[24] K. Abe, Y. Haga, Y. Hayato, M. Ikeda, K. Iyogi, J. Kameda, Y. Kishimoto, M. Miura, S. Moriyama, M. Nakahata, and et al. Search for proton decay via p→e+π0 and p→μ+π0 in 0.31 megaton·years exposure of the Super-Kamiokande water Cherenkov detector. *Physical Review D*, 95(1), Jan 2017. ISSN 2470-0029. doi: 10.1103/physrevd.95.012004. URL http://dx.doi.org/10.1103/PhysRevD.95.012004.

[25] Janusz Rosiek. Complete set of Feynman rules for the minimal supersymmetric extension of the standard model. *Physical Review D*, 41(11):3464–3501, Jun 1990. ISSN 0556-2821. doi: 10.1103/physrevd.41.3464. URL http://dx.doi.org/10.1103/PhysRevD.41.3464.

[26] Savas Dimopoulos and David Sutter. The supersymmetric flavor problem. *Nuclear Physics B*, 452(3):496–512, Oct 1995. ISSN 0550-3213. doi: 10.1016/0550-3213(95)00421-n. URL http://dx.doi.org/10.1016/0550-3213(95)00421-N.

[27] G.F. Giudice and R. Rattazzi. Theories with gauge-mediated supersymmetry breaking. *Physics Reports*, 322(6):419–499, Dec 1999. ISSN 0370-1573. doi: 10.1016/s0370-1573(99)00042-3. URL http://dx.doi.org/10.1016/S0370-1573(99)00042-3.

[28] Gian F Giudice, Riccardo Rattazzi, Markus A Luty, and Hitoshi Murayama. Gaugino mass without singlets. *Journal of High Energy Physics*, 1998(12):027–027, Dec 1998. ISSN

1029-8479. doi: 10.1088/1126-6708/1998/12/027. URL http://dx.doi.org/10.1088/1126-6708/1998/12/027.

[29] Lisa Randall and Raman Sundrum. Out of this world supersymmetry breaking. *Nuclear Physics B*, 557(1-2):79–118, Sep 1999. ISSN 0550-3213. doi: 10.1016/s0550-3213(99)00359-4. URL http://dx.doi.org/10.1016/S0550-3213(99)00359-4.

[30] Nima Arkani-Hamed and Savas Dimopoulos. Supersymmetric unification without low energy supersymmetry and signatures for fine-tuning at the lhc. *Journal of High Energy Physics*, 2005(06):073–073, Jun 2005. ISSN 1029-8479. doi: 10.1088/1126-6708/2005/06/073. URL http://dx.doi.org/10.1088/1126-6708/2005/06/073.

[31] G.F. Giudice and A. Romanino. Erratum to: "split supersymmetry" [nucl. phys. b 699 (2004) 65]. *Nuclear Physics B*, 706(1-2):487, Jan 2005. ISSN 0550-3213. doi: 10.1016/j.nuclphysb.2004.11.048. URL http://dx.doi.org/10.1016/j.nuclphysb.2004.11.048.

[32] SUSY March 2021 Summary Plot Update. Technical Report ATL-PHYS-PUB-2021-007, CERN, Geneva, Mar 2021. URL http://cds.cern.ch/record/2758782.

[33] Daniele Alves, Nima Arkani-Hamed, Sanjay Arora, Yang Bai, Matthew Baumgart, Joshua Berger, Matthew Buckley, Bart Butler, Spencer Chang, Hsin-Chia Cheng, and et al. Simplified models for LHC new physics searches. *Journal of Physics G: Nuclear and Particle Physics*, 39(10):105005, Sep 2012. ISSN 1361-6471. doi: 10.1088/0954-3899/39/10/105005. URL http://dx.doi.org/10.1088/0954-3899/39/10/105005.

[34] Lawrence Lee, Christian Ohm, Abner Soffer, and Tien-Tien Yu. Collider searches for long-lived particles beyond the Standard Model. *Progress in Particle and Nuclear Physics*, 106: 210–255, May 2019. ISSN 0146-6410. doi: 10.1016/j.ppnp.2019.02.006. URL http://dx.doi.org/10.1016/j.ppnp.2019.02.006.

[35] The ATLAS Collaboration. Search for heavy charged long-lived particles in proton–proton collisions at $\sqrt{s} = 13$ TeV using an ionisation measurement with the ATLAS detector. *Physics Letters B*, 788:96–116, Jan 2019. ISSN 0370-2693. doi: 10.1016/j.physletb.2018.10.055. URL http://dx.doi.org/10.1016/j.physletb.2018.10.055.

[36] The ATLAS Collaboration. Search for metastable heavy charged particles with large ionization energy loss in pp collisions at $\sqrt{s} = 13$ TeV using the ATLAS experiment. *Physi-*

cal Review D, 93(11), Jun 2016. ISSN 2470-0029. doi: 10.1103/physrevd.93.112015. URL http://dx.doi.org/10.1103/PhysRevD.93.112015.

[37] The ATLAS Collaboration. Search for metastable heavy charged particles with large ionisation energy loss in pp collisions at $\sqrt{s} = 8$ TeV using the ATLAS experiment. *The European Physical Journal C*, 75(9), Sep 2015. ISSN 1434-6052. doi: 10.1140/epjc/s10052-015-3609-0. URL http://dx.doi.org/10.1140/epjc/s10052-015-3609-0.

[38] The ATLAS Collaboration. Search for heavy charged long-lived particles in the ATLAS detector in 36.1fb^1 of proton-proton collision data at $\sqrt{s} = 13$ TeV. *Physical Review D*, 99(9), May 2019. ISSN 2470-0029. doi: 10.1103/physrevd.99.092007. URL http://dx.doi.org/10.1103/PhysRevD.99.092007.

[39] Search for heavy stable charged particles with 12.9 fb^{-1} of 2016 data. Technical report, CERN, Geneva, 2016. URL https://cds.cern.ch/record/2205281.

[40] The ATLAS Collaboration. Search for long-lived, massive particles in events with displaced vertices and missing transverse momentum in $\sqrt{s} = 13$ TeV pp collisions with the atlas detector. *Physical Review D*, 97(5), Mar 2018. ISSN 2470-0029. doi: 10.1103/physrevd.97.052012. URL http://dx.doi.org/10.1103/PhysRevD.97.052012.

[41] ATLAS Collaboration. Search for displaced leptons in $\sqrt{s} = 13$ TeV pp collisions with the ATLAS detector, 2020.

[42] Claude Leroy and Pier Giorgio Rancoita. *Principles of Radiation Interaction in Matter and Detection, 2nd Edition*. 02 2009. doi: 10.1142/6872.

[43] Niels Bohr. *The penetration of atomic particles through matter*. Munksgaard Copenhagen, 1948.

[44] Richard Clinton Fernow. *Introduction to Experimental Particle Physics*. Cambridge University Press, 1986. doi: 10.1017/CBO9780511622588.

[45] John David Jackson. *Classical electrodynamics*. Wiley, New York, NY, 3rd ed. edition, 1999. ISBN 9780471309321. URL http://cdsweb.cern.ch/record/490457.

[46] John Sabin. Determination of the mean excitation energy of materials for projectile stopping power. *Journal of Physical Chemistry & Biophysics*, 04, 01 2014. doi: 10.4172/2161-0398.1000e118.

[47] H. Bichsel. Shell corrections in stopping powers. *Phys. Rev. A*, 65:052709, Apr 2002. doi: 10.1103/PhysRevA.65.052709. URL https://link.aps.org/doi/10.1103/PhysRevA.65.052709.

[48] Hans Bethe. Zur theorie des durchgangs schneller korpuskularstrahlen durch materie. *Annalen der Physik*, 397(3):325–400, 1930.

[49] Enrico Fermi. The ionization loss of energy in gases and in condensed materials. *Phys. Rev.*, 57:485–493, Mar 1940. doi: 10.1103/PhysRev.57.485. URL https://link.aps.org/doi/10.1103/PhysRev.57.485.

[50] U Fano. Penetration of protons, alpha particles, and mesons. *Annual Review of Nuclear Science*, 13(1):1–66, 1963. doi: 10.1146/annurev.ns.13.120163.000245. URL https://doi.org/10.1146/annurev.ns.13.120163.000245.

[51] Felix Bloch. Bremsvermögen von atomen mit mehreren elektronen. *Zeitschrift für Physik*, 81 (5):363–376, 1933.

[52] Felix Bloch. Zur bremsung rasch bewegter teilchen beim durchgang durch materie. *Annalen der Physik*, 408(3):285–320, 1933.

[53] Walter H Barkas, John N Dyer, and Harry H Heckman. Resolution of the σ–mass anomaly. *Physical Review Letters*, 11(1):26, 1963.

[54] Lev Davidovich Landau and Dirk Ter-Haar. *Collected papers of L.D. Landau*. Pergamon, Oxford, 1965. URL https://cds.cern.ch/record/104093.

[55] Fluctuations of energy loss by heavy charged particles in matter. Technical Report UCRL-16931, Lawrence Berkeley National Laboratory, 1966. URL https://escholarship.org/uc/item/85n0b989.

[56] Hans Bichsel. The interaction of radiation with matter. *Landolt Börnstein*, pages 4–, 01 2011. doi: 10.1007/978-3-642-03606-4_2.

[57] M. Stanley Livingston and H. A. Bethe. Nuclear physics c. nuclear dynamics, experimental. *Rev. Mod. Phys.*, 9:245–390, Jul 1937. doi: 10.1103/RevModPhys.9.245. URL https://link.aps.org/doi/10.1103/RevModPhys.9.245.

[58] Rene Brun and Fons Rademakers. ROOT - An Object Oriented Data Analysis Framework. In *AIHENP'96 Workshop, Lausane*, volume 389, pages 81–86, 1996.

[59] Eugene Bulyak and Nikolay Shul'ga. Statistics of relativistic electrons radiating in periodic fields. *Phys. Rev. Accel. Beams*, 22:040705, Apr 2019. doi: 10.1103/PhysRevAccelBeams.22.040705. URL https://link.aps.org/doi/10.1103/PhysRevAccelBeams.22.040705.

[60] John P. Nolan. *Univariate Stable Distributions*. Springer Nature, 2020.

[61] P V Vavilov. Ionization losses of high-energy heavy particles. *Soviet Phys. JETP*. URL https://www.osti.gov/biblio/4311507.

[62] W W M Allison and J H Cobb. Relativistic charged particle identification by energy loss. *Annual Review of Nuclear and Particle Science*, 30(1):253–298, 1980. doi: 10.1146/annurev.ns.30.120180.001345. URL https://doi.org/10.1146/annurev.ns.30.120180.001345.

[63] Hans Bichsel. Straggling in thin silicon detectors. *Rev. Mod. Phys.*, 60:663–699, Jul 1988. doi: 10.1103/RevModPhys.60.663. URL https://link.aps.org/doi/10.1103/RevModPhys.60.663.

[64] LHC Guide. Mar 2017. URL https://cds.cern.ch/record/2255762.

[65] Oliver Sim Brüning, Paul Collier, P Lebrun, Stephen Myers, Ranko Ostojic, John Poole, and Paul Proudlock. *LHC Design Report*. CERN Yellow Reports: Monographs. CERN, Geneva, 2004. doi: 10.5170/CERN-2004-003-V-1. URL https://cds.cern.ch/record/782076.

[66] Joao Pequenao. Computer generated image of the whole ATLAS detector. Mar 2008. URL https://cds.cern.ch/record/1095924.

[67] ATLAS Collaboration. The ATLAS experiment at the CERN Large Hadron Collider. *Journal of Instrumentation*, 3(08):S08003–S08003, aug 2008. doi: 10.1088/1748-0221/3/08/s08003. URL https://doi.org/10.1088/1748-0221/3/08/s08003.

[68] Joao Pequenao. Computer generated image of the ATLAS inner detector. Mar 2008. URL https://cds.cern.ch/record/1095926.

[69] Track Reconstruction Performance of the ATLAS Inner Detector at $\sqrt{s} = 13$ TeV. Technical Report ATL-PHYS-PUB-2015-018, CERN, Geneva, Jul 2015. URL https://cds.cern.ch/record/2037683.

[70] G. Aad et al. ATLAS pixel detector electronics and sensors. *JINST*, 3:P07007, 2008. doi: 10.1088/1748-0221/3/07/P07007.

[71] dE/dx measurement in the ATLAS Pixel Detector and its use for particle identification. Technical Report ATLAS-CONF-2011-016, CERN, Geneva, Mar 2011. URL http://cds.cern.ch/record/1336519.

[72] B. Abbott et al. Production and Integration of the ATLAS Insertable B-Layer. *JINST*, 13(05): T05008, 2018. doi: 10.1088/1748-0221/13/05/T05008.

[73] The ATLAS collaboration. Operation and performance of the ATLAS semiconductor tracker. *Journal of Instrumentation*, 9(08):P08009–P08009, aug 2014. doi: 10.1088/1748-0221/9/08/p08009. URL https://doi.org/10.1088/1748-0221/9/08/p08009.

[74] Aijaz Ahmad, Z. Albrechtskirchinger, P.P. Allport, Javi Alonso, Ladislav Andricek, Robert Apsimon, A.J. Barr, Richard Bates, G.A. Beck, P.J. Bell, A. Belymam, J. Benes, C.M. Berg, J. Bernabeu, Siegfried Bethke, N. Bingefors, J.P. Bizzell, J. Bohm, R. Brenner, and A. Zsenei. The silicon microstrip sensors of the ATLAS semiconductor tracker. *Nuclear Instruments and Methods in Physics Research Section A: Accelerators, Spectrometers, Detectors and Associated Equipment*, 578:98–118, 07 2007. doi: 10.1016/j.nima.2007.04.157.

[75] The ATLAS Collaboration. Performance of the ATLAS Transition Radiation Tracker in Run 1 of the LHC: tracker properties. *Journal of Instrumentation*, 12(05):P05002–P05002, May 2017. ISSN 1748-0221. doi: 10.1088/1748-0221/12/05/p05002. URL http://dx.doi.org/10.1088/1748-0221/12/05/P05002.

[76] The ATLAS Collaboration. TRT performance results from 13 TeV collision data. https://atlas.web.cern.ch/Atlas/GROUPS/PHYSICS/PLOTS/TRT-2016-001/, . Accessed: 2021-03-25.

[77] Nikiforos Nikiforou. Performance of the ATLAS Liquid Argon Calorimeter after three years of LHC operation and plans for a future upgrade, 2013.

[78] Ana Maria Henriques Correia. The ATLAS Tile Calorimeter. Technical Report ATL-TILECAL-PROC-2015-002, CERN, Geneva, Mar 2015. URL https://cds.cern.ch/record/2004868.

[79] ATLAS Collaboration. Topological cell clustering in the ATLAS calorimeters and its performance in LHC Run 1. *The European Physical Journal C*, 77(7), Jul 2017. ISSN 1434-6052. doi: 10.1140/epjc/s10052-017-5004-5. URL http://dx.doi.org/10.1140/epjc/s10052-017-5004-5.

[80] ATLAS muon spectrometer: Technical design report. 6 1997.

[81] Y Arai et al. ATLAS muon drift tube electronics. *Journal of Instrumentation*, 3(09):P09001–P09001, sep 2008. doi: 10.1088/1748-0221/3/09/p09001. URL https://doi.org/10.1088/1748-0221/3/09/p09001.

[82] The ATLAS Collaboration. Muon performance public figures from simulation. https://twiki.cern.ch/twiki/bin/view/AtlasPublic/MuonPerformancePublicPlotsSimulation, . Accessed: 2021-03-29.

[83] D Boscherini. Performance and operation of the ATLAS Resistive Plate Chamber system in LHC Run-1. Technical Report ATL-MUON-PROC-2014-005. 12, CERN, Geneva, Sep 2014. URL https://cds.cern.ch/record/1753173.

[84] The ATLAS Collaboration. Performance of the ATLAS trigger system in 2015. *The European Physical Journal C*, 77(5), May 2017. ISSN 1434-6052. doi: 10.1140/epjc/s10052-017-4852-3. URL http://dx.doi.org/10.1140/epjc/s10052-017-4852-3.

[85] The ATLAS collaboration. Operation of the ATLAS trigger system in Run 2. *Journal of Instrumentation*, 15(10):P10004–P10004, Oct 2020. ISSN 1748-0221. doi: 10.1088/1748-0221/15/10/p10004. URL http://dx.doi.org/10.1088/1748-0221/15/10/P10004.

[86] The ATLAS Collaboration. Performance of the missing transverse momentum triggers for the atlas detector during run-2 data taking. *Journal of High Energy Physics*, 2020(8), Aug 2020. ISSN 1029-8479. doi: 10.1007/jhep08(2020)080. URL http://dx.doi.org/10.1007/JHEP08(2020)080.

[87] Azriel Rosenfeld and John L. Pfaltz. Sequential operations in digital picture processing. *J. ACM*, 13(4):471–494, October 1966. ISSN 0004-5411. doi: 10.1145/321356.321357. URL https://doi.org/10.1145/321356.321357.

[88] T Cornelissen, M Elsing, I Gavrilenko, W Liebig, E Moyse, and A Salzburger. The new ATLAS track reconstruction (NEWT). *Journal of Physics: Conference Series*, 119:032014, 07 2008. doi: 10.1088/1742-6596/119/3/032014.

[89] The ATLAS Collaboration. Performance of the ATLAS track reconstruction algorithms in dense environments in LHC Run 2. *The European Physical Journal C*, 77(10), Oct 2017. ISSN 1434-6052. doi: 10.1140/epjc/s10052-017-5225-7. URL http://dx.doi.org/10.1140/epjc/s10052-017-5225-7.

[90] R. Frühwirth. Application of kalman filtering to track and vertex fitting. *Nuclear Instruments and Methods in Physics Research Section A: Accelerators, Spectrometers, Detectors and Associated Equipment*, 262(2):444–450, 1987. ISSN 0168-9002. doi: https://doi.org/10.1016/0168-9002(87)90887-4. URL https://www.sciencedirect.com/science/article/pii/0168900287908874.

[91] Richard O. Duda and Peter E. Hart. Use of the hough transformation to detect lines and curves in pictures. *Commun. ACM*, 15(1):11–15, January 1972. ISSN 0001-0782. doi: 10.1145/361237.361242. URL https://doi.org/10.1145/361237.361242.

[92] T Cornelissen, M Elsing, S Fleischmann, W Liebig, E Moyse, and A Salzburger. Concepts, Design and Implementation of the ATLAS New Tracking (NEWT). Technical Report ATL-SOFT-PUB-2007-007. ATL-COM-SOFT-2007-002, CERN, Geneva, Mar 2007. URL https://cds.cern.ch/record/1020106.

[93] The ATLAS Collaboration. Public pixel tracker plots for collision data. https://twiki.cern.ch/twiki/bin/view/AtlasPublic/PixelPublicResults, . Accessed: 2021-05-07.

[94] The ATLAS collaboration. A neural network clustering algorithm for the ATLAS silicon pixel detector. *Journal of Instrumentation*, 9(09):P09009–P09009, Sep 2014. ISSN 1748-0221. doi: 10.1088/1748-0221/9/09/p09009. URL http://dx.doi.org/10.1088/1748-0221/9/09/P09009.

[95] Training and validation of the ATLAS pixel clustering neural networks. Technical Report ATL-PHYS-PUB-2018-002, CERN, Geneva, Mar 2018. URL http://cds.cern.ch/record/2309474.

[96] Early Inner Detector Tracking Performance in the 2015 data at $\sqrt{s} = 13$ TeV. Technical Report ATL-PHYS-PUB-2015-051, CERN, Geneva, Dec 2015. URL http://cds.cern.ch/record/2110140.

[97] R Frühwirth, Wolfgang Waltenberger, and Pascal Vanlaer. Adaptive Vertex Fitting. Technical Report CMS-NOTE-2007-008, CERN, Geneva, Mar 2007. URL https://cds.cern.ch/record/1027031.

[98] The ATLAS Collaboration. Reconstruction of primary vertices at the atlas experiment in run 1 proton–proton collisions at the lhc. *The European Physical Journal C*, 77(5), May 2017. ISSN 1434-6052. doi: 10.1140/epjc/s10052-017-4887-5. URL http://dx.doi.org/10.1140/epjc/s10052-017-4887-5.

[99] The ATLAS Collaboration. Muon reconstruction performance of the ATLAS detector in proton–proton collision data at $\sqrt{s}$ =13 TeV. *Eur. Phys. J. C*, 76(5):292, 2016. doi: 10.1140/epjc/s10052-016-4120-y.

[100] Matteo Cacciari, Gavin P Salam, and Gregory Soyez. The anti-k_t jet clustering algorithm. *Journal of High Energy Physics*, 2008(04):063–063, Apr 2008. ISSN 1029-8479. doi: 10.1088/1126-6708/2008/04/063. URL http://dx.doi.org/10.1088/1126-6708/2008/04/063.

[101] The ATLAS Collaboration. Jet energy resolution in 2017 data and simulation. https://atlas.web.cern.ch/Atlas/GROUPS/PHYSICS/PLOTS/JETM-2018-005/, . Accessed: 2021-03-31.

[102] Tagging and suppression of pileup jets with the ATLAS detector. Technical Report ATLAS-CONF-2014-018, CERN, Geneva, May 2014. URL https://cds.cern.ch/record/1700870.

[103] The ATLAS Collaboration. Electron reconstruction and identification in the ATLAS experiment using the 2015 and 2016 LHC proton-proton collision data at $\sqrt{s} = 13$ TeV. *Eur. Phys. J. C*, 79(arXiv:1902.04655. 8):639. 40 p, Feb 2019. doi: 10.1140/epjc/s10052-019-7140-6. URL https://cds.cern.ch/record/2657964. 63 pages in total, author list starting page 47, 16 figures, 4 tables, final version published in EPJC. All figures including auxiliary figures are available at https://atlas.web.cern.ch/Atlas/GROUPS/PHYSICS/PAPERS/PERF-2017-01.

[104] The ATLAS Collaboration. Reconstruction of hadronic decay products of tau leptons with the atlas experiment. *The European Physical Journal C*, 76(5), May 2016. ISSN 1434-6052. doi: 10.1140/epjc/s10052-016-4110-0. URL http://dx.doi.org/10.1140/epjc/s10052-016-4110-0.

[105] G. Aad, B. Abbott, D.C. Abbott, A. Abed Abud, K. Abeling, D.K. Abhayasinghe, S.H. Abidi, O.S. AbouZeid, N.L. Abraham, H. Abramowicz, and et al. Electron and photon performance measurements with the ATLAS detector using the 2015–2017 LHC proton-proton collision data. *Journal of Instrumentation*, 14(12):P12006–P12006, Dec 2019. ISSN 1748-0221. doi: 10.1088/1748-0221/14/12/p12006. URL http://dx.doi.org/10.1088/1748-0221/14/12/P12006.

[106] Expected performance of missing transverse momentum reconstruction for the ATLAS detector at $\sqrt{s} = 13$ TeV. Technical report, CERN, Geneva, Jul 2015. URL https://cds.cern.ch/record/2037700. All figures including auxiliary figures are available at https://atlas.web.cern.ch/Atlas/GROUPS/PHYSICS/PUBNOTES/ATL-PHYS-PUB-2015-023.

[107] The ATLAS Collaboration. Performance of missing transverse momentum reconstruction with the ATLAS detector using proton–proton collisions at $\sqrt{s} = 13$ TeV. *The European Physical Journal C*, 78(11), Nov 2018. ISSN 1434-6052. doi: 10.1140/epjc/s10052-018-6288-9. URL http://dx.doi.org/10.1140/epjc/s10052-018-6288-9.

[108] M. Backhaus. The upgraded Pixel Detector of the ATLAS Experiment for Run 2 at the Large Hadron Collider. *Nuclear Instruments and Methods in Physics Research Section A: Accelerators, Spectrometers, Detectors and Associated Equipment*, 831:65–70, 2016. ISSN 0168-9002. doi: https://doi.org/10.1016/j.nima.2016.05.018. URL https://www.sciencedirect.com/science/article/pii/S0168900216303837. Proceedings of the 10th International "Hiroshima" Symposium on the Development and Application of Semiconductor Tracking Detectors.

[109] Luigi Rolandi, Werner Riegler, and Walter Blum. *Particle Detection with Drift Chambers*, volume -1. 01 2008. ISBN 978-3-540-76683-4. doi: 10.1007/978-3-540-76684-1.

[110] John Erthal Gaiser. *Charmonium spectroscopy from radiative decays of the J/ψ and ψ'**. PhD thesis, Stanford Linear Accelerator Center, Stanford University, National Technical Information Service, 8 1982.

[111] A Ruiz Martínez and. The run-2 ATLAS trigger system. *Journal of Physics: Conference Series*, 762:012003, oct 2016. doi: 10.1088/1742-6596/762/1/012003. URL https://doi.org/10.1088/1742-6596/762/1/012003.

[112] The ATLAS Collaboration. Feynman diagrams. https://feynman.web.cern.ch/feynman/, . Accessed: 2021-01-27.

[113] J. Alwall, R. Frederix, S. Frixione, V. Hirschi, F. Maltoni, O. Mattelaer, H.-S. Shao, T. Stelzer, P. Torrielli, and M. Zaro. The automated computation of tree-level and next-to-leading order differential cross sections, and their matching to parton shower simulations. *Journal of High Energy Physics*, 2014(7), Jul 2014. ISSN 1029-8479. doi: 10.1007/jhep07(2014)079. URL http://dx.doi.org/10.1007/JHEP07(2014)079.

[114] Torbjörn Sjöstrand, Stefan Ask, Jesper R. Christiansen, Richard Corke, Nishita Desai, Philip Ilten, Stephen Mrenna, Stefan Prestel, Christine O. Rasmussen, and Peter Z. Skands. An introduction to PYTHIA 8.2. *Computer Physics Communications*, 191:159–177, Jun 2015. ISSN 0010-4655. doi: 10.1016/j.cpc.2015.01.024. URL http://dx.doi.org/10.1016/j.cpc.2015.01.024.

[115] ATLAS Pythia 8 tunes to 7 TeV data. Technical Report ATL-PHYS-PUB-2014-021, CERN, Geneva, Nov 2014. URL https://cds.cern.ch/record/1966419.

[116] D. J. Lange. The EvtGen particle decay simulation package. *Nucl. Instrum. Meth. A*, 462: 152, 2001. doi: 10.1016/S0168-9002(01)00089-4.

[117] S. Agostinelli et al. Geant4—a simulation toolkit. *Nuclear Instruments and Methods in Physics Research Section A: Accelerators, Spectrometers, Detectors and Associated Equipment*, 506(3):250–303, 2003. ISSN 0168-9002. doi: https://doi.org/10.1016/S0168-9002(03)01368-8. URL https://www.sciencedirect.com/science/article/pii/S0168900203013688.

[118] A. C. Kraan. Interactions of heavy stable hadronising particles. *The European Physical Journal C*, 37(1):91–104, Sep 2004. ISSN 1434-6052. doi: 10.1140/epjc/s2004-01946-6. URL http://dx.doi.org/10.1140/epjc/s2004-01946-6.

[119] Generation and Simulation of R-Hadrons in the ATLAS Experiment. Technical Report ATL-PHYS-PUB-2019-019, CERN, Geneva, May 2019. URL https://cds.cern.ch/record/2676309.

[120] Giuseppe Bozzi, Benjamin Fuks, and Michael Klasen. Threshold Resummation for Slepton-Pair Production at Hadron Colliders. *Nucl. Phys. B*, 777:157, 2007. doi: 10.1016/j.nuclphysb.2007.03.052.

[121] Benjamin Fuks, Michael Klasen, David R. Lamprea, and Marcel Rothering. Precision predictions for electroweak superpartner production at hadron colliders with RESUMMINO. *Eur. Phys. J. C*, 73:2480, 2013. doi: 10.1140/epjc/s10052-013-2480-0.

[122] Benjamin Fuks, Michael Klasen, David R. Lamprea, and Marcel Rothering. Revisiting slepton pair production at the Large Hadron Collider. *JHEP*, 01:168, 2014. doi: 10.1007/JHEP01(2014)168.

[123] Juri Fiaschi and Michael Klasen. Slepton pair production at the LHC in NLO+NLL with resummation-improved parton densities. *JHEP*, 03:094, 2018. doi: 10.1007/JHEP03(2018)094.

[124] W. Beenakker et al. Production of Charginos, Neutralinos, and Sleptons at Hadron Colliders. *Phys. Rev. Lett.*, 83:3780, 1999. doi: 10.1103/PhysRevLett.83.3780.

[125] W. Beenakker et al. *Phys. Rev. Lett.*, 100:029901, 2008. doi: 10.1103/PhysRevLett.100.029901.

[126] Search for long-lived charginos based on a disappearing-track signature using 136 fb^{-1} of pp collisions at $\sqrt{s} = 13$ TeV with the ATLAS detector. Technical Report ATLAS-CONF-2021-015, CERN, Geneva, Mar 2021. URL http://cds.cern.ch/record/2759676.

[127] W. Beenakker, R. Höpker, M. Spira, and P.M. Zerwas. Squark and gluino production at hadron colliders. *Nucl. Phys. B*, 492:51, 1997. doi: 10.1016/S0550-3213(97)00084-9.

[128] A. Kulesza and L. Motyka. Threshold Resummation for Squark-Antisquark and Gluino-Pair Production at the LHC. *Phys. Rev. Lett.*, 102:111802, 2009. doi: 10.1103/PhysRevLett.102.111802.

[129] A. Kulesza and L. Motyka. Soft gluon resummation for the production of gluino-gluino and squark-antisquark pairs at the LHC. *Phys. Rev. D*, 80:095004, 2009. doi: 10.1103/PhysRevD.80.095004.

[130] Wim Beenakker, Silja Brensing, Michael Krämer, Anna Kulesza, Eric Laenen, and Irene Niessen. Soft-gluon resummation for squark and gluino hadroproduction. *JHEP*, 12:041, 2009. doi: 10.1088/1126-6708/2009/12/041.

[131] Wim Beenakker, Silja Brensing, Michael Krämer, Anna Kulesza, Eric Laenen, and Irene Niessen. NNLL resummation for squark-antisquark pair production at the LHC. *JHEP*, 01:076, 2012. doi: 10.1007/JHEP01(2012)076.

[132] Wim Beenakker, Tim Janssen, Susanne Lepoeter, Michael Krämer, Anna Kulesza, Eric Laenen, Irene Niessen, Silja Thewes, and Tom Van Daal. Towards NNLL resummation: hard matching coefficients for squark and gluino hadroproduction. *JHEP*, 10:120, 2013. doi: 10.1007/JHEP10(2013)120.

[133] Wim Beenakker, Christoph Borschensky, Michael Krämer, Anna Kulesza, Eric Laenen, Vincent Theeuwes, and Silja Thewes. NNLL Resummation for Squark-Antisquark and Gluino-Pair Production at the LHC. *JHEP*, 12:023, 2014. doi: 10.1007/JHEP12(2014)023.

[134] Wim Beenakker, Christoph Borschensky, Michael Krämer, Anna Kulesza, and Eric Laenen. NNLL-fast: predictions for coloured supersymmetric particle production at the LHC with threshold and Coulomb resummation. *JHEP*, 12:133, 2016. doi: 10.1007/JHEP12(2016)133.

[135] Christoph Borschensky, Michael Krämer, Anna Kulesza, Michelangelo Mangano, Sanjay Padhi, Tilman Plehn, and Xavier Portell. Squark and gluino production cross sections in pp collisions at $\sqrt{s} = 13, 14, 33$ and 100 tev. *The European Physical Journal C*, 74(12), Dec 2014. ISSN 1434-6052. doi: 10.1140/epjc/s10052-014-3174-y. URL http://dx.doi.org/10.1140/epjc/s10052-014-3174-y.

[136] S Tarem, S Bressler, H Nomoto, and A Dimattia. Trigger and Reconstruction for a heavy long lived charged particles with the ATLAS detector. Dec 2007. doi: 10.1140/epjc/s10052-009-1040-0. URL https://cds.cern.ch/record/1072765. Accepted as Scientific Note SN-ATLAS-2008-071.

[137] James Catmore, Jack Cranshaw, Thomas Gillam, Eirik Gramstad, Paul Laycock, Nurcan Ozturk, and Graeme Andrew Stewart. A new petabyte-scale data derivation framework for ATLAS. *Journal of Physics: Conference Series*, 664(7):072007, dec 2015. doi: 10.1088/1742-6596/664/7/072007. URL https://doi.org/10.1088/1742-6596/664/7/072007.

[138] James Catmore. The ATLAS data processing chain: from collisions to papers. https://indico.cern.ch/event/472469/contributions/1982677/attachments/1220934/1785823/intro_slides.pdf. Accessed: 2021-05-09.

[139] Luminosity determination in pp collisions at $\sqrt{s} = 13$ TeV using the ATLAS detector at the LHC. Technical report, CERN, Geneva, Jun 2019. URL https://cds.cern.ch/record/2677054. All figures including auxiliary figures are available at

https://atlas.web.cern.ch/Atlas/GROUPS/PHYSICS/CONFNOTES/ATLAS-CONF-2019-021.

[140] Glen Cowan, Kyle Cranmer, Eilam Gross, and Ofer Vitells. Asymptotic formulae for likelihood-based tests of new physics. *The European Physical Journal C*, 71(2), Feb 2011. ISSN 1434-6052. doi: 10.1140/epjc/s10052-011-1554-0. URL http://dx.doi.org/10.1140/epjc/s10052-011-1554-0.

[141] Heinrich, Lukas and Feickert, Matthew and Stark, Giordon. pyhf: v0.5.4. URL https://github.com/scikit-hep/pyhf.

[142] Lukas Heinrich, Matthew Feickert, Giordon Stark, and Kyle Cranmer. pyhf: pure-Python implementation of HistFactory statistical models. *Journal of Open Source Software*, 6(58): 2823, 2021. doi: 10.21105/joss.02823. URL https://doi.org/10.21105/joss.02823.

[143] Kyle Cranmer, George Lewis, Lorenzo Moneta, Akira Shibata, and Wouter Verkerke. HistFactory: A tool for creating statistical models for use with RooFit and RooStats. 6 2012.

[144] Reproducing searches for new physics with the ATLAS experiment through publication of full statistical likelihoods. Technical Report ATL-PHYS-PUB-2019-029, CERN, Geneva, Aug 2019. URL https://cds.cern.ch/record/2684863.

[145] A L Read. Presentation of search results: theCLstechnique. *Journal of Physics G: Nuclear and Particle Physics*, 28(10):2693–2704, sep 2002. doi: 10.1088/0954-3899/28/10/313. URL https://doi.org/10.1088/0954-3899/28/10/313.

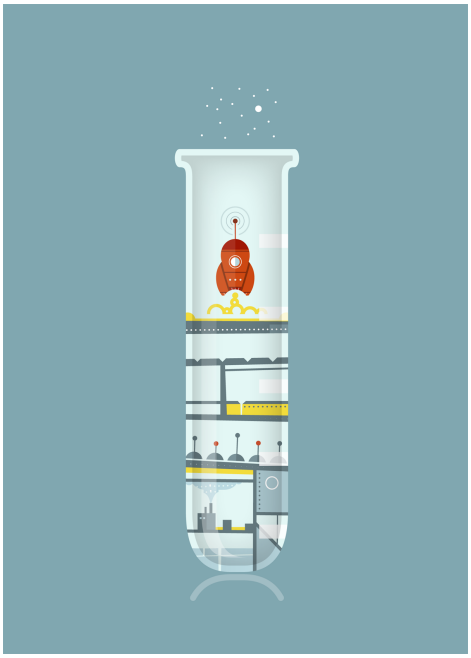

This thesis was typeset using LaTeX, originally developed by Leslie Lamport and based on Donald Knuth's TeX. The body text is set in 11 point Egenolff-Berner Garamond, a revival of Claude Garamont's humanist typeface. The above illustration, *Science Experiment 02*, was created by Ben Schlitter and released under CC BY-NC-ND 3.0. A template that can be used to format a PhD dissertation with this look & feel has been released under the permissive AGPL license, and can be found online at github.com/suchow/Dissertate or from its lead author, Jordan Suchow, at suchow@post.harvard.edu.